MICROWAVE ASSISTED SOLID STATE SYNTHESIS OF RARE EARTH IONS DOPED $LaBO_3$, YBO_3 AND $GdBO_3$, THEIR CHARACTERIZATIONS AND INVESTIGATIONS OF LUMINISCENCE PROPERTIES

A THESIS SUBMITTED TO THE GRADUATE SCHOOL OF NATURAL AND APPLIED
OF
MIDDLE EAST TECHNICAL UNIVERSITY

BY

METEHAN SEVEROĞLU

IN PARTIAL FULFILLMENT OF THE REQUIREMENTS
FOR
THE DEGREE OF MASTER OF SCIENCE
IN
CHEMISTRY

JUNE, 2016

Approval of the thesis:

MICROWAVE ASSISTED SOLID STATE SYNTHESIS OF RARE EARTH IONS DOPED $LaBO_3$, YBO_3 AND $GdBO_3$, THEIR CHARACTERIZATIONS AND INVESTIGATIONS OF LUMINISCENCE PROPERTIES

submitted by **METEHAN SEVEROĞLU** in partial fulfillment of the requirements for the degree of **Master of Science in Chemistry Department, Middle East Technical University** by,

Prof. Dr. Gülbin Dural Ünver _____
Dean, Graduate School of **Natural and Applied Sciences**

Prof. Dr. Cihangir Tanyeli _____
Head of Department, **Chemistry Department**

Prof. Dr. Ayşen Yılmaz _____
Supervisor, **Chemistry Department, METU**

Assoc. Prof. Dr. Okan Esentürk _____
Co-Supervisor, **Chemistry Department, METU**

Examining Committee Members

Prof. Dr. Nurşen Altuntaş Öztaş _____
Chemistry Department, Hacettepe Uni.

Prof. Dr. Ayşen Yılmaz _____
Chemistry Department, METU

Assoc. Prof. Dr. Okan Esentürk _____
Chemistry Department, METU

Assoc. Prof. Dr. Ali Çırpan _____
Chemistry Department, METU

Assoc. Prof. Dr. Mehmet Fatih Danışman _____
Chemistry Department, METU

Date: **09.06.2016**

I hereby declare that all information in this document has been obtained and presented in accordance with academic rules and ethical conduct. I also declare that, as required by these rules and conduct, I have fully cited and referenced all material and results that are not original to this work.

Name & Last Name: Metehan Severoğlu

Signature:

ABSTRACT

MICROWAVE ASSISTED SOLID STATE SYNTHESIS OF RARE EARTH IONS DOPED *$LaBO_3$*, *YBO_3* AND *$GdBO_3$*, THEIR CHARACTERIZATIONS AND INVESTIGATIONS OF LUMINISCENCE PROPERTIES

Severoğlu, Metehan

M. Sc. Department of Chemistry

Supervisor: Prof. Dr. Ayşen Yılmaz

Co-Supervisor: Assoc. Prof. Dr. Okan Esentürk

June 2016, 91 pages

$LnBO_3$ are notable host materials to doped with Rare Earth Element (REE) to achieve strong luminescence. Therefore, it attracts great attention of scientist for many decades with promising applications in many field such as affordable Light Emitting diode (LED) devices.

This research covers the synthesis of undoped lanthanum, gadolinium, and yttrium orthoborates and dysprosium, terbium and samarium ions doped $LnBO_3$ (Ln: La, Gd, Y) by microwave assisted solid state synthesis method to investigate the effect of changing concentration and identity of ions on their photoluminescence properties. Microwave assisted solid state synthesis method has various advantages such as reducing energy consumption with decreasing heating duration and producing fine powders. The samples were synthesized by heating mixtures of precursor solid reactants in microwave oven at 1200 W for ten minutes and heating them at 950° C for 2 hours in muffle furnace.

For characterization of powder samples X-ray diffraction were used. The morphological properties of undoped and rare earth ions doped the samples were examined by Scanning Electron Microscope (SEM). Moreover, Attenuated Total Reflection (ATR) spectrometry were done to identify vibrational modes of anionic groups. Far-IR spectrometry were employed for detecting low frequency modes. Fluorescence spectroscopy were employed for finding the luminescence characteristics of products.

The XRD patterns demonstrate that undoped and doped $LnBO_3$ powder samples were synthesized successfully with microwave assisted solid state method. From the XRD patterns, it is observed that added doping materials do not disturb the hosts' structure. SEM images of undoped and doped $LnBO_3$ powders show a fine particle with regular morphology. As results, doping with Dy^{3+}, Sm^{3+}, Tb^{3+} ions did not affect the crystallinity and morphology of $LnBO_3$. ATR results demonstrated that the presence of planar BO_3^{3-} units in $LaBO_3$ whereas tetrahedral $B_3O_9^{9-}$ ring containing planar BO_3^{3-} and tetrahedral BO_4^{5-} units in $GdBO_3$ and YBO_3. Far-IR results illustrate low frequency vibrational modes of $LnBO_3$. The differences in the observed vibrational modes of doped and undoped $LnBO_3$ help on identification of doping characteristics as interstitial or substitutional. Luminescence studies showed that 5.30% Dy doped $LaBO_3$ samples gives rise to the most intensive emission among all the samples prepared. International Commission on Illumination (CIE) studies show that Dy doped $LnBO_3$ samples give pale yellow, Sm doped $LnBO_3$ samples give orange color and Tb doped $LnBO_3$ samples give green color.

Keywords: Lanthanum orthoborate, Gadolinium orthoborate, Yttrium orthoborate, dysprosium, terbium, samarium, luminescence, color, urea, microwave assisted solid state synthesis.

ÖZ

NADİR TOPRAK İYONLARI İLE KATKILI $LaBO_3$,YBO_3 VE $GdBO_3$ ORTOBORATLARIN MİKRODALGA YARDIMLI KATI HAL SENTEZİ KARAKTERİZASYONU VE LÜMİNESANS ÖZELLİKLERİNİN ARAŞTIRILMASI

Severoğlu, Metehan
Yüksek Lisans, Kimya Bölümü
Tez Yöneticisi: Prof. Dr. Ayşen Yılmaz
Ortak Tez Yöneticisi: Doç. Dr. Okan Esentürk

Haziran 2016, 91 Sayfa

$LnBO_3$ dikkate değer anayapılar olup Nadir Toprak elementleri (NTE) ile katkılandığında yüksek şiddette lüminesans özelliği göstermektedir. Bu yüzden, birçok alanda kullanılabilecek olan bu malzemeler, örneğin ekonomik Işık Yayan Diyot (LED) cihazları, bilim adamlarının ilgisini uzun yıllardır çekmektedir.

Bu çalışmada, katkısız lantan, gadolinyum, ve itriyum ortoboratların ve nadir toprak elementleri disprosyum, terbiyum ve samaryum iyonları ile katkılanmış bu ortoboratların, mikrodalga yardımlı katı hal sentezi ile değişen konsantrasyon etkisi ve farklı iyonların, fotolüminesans üzerindeki etkileri araştırılmıştır. Mikrodalga yardımlı katı hal sentez yöntemi çeşitli avantajlara sahiptir. Bu sentez yönteminde ısıtma süresinin kısaltılması ile enerji tüketimi azaltılmıştır ve düzgün parçacık şekilli toz numuneler hazırlanmıştır. Numuneler, başlangıç karışımı mikrodalga fırınında 1200 W'ta 10 dakika bekletildikten sonra 2 saat boyuna 950° C deki fırında ısıtılarak sentezlenmiştir.

X ışınları toz kırınımı (XRD) metodu malzemenin kristal yapı karakterizasyonu için kullanılmıştır. Katkılı ve katkısız numunelerin morfolojik çalışması Taramalı Elektron Mikroskobu (SEM) kullanılarak tamamlanmıştır. Ayrıca, anyonik grupların bağ

yapısını ve bantlarını tanımlayabilmek adına ATR spektrometresi analizleri gerçekleştirilmiştir. Far-IR spektrometresi, düşük frekanslardaki bağların bantlarını belirlemek için kullanılmıştır. Floresans spektrometresi numunelerin lüminesans özelliklerini bulmak için kullanılmıştır.

XRD desenleri katkısız ve katkılı $LnBO_3$ toz numunelerin, başarıyla sentezlendiğini göstermektedir. Bu desenlerden; eklenen katkı iyonlarının anayapıda herhangi bir değişime sebep olmadığı gözlemlenmiştir. Katkılı ve katkısız toz numunelerin SEM görüntüleri; örneklerin düzgün şekilli toz parçacıklar ile düzenli morfolojisi olduğunu göstermiştir. Sonuç olarak, katkılanan Dy^{3+}, Sm^{3+}, Tb^{3+} iyonlarının anayapının kristal yapısına ve morfolojisine ektisi olmadığı görülmüştür. ATR sonuçları göstermiştir ki $LaBO_3$ anayapısı düzlemsel BO_3^{3-} birimlerinden oluşurken, $GdBO_3$ ve YBO_3 anayapıları düzlemsel BO_3^{3-} ve dörtyüzlü BO_4^{5-}'ten oluşan $B_3O_9^{9-}$ birimlerine sahiptir. Far-IR sonuçları, düşük frekanstaki salınım hareketlerinin bantlarını göstermiştir. Bu sayede, katkılı ve katkısız örneklerin gözlemlenen salınım bantları, katkılanan iyonun yapıda nereye yerleştiğini (arayagirme veya yerdeğiştirme) tanımlamak için yardımcı olmuştur. Lüminesans çalışmaları göstermiştir ki en yüksek lüminesans şiddetini hazırlanan tüm örnekler içerisinden, %5.30 Dy katkılı $LaBO_3$ numunesi vermiştir. CIE çalışmaları ile Dy katkılı anayapıların açık sarı, Sm katkılı anayapıların turuncu ve Tb katkılı anayapıların yeşil renk ışıma yaptığı kanıtlanmıştır.

Anahtar Sözcükler: Lantan ortoborat, Gadolinyum ortoborat, İtriyum ortoborat, disprosyum, terbiyum, samaryum, lüminesans, mikrodalga yardımlı katı hal sentezi.

To my parents Selman and Ayşe and my sister Nagihan and my aunt Şükran

ACKNOWLEDGEMENTS

I wish to express endless gratitude to my advisor Prof. Dr. Ayşen Yılmaz and co-advisor Assoc. Prof. Dr. Okan Esentürk for their guidance with full support, comments and insights as well as patience during this study.

I wish to express my gratitude for Prof. Dr. Ahmet M. Önal and Assoc. Prof. Dr. Ali Çırpan for allowing me to utilize their research laboratories during this project.

I wish to give my dearest appreciation to my lab mates M. Gencay Çelik, Ali Farid, Saeed Vahed Qaramaleki, Ceren Abacı, Zeynep Seda Eren for their support and the shared memories. I also wish to thank my friends Ruşen Ünal, Haldun Topçuoğlu, Hakan Ünay and Gizem Çalışgan Ünay for making my life easier and more peaceful.

And most importantly, I want to give the best love and gratitude to my beloved family and fiancée Günce Bayram.

I wish to express my gratitude for Tübitak for financial support.

TABLE OF CONTENT

ABSTRACT vi

ÖZ viii

ACKNOWLEDGEMENTS xi

TABLE OF CONTENT xii

LIST OF TABLE xiv

LIST OF FIGURE xv

CHAPTERS 1

1. INTRODUCTION 1

1.1 Borates 1

1.2 Phosphors and Luminescence 3

1.2.1 Phosphors 3

1.2.2 Luminescence 4

1.3 Rare Earth Elements 6

1.3.1 Tb^{3+} Ions Luminescence Properties 8

1.3.2 Dy^{3+} Ions Luminescence Properties 10

1.3.3 Sm^{3+} Ions Luminescence Properties 12

1.4 Crystal Structure of Hosts 14

1.4.1 Crystal Structure and IR Investigation of $LaBO_3$ 15

1.4.2 Crystal Structure and IR Investigation of $GdBO_3$ 16

1.4.3 Crystal Structure and IR Investigation of YBO_3 18

1.5 Color and Chromaticity 20

1.6 Synthesis Method 21

2. METARIALS AND METHODS 25

2.1 Materials 25
2.2 Instrumentation 26
2.2.1 Furnace 26
2.2.2. X-Ray Diffractometer 26
2.2.3 Attenuated total reflectance -Fourier Transform Infrared Spectrometer (ATR-FT-IR) 26
2.2.4 Far-IR 26
2.2.5 Scanning Electron Microscope (SEM) 27
2.2.6 Photoluminescence Reader 27
2.3 Experimental Methods 27
2.3.1 Synthesis of $LnBO_3$ 27
3. RESULTS AND DISCUSSION 31
3.1 X-ray Diffraction Patterns 31
3.2 SEM & EDX Results 38
3.3 ATR Results and Spectra 43
3.4 Luminescence Results and Spectra 53
3.5 Far-IR Results and Spectra 61
3.6 CIE results 73
4. CONCLUSION AND RECOMMENDATIONS 81
REFERENCES 84

LIST OF TABLE

TABLES

Table 1: World B_2O_3 Reserves [1]. 2
Table 2: Most Abundant Minerals [1]. 3
Table 3: Compounds used, utilization purposes, labels. 25
Table 4: Mol percent of Dy. 28
Table 5: Mol percent of Sm. 28
Table 6: Mol percent of Tb. 29
Table 7: Weight of used materials. 29

LIST OF FIGURE

FIGURES

Figure 1. Jablonski diagram [21]. 4
Figure 2. Franck-Condon Energy Level Diagram [24]. 6
Figure 3. Energy level of RE^{3+} ions [26]. 7
Figure 4. Emission spectra of $LaBO_3$: Tb at 378 nm by varying Tb doping amount [31]. 9
Figure 5. Energy level diagram of Tb^{+3} between 400 and 600 nm [32]. 10
Figure 6. Emission spectra for lead borate glasses with changing doping Dy^{3+} amount [37]. 11
Figure 7. Energy level diagram for Dy^{3+} ions in lead borate glasses [37]. 12
Figure 8. Emission and excitation spectrum of $LaAlGe_2O_7$: Sm [38]. 13
Figure 9. Energy level diagram for Sm^{3+} ions in $LaAlGe_2O_7$ [38]. 13
Figure 10. Lanthanum orthoborate crystal data and crystal structure refinement [51]. 15
Figure 11. The crystal structure of $LaBO_3$. (Black dots: La, Blue dots: B, Red dots: O) [52]. 16
Figure 12. Planar BO_3^{3-} structure [51]. 16
Figure 13. $GdBO_3$ crystal data and crystal structure refinement [51]. 17
Figure 14. The crystal structure of $GdBO_3$. (Black dots: Gd, Blue dots: B, Red dots: O) [52]. 18
Figure 15. Tetrahedral $B_3O_9^{9-}$ structure [51]. 18
Figure 16. YBO_3 crystal data and crystal structure refinement [51]. 19
Figure 17. The crystal structure of YBO_3 (Black dots: Y, Blue dots: B, Red dots: O) [52]. 19
Figure 18. CIE chromaticity diagram 1931 [55]. 21
Figure 19. X-Ray patterns of undoped and Dy doped $LaBO_3$ samples. 32
Figure 20. X-Ray patterns of undoped and Sm doped $LaBO_3$ samples. 33
Figure 21. X-Ray patterns of undoped and Tb doped $LaBO_3$ samples. 33
Figure 22. X-Ray patterns of undoped and Dy doped $GdBO_3$ samples. 34
Figure 23. X-Ray patterns of undoped and Sm doped $GdBO_3$ samples. 35

Figure 24. X-Ray patterns of undoped and Tb doped $GdBO_3$ samples. 35
Figure 25. X-Ray patterns of undoped and Dy doped YBO_3 samples. 36
Figure 26. X-Ray patterns of undoped and Sm doped YBO_3 samples. 37
Figure 27. X-Ray patterns of undoped and Tb doped YBO_3 samples. 37
Figure 28. SEM images of a) undoped $LaBO_3$ b) Dy doped $LaBO_3$ c) Sm doped $LaBO_3$ d) Tb doped $LaBO_3$ all scale of 5 µm. 38
Figure 29. EDX results a) undoped $LaBO_3$b) Dy doped $LaBO_3$ c) Sm doped $LaBO_3$ d) Tb doped $LaBO_3$. 39
Figure 30. SEM images of a) undoped $GdBO_3$ b) Dy doped $GdBO_3$ c) Sm doped $GdBO_3$ d) Tb doped $GdBO_3$ all scale of 5 µm. 40
Figure 31. EDX results of a) undoped $GdBO_3$b) Dy doped $GdBO_3$ c) Sm doped $GdBO_3$ d) Tb doped $GdBO_3$. 41
Figure 32. SEM images of a) undoped YBO_3 b) Dy doped YBO_3 c) Sm doped YBO_3 d) Tb doped YBO_3 all scale of 5 µm. 42
Figure 33. EDX results of a) undoped YBO_3 b) Dy doped YBO_3 c) Sm doped YBO_3 d) Tb doped YBO_3. 43
Figure 34. ATR spectra of undoped and Dy doped $LaBO_3$ samples. 44
Figure 35. ATR spectra of undoped and Sm doped $LaBO_3$ samples. 45
Figure 36. ATR spectra of undoped and Tb doped $LaBO_3$ samples. 46
Figure 37. ATR spectra of undoped and Dy doped $GdBO_3$ samples. 47
Figure 38. ATR spectra of undoped and Sm doped $GdBO_3$ samples. 48
Figure 39. ATR spectra of undoped and Tb doped $GdBO_3$ samples. 49
Figure 40. ATR spectra of undoped and Dy doped YBO_3 samples. 50
Figure 41. ATR spectra of undoped and Sm doped YBO_3 samples. 51
Figure 42. ATR spectra of undoped and Tb doped YBO_3 samples. 52
Figure 43. PL spectra of Dy doped $LaBO_3$ samples. 53
Figure 44. PL spectra of Sm doped $LaBO_3$ samples. 54
Figure 45. PL spectra of Tb doped $LaBO_3$ samples. 55
Figure 46. PL spectra of Dy doped $GdBO_3$ samples. 56
Figure 47. PL spectra of Sm doped $GdBO_3$ samples. 57
Figure 48. PL spectrum of Tb doped $GdBO_3$. 58

Figure 49. PL spectra of Dy doped YBO_3 samples. 59
Figure 50. PL spectra of Sm doped YBO_3 samples. 60
Figure 51. PL spectra of Tb doped YBO_3 samples. 61
Figure 52. Far-IR spectra of undoped and Dy doped $LaBO_3$ and $DyBO_3$. 63
Figure 53. Far-IR spectra of undoped and Sm doped $LaBO_3$ and $SmBO_3$. 64
Figure 54. Far-IR spectra of undoped and Tb doped $LaBO_3$ and $TbBO_3$. 65
Figure 55. Far-IR spectra of undoped and Dy doped $GdBO_3$ and $DyBO_3$. 66
Figure 56. Far-IR spectra of undoped and Sm doped $GdBO_3$ and $SmBO_3$. 67
Figure 57. Far-IR spectra of undoped and Tb doped $GdBO_3$ and $TbBO_3$. 68
Figure 58. Far-IR spectra of undoped and Dy doped YBO_3 and $DyBO_3$. 69
Figure 59. Far-IR spectra of undoped and Sm doped YBO_3 $SmBO_3$ 70
Figure 60. Far-IR spectra of undoped and Tb doped YBO_3 and $TbBO_3$ 71
Figure 61. Far-IR spectra of boric acid and RE oxides. 72
Figure 62. 5.30 %: Dy doped $LaBO_3$ CIE results 73
Figure 63. 2.12 %: Sm doped $LaBO_3$ CIE results. 74
Figure 64. 2.12 %: Tb doped $LaBO_3$ CIE results. 75
Figure 65. 5.73 %: Dy doped $GdBO_3$ CIE results. 76
Figure 66. 5.30 %: Sm doped $GdBO_3$ CIE results. 77
Figure 67. 5.30 %: Dy doped YBO_3 CIE results. 78
Figure 68. 5.30 %: Sm doped YBO_3 CIE results. 79
Figure 69. 5.30 %: Tb doped YBO_3 CIE results. 79

CHAPTERS

1. INTRODUCTION

1.1 Borates

Boron is in the third group of the periodic table with the atomic number of 5. It has two stable isotopes with the mass numbers 10 and 11. Boron isotope with the atomic number 10 is used in nuclear power plants as a neutron capturer. Boron is the single nonmetal element in group IIIA of the periodic table. Boron behaves as a nonmetal in its compounds, whereas it behaves like Carbon in elemental form, conducting electricity. At room temperature, its conductivity is poor. Conductivity increases with increasing temperature. At the first glance, boron mineral appears as a white rock, very hard and resistant to heat. It is found in nature as salt crystals. Its elemental form is a brown amorphous powder. However, its monoclinic crystal form is hard, brittle and yellowish brown. When heated in air, it burns with a green flame, forming B_2O_3 [1]**.**

Boron containing minerals are collectively called borates. The industrial standing of boron minerals and compounds is increasing worldwide. They have various different usages such as detergents, toothpaste, insecticides and rocket fuels. Boron nitrite, which acts as an insulator towards electricity, acts as a conductor of heat like a metal. It is hardening for any material it is mixed with [2, 3]**.**

More often than not, boron is found as borosilicate or borate minerals in nature, 230 of which are identified [4]**.** The reserves and production of boron in Russia and Turkey are leading in the world. The total boron reserves of the world are estimated as 1.312.300 thousand tons as of 2014 given in **Table 1**. Among these reserves, a leading percentage of 72.8 % is in Turkey [1]**.**

Table 1: World B_2O_3 Reserves [1].

Countries	**Total Reserves (Thousand tons B_2O_3)**	**Distribution (%)**
Turkey	955.300	72.8
U.S.A [2, 5]	80.000	6.1
Russia [5]	100.000	7.6
China [5]	47.000	3.6
Argentina [2, 5]	9.000	0.7
Bolivia [2, 6]	19.000	1.4
Chile [2, 6]	41.000	3.2
Peru [5]	22.000	1.7
Kazakhstan [6, 7]	15.000	1.2
Serbia [6]	24.000	1.7
Total	1.312.300.100	

Boron minerals occur naturally with different amounts of boron oxide (B_2O_3) in their structure. Although there are virtually 230 of them, the most economically significant boron minerals list as tincal, colemanite, kernite, ulexite, pandermite, boracite, szaybelite and hydroboracite. **Table 2** shows the chemical formulas and B_2O_3 content of these minerals. In Turkey, there are sodium based tincal, calcium based colemanite and sodium+calcium based ulexite. These minerals are first enriched in physical procedures (concentrated boron) and then refined to form various boron chemicals. All of these products are referred to as boron for convenience [1].

Table 2: Most Abundant Minerals [1].

Minerals	Formula	Content B_2O_3 %
Colemanite	$Ca_2B_6O_{11}.5H_2O$	50.8
Ulexite	$NaCaB_5O_9.8H_2O$	43.0
Tincal	$Na_2B_4O_7.10H_2O$	35.5
Kernite	$Na_2B_{14}O_7.4H_2O$	51.0
Pandermite	$Ca_4B_{10}O_9.7H_2O$	49.8
Hydroboracite	$CaMgB_6O_{11}.6H_2O$	50.5

1.2 Phosphors and Luminescence

1.2.1 Phosphors

The word phosphor, first given in 17th century, has originated from Greek and has kept its meaning so far. Phosphor is also defined as a light-emitting, shining (luminescent) matter [8]. Phosphors are solid materials usually formed by addition of impurities such as rare earth elements into inorganic host materials. In other words, phosphor is any material that can absorb energy and emit it as visible light. The impurity level in phosphors is usually chosen to be low because concentration quenching decreases luminescence yield at high concentrations. Concentration quenching occurs when dopant amount increases inside inorganic host and luminescence intensity begin decrease. Phosphors are usually white and it prevents visible light from being absorbed by the phosphors [9].

Luminescent materials known as phosphors can absorb energy from radiation and emit it as light after a series of energy transfer events. These emissions usually fall in the visible region however they might also be in the ultraviolet [10] or infrared region [11-15]. An average human eye is only sensitive to visible light between 380 and 750 nm and sensitivity peaks at 555 nm [16]. Thus, phosphors that are radiating in visible region are mostly used commercially. Phosphors can be edited in terms of morphology and particle size to fit the needs in various application areas [17]. Long life lightening phosphorescence materials are used daily in UV lamps, high and low pressure mercury

lamps, billboards, x-ray applications, cathode ray tubes like television, product coding [18].

1.2.2 Luminescence

The term luminescence, which means electromagnetic radiation emitted from phosphors with the aid of a suitable excitation source, is first used by German physicist Eilhard Wiedemann to characterize light emission without any changes in the temperature of the sample. It is called "cold light"; opposite of incandescence which is light emitted by a substance as a result of heating [19].

Alexander Jablonski findings' suggested that whenever energy is supplied to a molecule, the molecule is excited and its electronic energy levels are elevated [20]. The essential pathways are given in **Figure 1** (Jablonski diagram) according to which whenever a molecule absorbs energy, it returns to ground state by only one way. This way can be phosphorescence, fluorescence, internal conversion or Intersystem crossing.

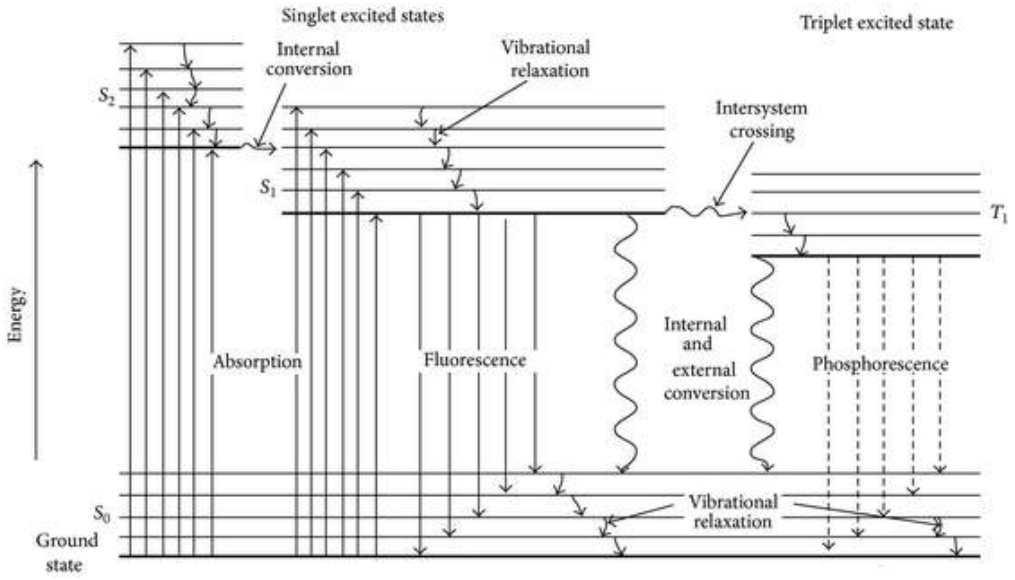


Figure 1. Jablonski diagram [21].

Fluorescence and phosphorescence are alike in terms of the excitation that occurs by absorption of photons. As a result, these two phenomena are usually referred to as photoluminescence, a broader term. Fluorescence differs from phosphorescence by the

fact that the electronic energy transmission responsible for fluorescence does not make a difference in the spin of the electron. As a result, fluorescence is a short-lived luminescence that vanishes instantly. However, a change in the electron spin related to phosphorescence emissions lasts for an easily detectable period of time after irradiation ends; a few seconds, if not more. Fluorescence occurs in simple or complicated solid, liquid or gas chemical systems. The simplest form of fluorescence is the fluorescence from dilute atomic vapors. For example, the 3s electrons of sodium atoms in vapor phase, can be excited to 3p energy level by absorption of light at the wavelengths 589.6 and 589 nm. After 10^{-5} to 10^{-8} seconds, electrons return to ground state and radiate in the same two wavelengths towards all directions. This type of fluorescence that involves emission of absorbed radiation without changes in wavelength is named resonance radiation or resonance fluorescence. Many molecular species exhibit resonance fluorescence as well. In addition, very commonly, molecular fluorescence or phosphorescence bands are found in higher wavelengths than resonance. This shift towards higher wavelengths or lower energies is called stokes shift. The energy loss from an excited electronic state can also be by phosphorescence. Singlet-singlet transition occurs more commonly than triplet-singlet transition. Therefore, the average lifetime of triplet form is rather high. Thus, emission resulting from such a crossing can last a while longer after the irradiation ends. In **Figure 2**, the configurational energy diagram of ground and excited states is seen where no trapped electrons are present [22, 23].

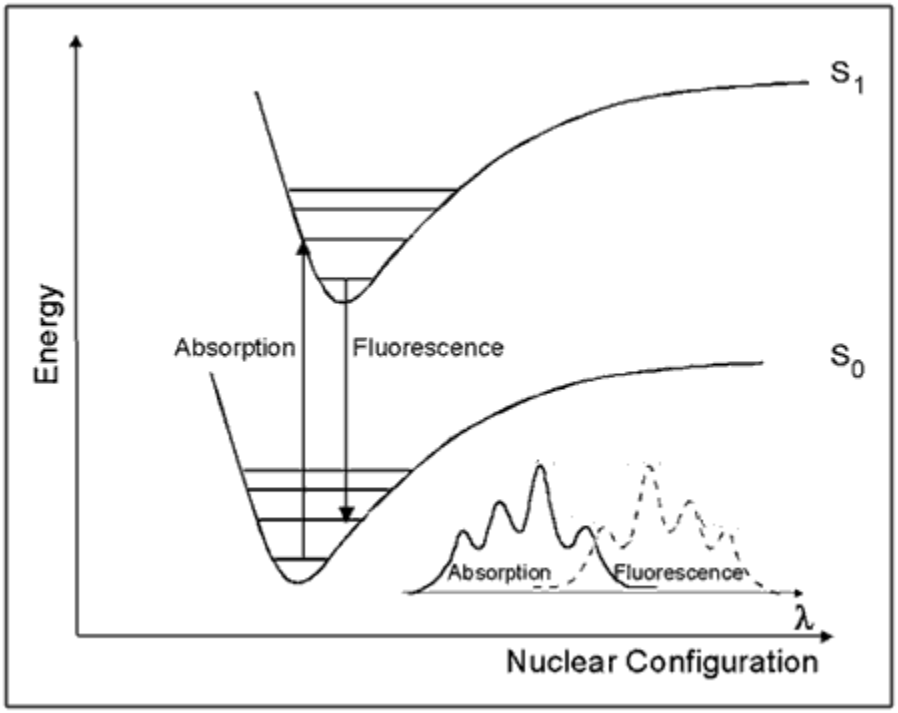


Figure 2. Franck-Condon Energy Level Diagram [24]**.**

1.3 Rare Earth Elements

Elements beginning from La with atomic number 57 to Lu with atomic number 71 make up rare earth elements, usually with the addition of Sc with atomic number 21 and Y with atomic number 39. Their incompletely filled 4f shell is an advantageous property and they demonstrate distinctive characteristics magnetically, electrically and optically. The $5s^2$ and $5p^6$ electrons protect the 4f electrons from the environment in these elements. Thus, the 4f configuration's optical transitions are not majorly affected by the surroundings or the crystal electric field. Dieke [25] as well as further researchers [26] have looked into the energy levels of 4f electrons of the trivalent rare earth ions (RE^{3+}) comprehensively. The Dieke diagram is seen in **Figure 3**. Experimental energy state determination was carried out, taking the optical spectra of ions integrated in $LaCl_3$ crystals into consideration. The semi-circles under the bars designate light emitting levels. The order of magnitude of the crystal field splitting, which is rather small, is determined by the examination of the thickness of the energy state bars. The 4f electrons do not usually interact with the electric field in the surroundings, so the diagram is valid for ions in virtually any host lattices. The highest

discrepancy of the energy states is very restrained and is of the order of several hundred cm^{-1} at most.

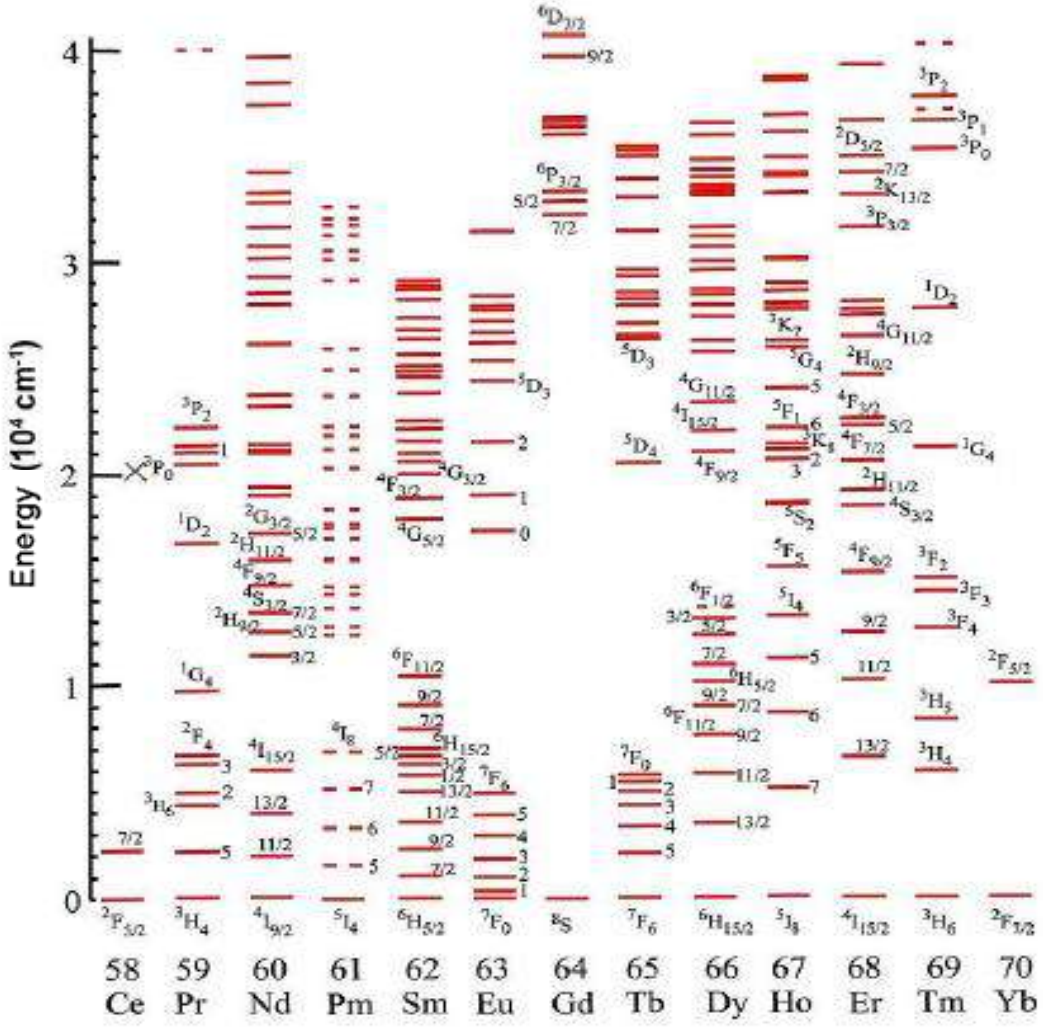


Figure 3. Energy level of RE^{3+} ions [26]**.**

The discrete 4f energy level numbers are high, excluding Ce^{3+} and Yb^{3+}. There are up to 327 levels of 4f configuration in Gd^{3+}, which increase more on account of crystal field splitting. Usually, the levels about the photoluminescence which are possible to be excited by ultraviolet light as well as other levels are overlooked. Since no changes in parity occur, transitions are severely forbidden from occurring within 4f shells. Since the interaction of rare earth ion with lattice vibrations or crystal field might mix the state of separate parities into 4f states, the forbidden transitions occur. An increase of the even parity transition amplitudes for the transitions within the 4f shell is brought

on by the coupling of 4f electrons with temporary dipoles. Induced electric dipole transition is the name given to these transitions. Oscillation strengths related with the surroundings and corresponding selection rules (S = 0, L ≤ ±2 and J ≤ ±2) shows great diversity. The transitions are forbidden for electric dipole, while they are allowed for magnetic dipole. The selection rules L = 0, S =0, I = 0 and J = 1(0 → 0 excluded) are obeyed by the magnetic dipole transitions. The selection rules on S and L are weakened by spin orbit coupling. Different parities' 4f states may be mixed by the rare earth ions' interactions with lattice vibrations. The combination of $4f^n$ state with the vibrational mode of the lattice lead to the vibrational transitions of rare earth ions [22].

The term symbol is briefly explained by angular momentum quantum numbers in a multi-electron atom. 2S+1 is multiplicity, L is total orbital angular momentum, and J is total angular momentum. S is composed of all the spins combine, L is produced from all orbital angular momenta couple, J is sum of the spin and orbital terms. Notation system is $^{2S+1}L_J$. The calculated term symbols obey Hund's rule and Pauli Exclusion Principle [27].

1.3.1 Tb^{3+} Ions Luminescence Properties

The transitions $^5D_4 \rightarrow {}^7F_J$ (J=0-6), which is in the green region mostly, and of $^5D_3 \rightarrow {}^7F_J$ which is in the blue, make up the emission spectrum. The ratio of blue to green mostly relies on the concentration of Tb^{+3}, owing to the cross relaxation effect among two adjacent Tb^{+3} pairs: Tb^{3+} ($^5D_3$) + Tb^{3+} ($^7F_6$) → Tb^{3+}($^5D_4$) → Tb^{3+} ($^7F_0$), a situation which is observed in numerous host crystals [28-30]. The intensity ratio of blue to green is further dependent on the host crystals in two ways. Firstly, the phonon induced relaxation caused by maximum phonon energy affects this ratio. The higher the maximum phonon energy, the lower the ratio. Secondly, the relative position of the $4f^75d^1$ and $4f^8$ energy level affects this ratio. An electron is excited to $4f^75d^1$ might return straight to the $^5D_4$ and it then bypasses the $^5D_3$ and as a result, produces $^5D_4$ luminescence only.

In a luminescence study of $LaBO_3$: Tb in which the amount of doped Tb is changed by 2.5,5,7.5,10 mol percent, the maximum absorption was found to be at 378 nm. Here, the excitation spectra were kept under 543 nm, the emission wavelength [31].

Figure 4 shows the emission spectrum of $LaBO_3$: Tb at 378 nm. The best emission intensity for $LaBO_3$: Tb was determined by luminescence studies to be 5 % moles.

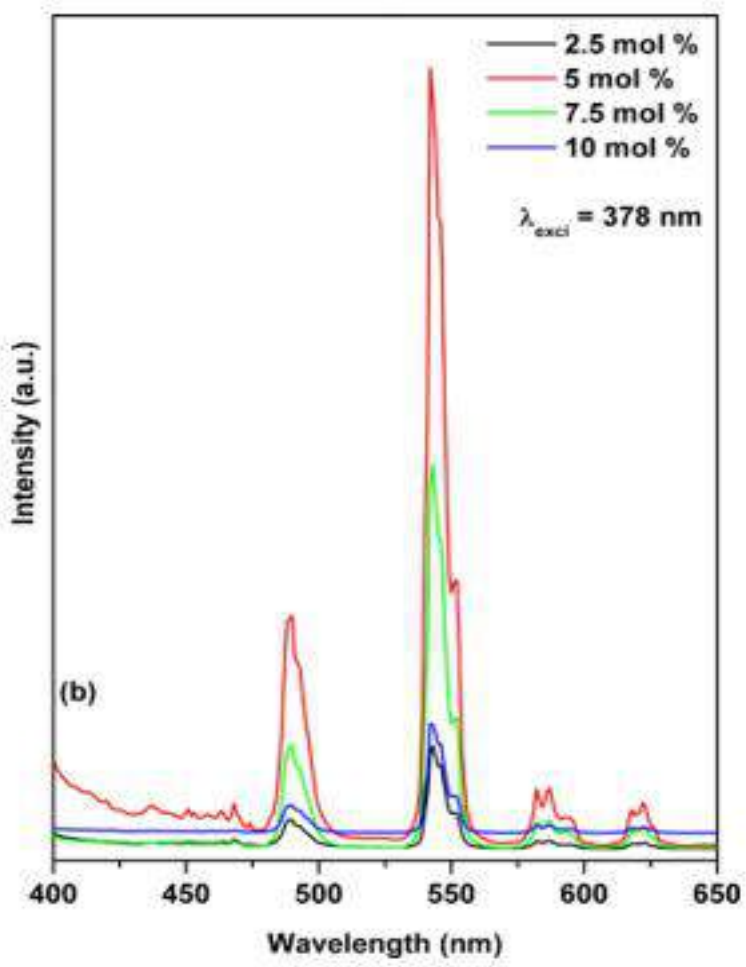


Figure 4. Emission spectra of $LaBO_3$: Tb at 378 nm by varying Tb doping amount [31]**.**

In a similar study by Zhang et al. on Eu and Tb with 1,10-phenanthroline in situ synthesized in a silica matrix, one doping material in various matrixes was determined to have different excitation numbers. Approximately similar wavelengths (612 nm for Eu, 544 nm for Tb), gave maximum emissions regardless of the excitation wavelength **Figure 5** [32]**.**

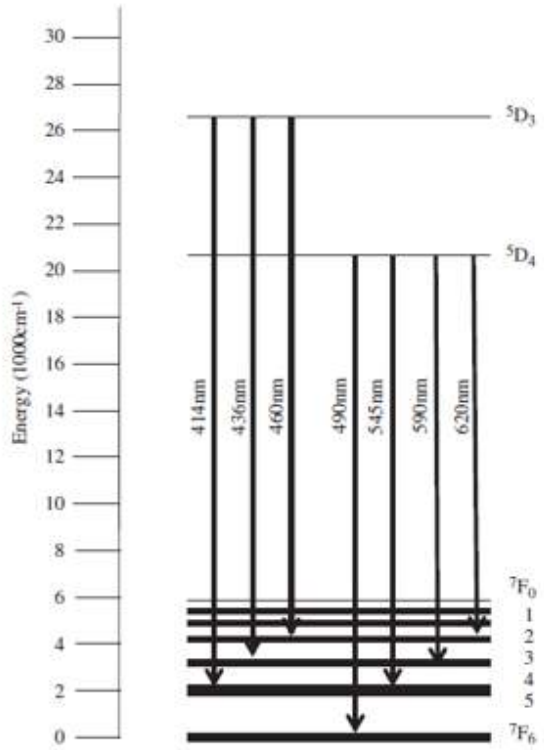


Figure 5. Energy level diagram of Tb^{+3} between 400 and 600 nm [32]**.**

1.3.2 Dy^{3+} Ions Luminescence Properties

Dy^{+3} ion shows potential among all other rare earth ions in applications including white light. The reason for this is the transition between $^4F_{9/2} \rightarrow {}^6H_{15/2}$ and $^4F_{9/2} \rightarrow {}^6H_{13/2}$ energy levels matching the dominant emission bands at respectively blue and yellow region [33]. Ligand field affects the $^4F_{9/2} \rightarrow {}^6H_{13/2}$ emission band, which occurs because of the electric dipole transition, strongly. The $^4F_{9/2} \rightarrow {}^6H_{15/2}$ emission occurs because of the magnetic dipole transition [34]. CIE 1931 chromaticity diagram most commonly shows white light region when yellow and blue regions overlap. Also, the intensity ratio of yellow to blue can be adjusted to produce white light from glass materials. The intensity ratio of yellow to blue (Y/B) can be adjusted by changing the rare earth ion concentration, glass composition and excitation wavelengths [35, 36].

Luminescence spectra of Dy^{+3} ions in lead borate glasses are seen in **Figure 6**. Dy^{+3} ion concentration was analyzed with luminescence. These spectra were collected while the sample was excited at 386 nm ($^4K_{17/2}$ state) or 450 nm ($^4I_{15/2}$ state) lines. Regardless

of excitation wavelengths, three peaks were observed. These are: 480 nm, 573 nm and a less intense band at 662 nm.

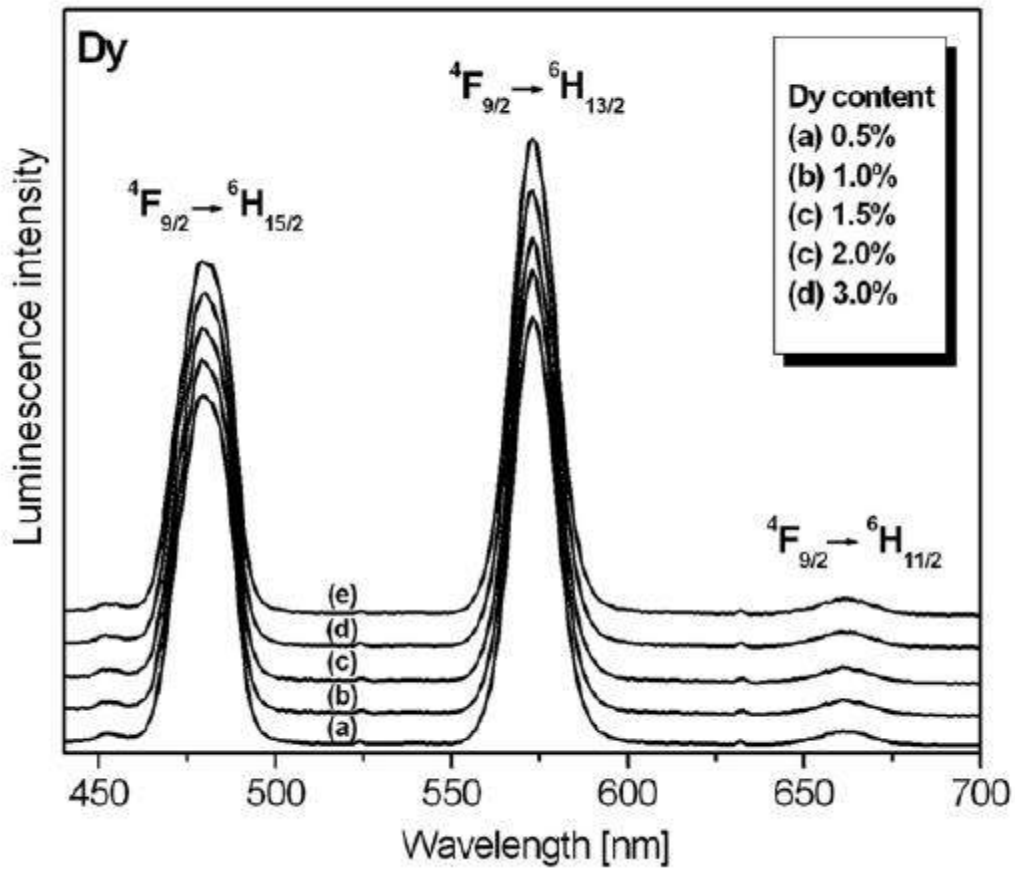


Figure 6. Emission spectra for lead borate glasses with changing doping Dy^{3+} amount [37].

Respectively, their transitions are $^4F_{9/2} \rightarrow {}^6H_{15/2}$ (blue), $^4F_{9/2} \rightarrow {}^6H_{13/2}$ (yellow) and $^4F_{9/2} \rightarrow {}^6H_{11/2}$ (red). These transitions show the energy level of Dy^{3+} ions in lead borate glass **Figure 7**. The region above 21 000 cm^{-1} is highly populated because of non-radiative relaxation. Follow yellow and blue luminescence, which are rather strong, resulting from the $^4F_{9/2}$ state. This situation results from large gap (~6000 cm^{-1}) between the $^4F_{9/2}$ state and the following $^6F_{1/2}$ state [37].

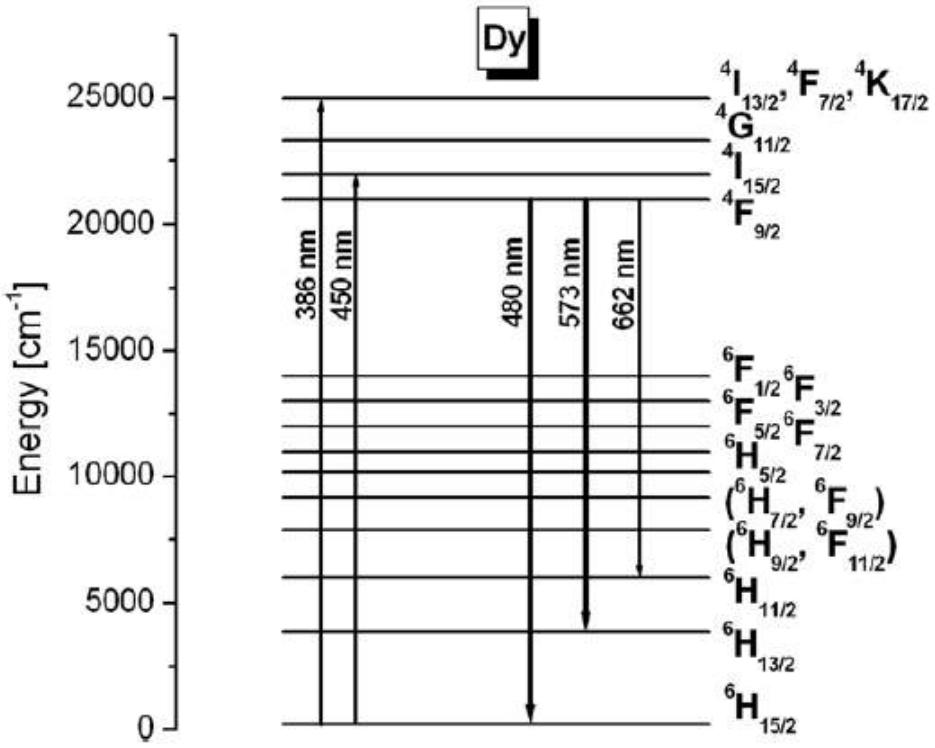


Figure 7. Energy level diagram for Dy^{3+} ions in lead borate glasses [37].

1.3.3 Sm^{3+} Ions Luminescence Properties

Sm^{+3}, having $4f^5$ configuration, possesses intricate energy level structure and has a variety of possible transitions between f levels. These transitions between f levels are sharp lines. **Figure 8** shows emission and excitation spectra of $LaAlGe_2O_7$: Sm. Sm^{+3} ions' ground level is $^6H_{5/2}$ and all excitation peaks result from that. Result of f-f transition of Sm^{+3} show several sharp peaks. Three emission bands of Sm^{+3} (563 nm, 595 nm, 641 nm) are responsible from the red-orange hued light of Sm^{+3}. The intra-4f-shell transitions from excited level $^4G_{5/2}$ respectively to ground levels $^6H_{5/2}$, $^6H_{7/2}$ and $^6H_{9/2}$, are given to these bands **Figure 9** [38].

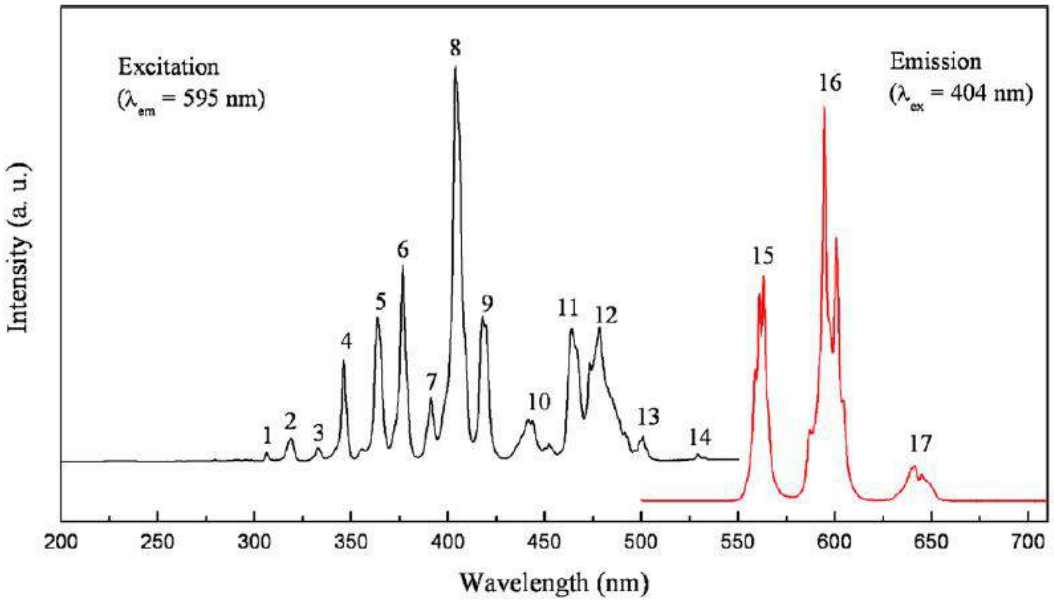


Figure 8. Emission and excitation spectrum of $LaAlGe_2O_7$: Sm [38]**.**

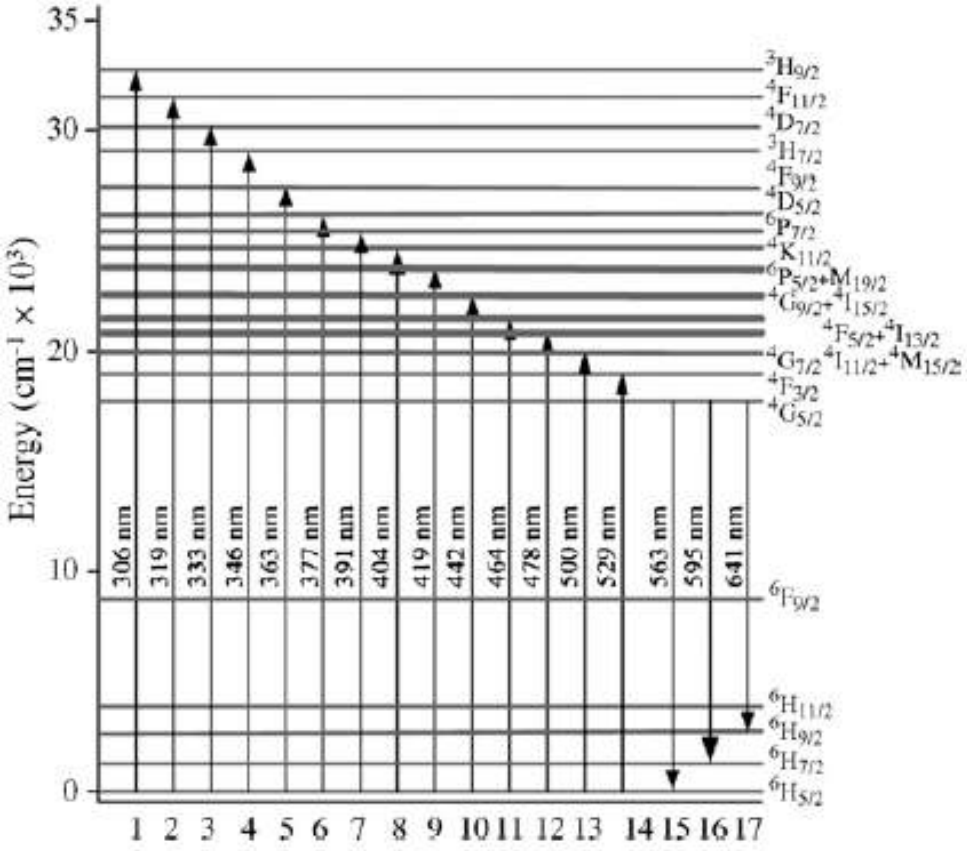


Figure 9. Energy level diagram for Sm^{3+} ions in $LaAlGe_2O_7$ [38].

1.4 Crystal Structure of Hosts

There are several host materials such as phosphates, aluminates, titanates and borates. We used borates as host materials since borates are the most abundant materials in our country and they are few studies on them.

Phosphates are important luminescent materials since they have excellent thermal stability and their tetrahedral rigid three dimensional matrixes are proper for charge stabilization. $KSrPO_4$ doped with Eu^{2+} materials are at range of blue emission display [39].

Aluminates are very important hosts for materials science since REE doped strontium aluminate phosphors have high chemical stability and luminescent properties [40]. In addition, titanates are significant host for phosphorescent. $CaTiO_3$: Pr^{3+} was first reported as hopeful phosphorescent material at range of red field emission display, in 1994 [41]. The fluorescence of europium doped silicate was studied and $R_xSi_yO_z$ system R: Ca, Sr, Ba give very bright absorption bands at 435-600 nm in visible range, very high productivity of excitation in UV [42].

A study by Levin et al on the simplest Lanthanide orthoborates, $LaBO_3$, was published in 1961. According to the study, depending on the rare earth, there is strong connection between the structure of rare earth borate and the three crystalline forms of $CaCO_3$, i.e., vaterite, calcite and aragonite types [43]. Aragonite type structure is displayed by the light rare earth orthoborates and vaterite type structure is displayed by the heavy elements of the Lanthanide group. Nonetheless, currently five crystal structures (based on previously described crystalline forms) of the RE orthoborates are known: the hexagonal vaterite type (space group P63/m, No. 176) [44,45], the orthorhombic aragonite type (Pnam, No. 62) [44,46], the rhombohedral vaterite type (R32, No. 155) [47], and the rhombohedral calcite type (R3c, No. 161) [48] and monoclinic pseudo wollastonite type (C2/c, No.15) [49,50]. It is very important to notice that BO_3^{3-} triangles are different from the standard $CaCO_3$ vaterite [49].

1.4.1 Crystal Structure and IR Investigation of $LaBO_3$

The result of the Rietveld refinements of $LaBO_3$ is summarized in **Figure 10** [51]. The $LaBO_3$ crystallize in orthorhombic system with the following refined unit cell parameters at room temperature a=5.8761(1) Å, b=5.10535(9) Å, c=8.252(1) Å. The refinement leads to the residual values of Rp=0.0844, Rwp=0.1076 [52]. The crystal structure of $LaBO_3$ was obtained from these refinement results and crystal structures were given in **Figure 11** by using Diamond (2000-2006) [53]. Trigonal BO_3^{3-} anions are easily seen in this orthorhombic structure in **Figure 12**.

Emprical Formula	$LaBO_3$
Molar mass	197.7 g/mol
Crystal System	Orthorhombic
Space Group	*Pnma*
Powder diffractometer	Panalytical X'Pert Pro
Radiation	CuKα(λ=1.54051Å)
Unit-cell dimensions	a=5.8761(1) Å
	b=5.10535(9) Å
	c=8.252(1) Å
Volume	247.570 (8) $Å^3$
Step (°)	0.013
2 Theta Range	10-150 °
R_{wp}	0.1076
R_p	0.0844
χ^2	5.101

Figure 10. Lanthanum orthoborate crystal data and crystal structure refinement [51]**.**

Aragonite type of orthoborates $LaBO_3$ has vibration modes which can be described as follows: ν3 (asymmetric stretching) in the region 1100 and 1400 cm^{-1}, ν1 (symmetric stretching) near 940 cm^{-1}, ν2 (out of plane bending) in the region 700-800 cm^{-1}, and ν4 (in-plane bending) below 670 cm^{-1}. For these compounds it is clear that boron atoms are in threefold coordination. The observed frequencies between 1350 and 1150 cm^{-1} range correspond to the stretching frequencies of a coordinated BO_3^{3-} group [54].

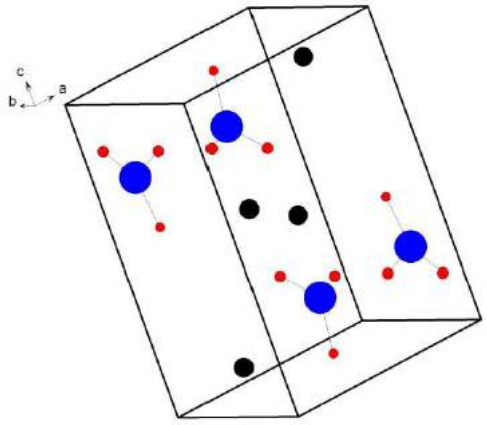


Figure 11. The crystal structure of $LaBO_3$. (Black dots: La, Blue dots: B, Red dots: O) [52]**.**

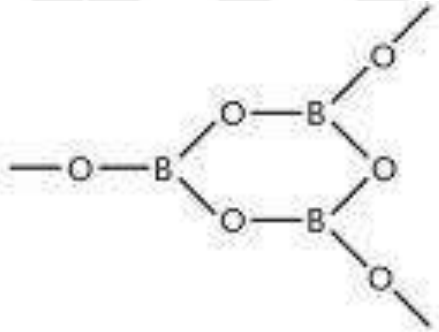


Figure 12. Planar BO_3^{3-} structure [51].

1.4.2 Crystal Structure and IR Investigation of $GdBO_3$

Since the space group work of vaterite structure is problematic, in a study by Seyyidoğlu et al. they used the all possible space groups mentioned before to find out the best possible space group. All attempts were failed and the refinements generally diverges for other space groups for $GdBO_3$. Only possible space group is $R3_2$ as mentioned in Ren et al. (1999). In this work, the phase purity of $GdBO_3$ powder samples was examined by X-ray diffraction. They derived the rhombohedral lattice constants from electron diffraction and refined from X-ray diffraction pattern, are a=6.6357(2) Å and c=26.706(1) Å. They could not identify the boron atoms from the refinement, because their scattering power is too small [47].

Figure 13 summarized the results of the Rietveld refinement of $GdBO_3$. Diamond (2000-2006) software program was used to draw crystal structure of $GdBO_3$ and the structure is given in **Figure 14** [52]. The bands between 1150-1350 cm^{-1} are not seen in the FTIR spectra of $GdBO_3$. The IR absorption peaks between 900 and 1050 cm^{-1} are those typical for the tetrahedral borate group BO_4 (Ren et al. 1999) and our results are consistent with these and $LnBO_3$ (Ln=Y, Gd, Tb, Yb) products are composed of $B_3O_9^{9-}$ in their structure in **Figure 15** [47].

Emprical Formula	$GdBO_3$
Molar mass	216.1 g/mol
Crystal System	Rhombohedral
Space Group	$R3_2$
Powder diffractometer	Panalytical X'Pert Pro
Radiation	CuKα(λ=1.54051Å)
Unit-cell dimensions	a=6.63899(8) Å
	c=26.7219(5) Å
Volume	1020.00 (2) $Å^3$
Step (°)	0.013
2 Theta Range	10-150 °
R_{wp}	0.0454
R_p	0.0320
χ^2	2.590

Figure 13. $GdBO_3$ crystal data and crystal structure refinement [51]**.**

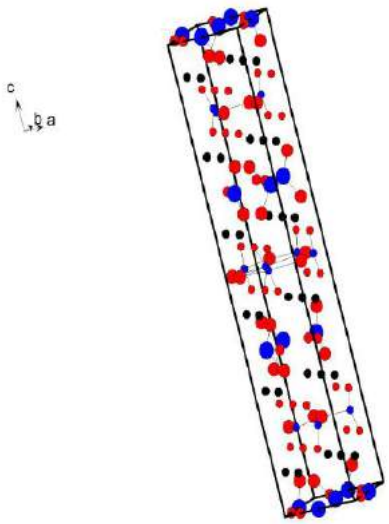


Figure 14. The crystal structure of $GdBO_3$. (Black dots: Gd, Blue dots: B, Red dots: O) [52]**.**

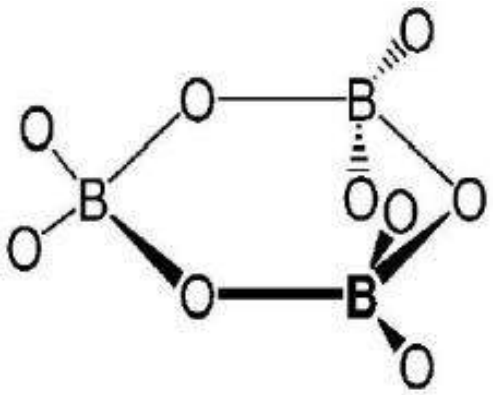


Figure 15. Tetrahedral $B_3O_9^{9-}$ structure [51].

1.4.3 Crystal Structure and IR Investigation of YBO_3

The refined unit cell parameters for YBO_3 at room temperature are a=11.3276(3), b=6.5444(2) Å, c=9.5589(1) Å, β=112.955(1) º, V=652.512 (9) $Å^3$. The results of the Rietveld refinement of YBO_3 are summarized in **Figure 16** [51]. These refinement results were used to draw crystal structure of YBO_3 by using Diamond (2000-2006) software and the structure is given in **Figure 17** [52]. The same structure with Lin et al. (2004) was obtained and $B_3O_9^{9-}$ anions are seen in this monoclinic cell [49].

Emprical Formula	YBO_3
Molar mass	147.7 g/mol
Crystal System	Monoclinic
Space Group	*C2/c*
Powder diffractometer	Panalytical X'Pert Pro
Radiation	CuKα(λ=1.54051Å)
Unit-cell dimensions	a=11.3276(3) Å
	b=6.5444(2) Å
	c=9.5589(1) Å
	β=112.955(1)°
Volume	652.512 (9)$Å^3$
Step (°)	0.013
2 Theta Range	10-150 °
R_{wp}	0.0421
R_p	0.0301
χ^2	3.289

Figure 16. YBO_3 crystal data and crystal structure refinement [51].

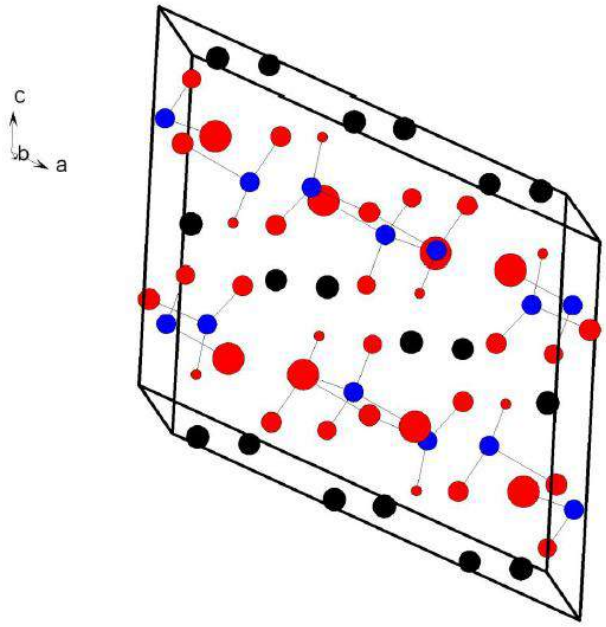


Figure 17. The crystal structure of YBO_3 (Black dots: Y, Blue dots: B, Red dots: O) [52]**.**

The bands between 1150-1350 cm^{-1} are not seen in the FTIR spectra of $GdBO_3$. The IR absorption peaks between 900 and 1050 cm^{-1} are those typical for the tetrahedral

borate group BO_4 (Ren et al. 1999) and our results are consistent with these and $LnBO_3$ (Ln=Y, Gd, Tb) products are composed of $B_3O_9^{9-}$ in their structure [47].

1.5 Color and Chromaticity

The chromaticity diagram of CIE gives a broad color range. CIE diagram was used while color coordinates of light were being identified. Diagram shows the equal energy white point with a coordinates of x=0.33, y=0.33. A white colored region is also present, being regarded as white light [55].

Three primaries red, green, blue compositions are most commonly described with the CIE method (Commission International de I'Eclairage). Real spectral colors can be produced by the addition of artificial "colors", indicated by X, Y, Z. Mathematically, the sum of three quantities (x, y, z) always equal to 1; so in order to define a color, it is sufficient to only give the reference stimuli quantity. Coordinates of chromaticity are the x, y, z, i.e. three tristimulus values are sum of the ratios of X, Y, Z equation 1.1-1.2-1.3.

Description of light source colors. A light source the tristimulus values are (X, Y and Z). It has a spectral energy distribution P(λ).

$$X = K \int_{380}^{780} \mathrm{P}(\lambda)\bar{x}(\lambda)\mathrm{d}\lambda \quad (1.1)$$

$$Y = K\mathrm{P}(\lambda)\bar{y}(\lambda)\mathrm{d}\lambda \quad (1.2)$$

$$Z = K \int_{380}^{780} \mathrm{P}(\lambda)\bar{z}(\lambda)\mathrm{d}\lambda \quad (1.3)$$

$$K = \frac{1}{\mathrm{P}(\lambda)\mathrm{Y}(\lambda)\mathrm{d}\lambda}$$

And x(λ), y(λ) and z(λ) are the spectral stimulus values for 2^o. These quantities are written as $x_{10}(\lambda)$, $y_{10}(\lambda)$ and $z_{10}(\lambda)$ for 10. Color coordinates of light source x and y are calculated with the following formulas equation 1.4.1-1.4.2.

$$x = \frac{X}{X+Y+Z} \quad (1.4.1)$$

$$y = \frac{Y}{X+Y+Z} \quad (1.4.2)$$

The CIE chromaticity diagram is seen in the **Figure 18**. Here, the ISCC-NBS (Inter-Society Color Council-National Bureau of Standard) color label for every color is specified [56].

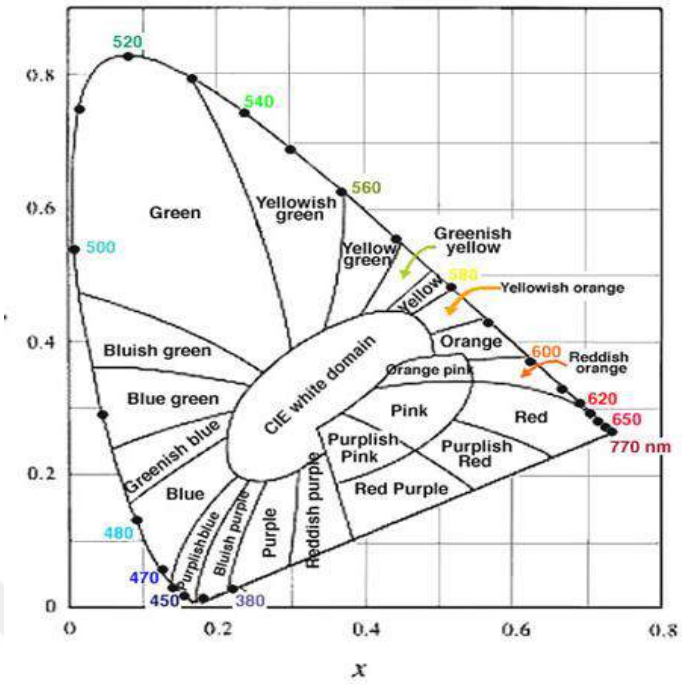


Figure 18. CIE chromaticity diagram 1931 [55].

1.6 Synthesis Method

Microwave assisted synthesis, sol-gel process, high temperature synthesis, hydrothermal synthesis, and combustion synthesis are a few methods for RE orthoborate synthesis [57]. The ultimate purpose is to identify the method with the lowest energy usage and the highest efficiency.

Combustion synthesis is efficient and cost effective. It is used for a wide variety of industrial processes [58]. On the other hand, it yields a high porosity in the product. [59]. Hydrothermal synthesis is advantageous in the sense that it begins the formation of crystals that form crystalline phases which aren't otherwise stable at melting points. However, this crystal formation beginning cannot be observed easily and the "autoclaves" are very expensive. Another risk is the explosion that comes with the handling of autoclaves used in the process [60]. A high crosslink degree can be achieved in high temperature synthesis method which considerably improves mechanical and thermal stability of the product [61]. However, energy consumptions are high in this method [62]. The sol-gel process has the following benefits; high purity end products, possibility of organic-inorganic materials that do not naturally exist,

association of the solid colloidal state with a liquid medium, and finally the possibility of monitoring the kinetics of other materials at low temperatures. Yet, the precursors that are used in the process are very costly, especially for the alkoxides. Using relatively cost effective precursors, this method is beneficial [63].

An important factor to control the size and crystallinity of powder solid is sintering treatment. Microwave-assisted sintering is a novel synthesis method in the quickly developing research area. Microwave-assisted sintering is advantageous in the sense that it consumes a smaller amount of energy and reduces the activation energy, thus reducing the sintering temperatures of the phosphors, as compared with conventional sintering treatments. Even some phosphors prepared by microwave-assisted sintering have been reported in recent years [64,65]. In a microwave synthesis, sources are heated over the whole sample quickly and uniformly, because microwave energy is immediately absorbed by the sample. Therefore, microwave heating techniques offer a noteworthy benefit of decrease in manufacturing costs, i.e., shorter processing time and energy saving. In addition, it is possible to heat a particular component in the mixtures. There are several advantages in microwave heating compared with conventional heating techniques, in view of potentials for (a) synthesis of new materials, (b) improved or unique microstructures and properties, (c) improved product uniformity and yields, and (d) energy saving and shorter processing time.

Microwaves heat the solids two ways. When particles can freely move through the matters, these particles can produce an oscillating electric current so some energy transfers to the surrounding as heat because of the movement resistance. This way is called conduction heating. However, molecules-particles have dipole moments, they are not move freely. Dipoles which do not align, cannot respond instantly when electric field of the radiation fluctuates very quickly. Under these situations, changing electric field causes that microwave radiation is absorbed from solid and these energies are transfer to surrounding as heat. This is dielectric heating. This way of heating related with dielectric constant. Dielectric constant decides how capably the absorbed radiation is transformed to heat [66].

Using microwave processing, various phosphors have been synthesized. The high efficiency phosphors developed for field emission displays, plasma displays, and white

light emitting diodes (LED) tend to be degraded by the operating environment and/or the devices' manufacturing conditions. The temperature of the sample which was monitored with an optical pyrometer, was controlled by adjusting the input power. During the microwave processing, the sample was rotated horizontally about the axis. The samples were heated with a microwave and held at the designed temperatures for typically 10–20 min. The microwave-synthesized products were characterized for particle size, brightness, phase composition, morphology, luminescence emission, and color coordinates. Optimization of the parameters is required to achieve desired properties [22, 67].

OBJECTIVE

In this study, it was aimed to examine the luminescence properties of Dy, Sm, Tb doped $LaBO_3$, $GdBO_3$, YBO_3 samples and to investigate the effect of doping percent on luminescence intensity. In order to understand those, samples were synthesized with microwave assisted solid state synthesis method and different types and amounts of doping agents were used.

2. METARIALS AND METHODS

2.1 Materials

The compounds utilized in this study in synthesis and doping of $LaBO_3$, $GdBO_3$, and YBO_3 are given in **Table 3**.

Table 3: Compounds used, utilization purposes, labels.

Material Used	Utilization Purpose	Labels and Code
La_2O_3	$LaBO_3$ production	Aldrich 99.9% (21,161-3)
Gd_2O_3	$GdBO_3$ production	Acros organics 99.9% (315511000)
Y_2O_3	YBO_3 production	Aldrich 99.9% (20,516-8)
H_3BO_3	$LnBO_3$ production	Merck (100165)
$CO(NH_2)_2$ (Urea)	$LnBO_3$ production	Merck (108487)
Dy_2O_3, Tb_4O_7, Sm_2O_3	Doping agent	Aldrich 99.9% (28,926-4) (22,867-2) (253952)

2.2 Instrumentation

2.2.1 Furnace

Protherm furnace PLF 130 6 with control panel that can heat up to 1300 °C has been used in this study. The annealing and further heating procedures have been carried out in this furnace.

2.2.2. X-Ray Diffractometer

The crystal structures of the undoped and doped $LnBO_3$ samples were obtained by the powder X-ray diffraction (XRD) measurements. The XRD data were recorded using Rigaku X-Ray Diffractometer (Miniflex) with CuKα (30kV, 15mA, λ= 1.54 Å).
The 2 theta range adopted for the XRD examinations were determined to between 5° and 90°. The scan speed was set to 1 degree per/min. Diffraction patterns were assigned using Joint Committee on Powder Diffraction Standards (JCPDS) cards supplied by the International Centre for Diffraction Database (ICDD) card numbered for $LaBO_3$: 12-0762, $GdBO_3$: 13-0483, YBO_3: 88-0356.

2.2.3 Attenuated total reflectance -Fourier Transform Infrared Spectrometer (ATR-FT-IR)

Attenuated total reflectance-FTIR (ATR-FTIR) spectra were collected by a Bruker IFS 66/S spectrometer equipped with a ZnSe crystal with the beam incident at an angle of 45º. The samples were analyzed over 575–4000 cm^{-1} range with the resolution of 4 cm^{-1}.

2.2.4 Far-IR

Far-IR results have been collected by using Nicolet 6700 FTIR. For measuring the powder samples, it should be prepared as pellet. Pellets were prepared with HDPE (high density polyethylene) as matrix materials, use of HDPE made it possible to work between 70-1200 cm^{-1}. Pellets were prepared with 15 mg sample mixed in 100 mg

HDPE followed by 5 tons of pressure for 5 minutes. The pellet samples were analyzed in the range of 70-700 cm^{-1}. The system is constantly purged with dry air to reduce the water vapor interference in the collected spectra as much as possible. After samples were placed in the Far-IR device, the measurements were taken after 4 hours of waiting for purging purpose.

2.2.5 Scanning Electron Microscope (SEM)

Scanning electron microscope was used to investigate the morphology of the samples. The analyses were completed using Zeiss SUPRA 50 VP with a magnification between 12 to 900000 and variable pressure between 2 to 133Pa, acceleration voltage between 0.1 to 30 kV.

2.2.6 Photoluminescence Reader

Photoluminescence spectra were collected by using Varian Cary Eclipse Fluorescence Spectrometer from 450 to 700 nm of dopants (Dy, Sm, Tb) with 5 nm emission and excitation slits at a rate of 100 nm per/min. Examination of samples was carried out directly in powder samples.

2.3 Experimental Methods

2.3.1 Synthesis of $LnBO_3$

$LnBO_3$ synthesis was carried out with microwave assisted synthesis method with urea. (Merck 99.0 %) (0.415g) and (Ln: La, Gd, Y) powders. The molar ratio was La_2O_3, Y_2O_3, Gd_2O_3: urea =1:1.33. The samples were heated in the microwave at 1200W for 10 minutes. In a ceramic crucible, rare earth oxides, La_2O_3 (Aldrich 99.9 %), Y_2O_3 (Aldrich 99.9 %), Gd_2O_3 (Acros Organics 99.9 %) and H_3BO_3 (Merck 99.5 %) were weighed in stoichiometric amounts and mixed together. The molar ratio was La_2O_3, Y_2O_3, Gd_2O_3: H_3BO_3= 1:2. The mixture was thoroughly grinded approximately for 5 minutes. The samples were incubated in the microwave for 10 minutes. Following

microwave incubation, they were heated in a furnace at 950 °C for 2 hours. Rare earth elements were added to the mixture to form 72 different samples. The ratios were 1.06, 2.12, 3.18, 4.24, 5.30, 5.73, 6.36 %. Tables 4, 5, 6 show the doping amounts by mole percent. The expected reactions are as follows:

$$La_2O_3 + 2H_3BO_3 \xrightarrow{\text{Fuel}} 2LaBO_3 + 3H_2O$$

$$Gd_2O_3 + 2H_3BO_3 \xrightarrow{\text{Fuel}} 2GdBO_3 + 3H_2O$$

$$Y_2O_3 + 2H_3BO_3 \xrightarrow{\text{Fuel}} 2YBO_3 + 3H_2O$$

Table 4: Mol percent of Dy.

Doping Agent	**Percentage of dopant (%)**	**Dy_2O_3 (g)**
Dy	1.06	0.021
Dy	2.12	0.043
Dy	3.18	0.064
Dy	4.24	0.086
Dy	5.30	0.100
Dy	5.73	0.116
Dy	6.36	0.128

Table 5: Mol percent of Sm.

Doping Agent	**Percentage of dopant (%)**	**Sm_2O_3 (g)**
Sm	1.06	0.019
Sm	2.12	0.038
Sm	3.18	0.058
Sm	4.24	0.077
Sm	5.30	0.096
Sm	5.73	0.104
Sm	6.36	0.115

Table 6: Mol percent of Tb.

Doping Agent	Percentage of dopant (%)	Tb_4O_7(g)
Tb	1.06	0.040
Tb	2.12	0.080
Tb	3.18	0.128
Tb	4.24	0.172
Tb	5.30	0.200
Tb	5.73	0.232
Tb	6.36	0.256

Table 7 shows the weight of used materials. Sm, Tb doping percentage and its weight is also calculated using the same formula. The Dy doping percentage was calculated as below formulation 2.1-2.2:

Table 7: Weight of used materials.

Materials	Mol	Weight (g)
Y_2O_3	5.18×10^{-3}	1.17
Gd_2O_3	5.18×10^{-3}	1.88
La_2O_3	5.18×10^{-3}	1.69
H_3BO_3	0.0103	0.64
Urea	6.9×10^{-3}	0.415

Dy_2O_3 (0.021g, 5.36×10^{-5} mol) (2.1)

Doping percentage= $\frac{2Dy}{LaBO3+2Dy}$= 1.06 % (2.2)

3. RESULTS AND DISCUSSION

3.1 X-ray Diffraction Patterns

3.1.1 Undoped and Dy, Sm and Tb doped $LaBO_3$ X-ray Results

The crystal structures of the undoped and Dy, Sm, Tb doped $LaBO_3$ samples were obtained by the powder X ray diffraction (XRD) measurements. The XRD data were recorded using Rigaku X-Ray Diffractometer with CuKα (30kV, 15mA, λ= 1.54 Å). The 2 theta range adopted for the XRD investigations were collected to be 5° and 90°. The scan speed was set to 1 degree per/min.

For the undoped and rare earth elements (REE) doped $LaBO_3$ samples XRD patterns and hkl values obtained from Joint Committee on Powder Diffraction Standards (JCPDS) are shown in **Figure 19**. The value match with JCPDS no:12-0762 card very well. Space group is Pnma and crystal system is orthorhombic with unit cell parameters a=5.84 Å, b=8.18 Å, c=5.07 Å. There are no obvious differences between Dy doped and undoped samples. There are shifts in peak positions that come with doping but these are small enough to be neglected. We can explain the cause of negligible shifting with close radii of RE ions; La^{3+}: 1.045 Å, Gd^{3+}: 0.938 Å, Y^{3+}: 0.900 Å and Dy^{3+}: 0.912 Å, Sm^{3+}: 0.958 Å, Tb^{3+}: 0.923 Å [68]. So, it is concluded that they can make interstitial alloy and/or substitutional alloy with host very well. Consequently, we should also state that the doping amounts are low and disturbances may have not been observed with X-Ray.

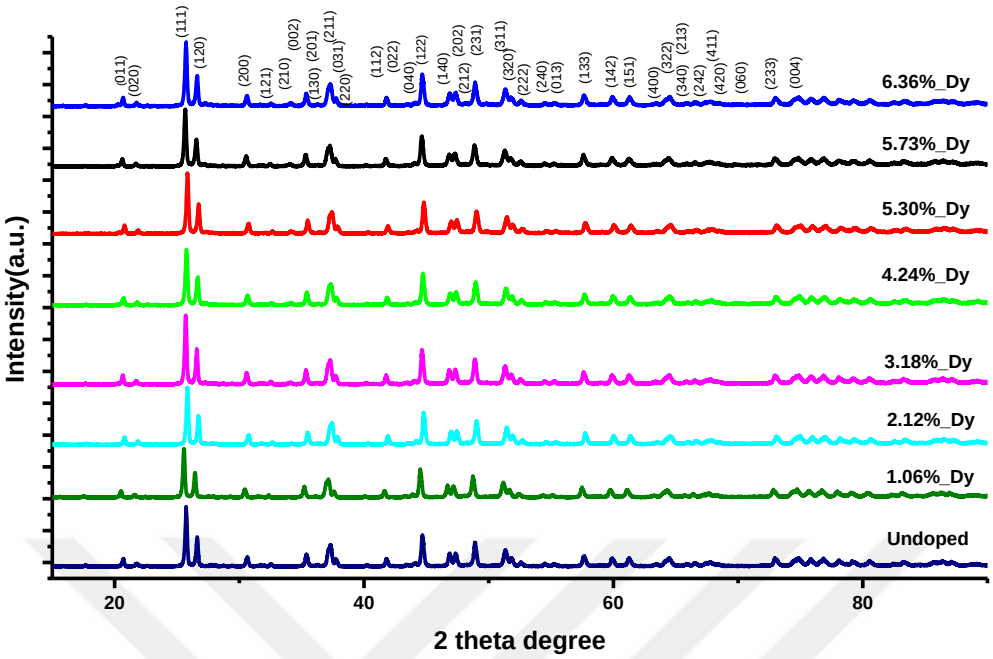


Figure 19. X-Ray patterns of undoped and Dy doped $LaBO_3$ samples.

X ray patterns are shown for undoped and Sm doped samples in **Figure 20** and undoped and Sm doped $LaBO_3$ samples have the same h-k-l values. X ray patterns are shown for undoped and Tb doped samples in **Figure 21** and the h-k-l numbers of Tb, Sm doped samples match with undoped samples h-k-l values and JCPDS no: 12-0762 cards h-k-l values. When these results are considered, it is seen that no different phases occur and all the samples have the same crystal structure. In conclusion, syntheses are done successfully.

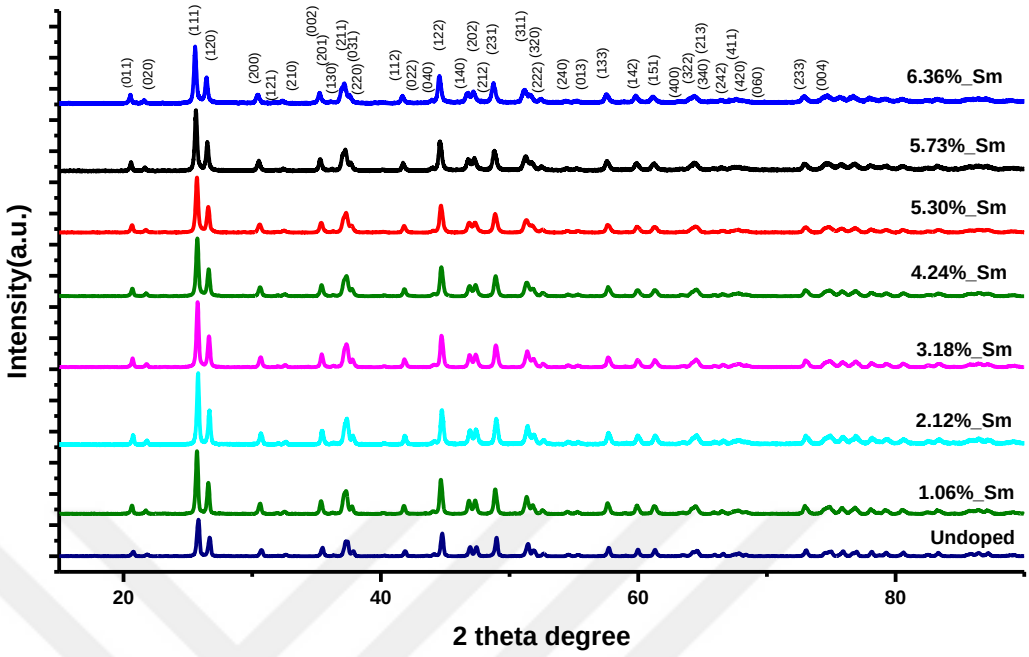


Figure 20. X-Ray patterns of undoped and Sm doped $LaBO_3$ samples.

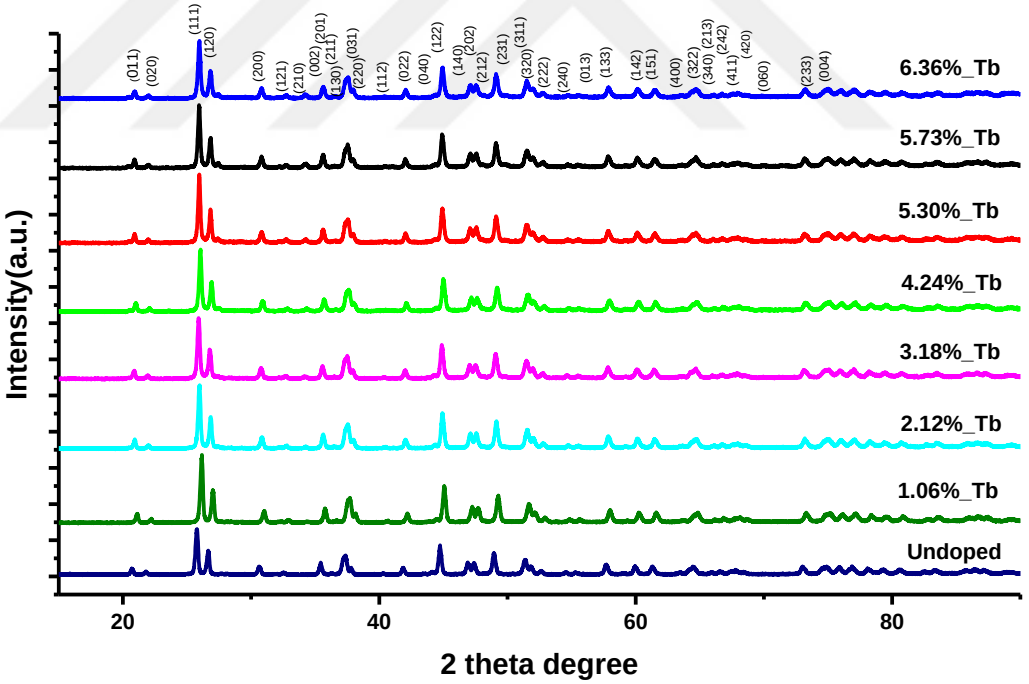


Figure 21. X-Ray patterns of undoped and Tb doped $LaBO_3$ samples.

3.1.2 Undoped and Dy, Sm and Tb doped $GdBO_3$ X-ray Results

Figure 22 shows the XRD patterns of undoped and Dy doped $GdBO_3$ samples. These patterns were used to analyze the crystal structure and phase of all samples. The space group is $R3_2$ and crystal system is rhombohedral. The lattice parameters are a=6.63Å, c=26.72 Å.

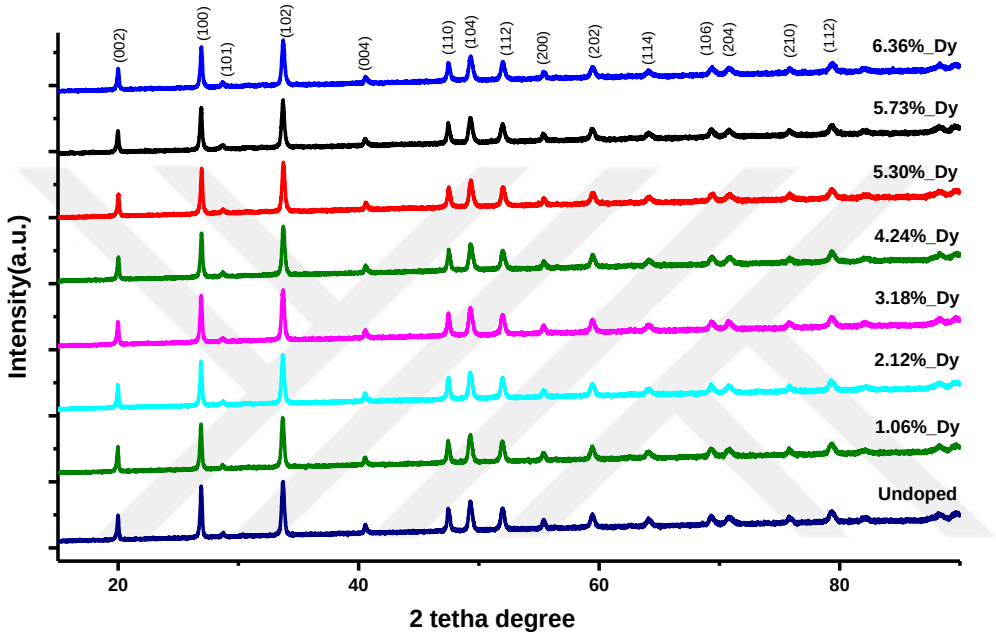


Figure 22. X-Ray patterns of undoped and Dy doped $GdBO_3$ samples.

Figure 23 shows undoped and Sm doped $GdBO_3$ X-ray pattern. The h-k-l values shown in the figure and the h-k-l values on the JCPDS no: 13-0483 card match. Hence, the crystal systems of these samples are rhombohedral with space group $R3_2$ and lattice parameters a=6.63 Å, c=26.72 Å.

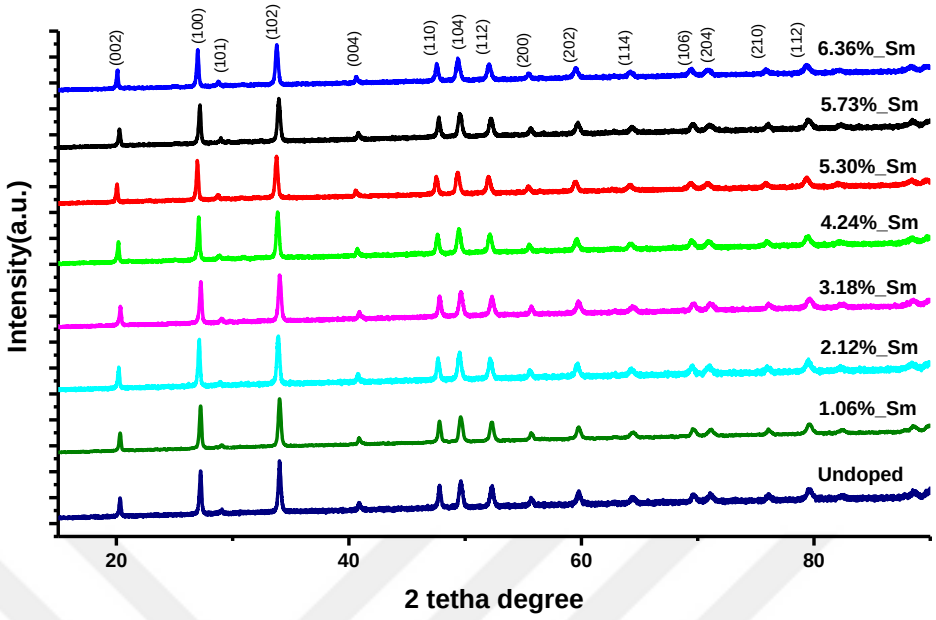


Figure 23. X-Ray patterns of undoped and Sm doped $GdBO_3$ samples.

Figure 24 shows undoped and Tb doped $GdBO_3$ X-ray pattern. The h-k-l values shown in figure and the h-k-l values on the JCPDS no: 13-0483 card match. The peak positions and intensities were compared to those in the Joint Committee on Powder Diffraction Standards (JCPDS) data files. Only hexagonal phase of the gadolinium borate was identified. The positions of the peaks correspond accurately to the Standard card with number 13-0483.

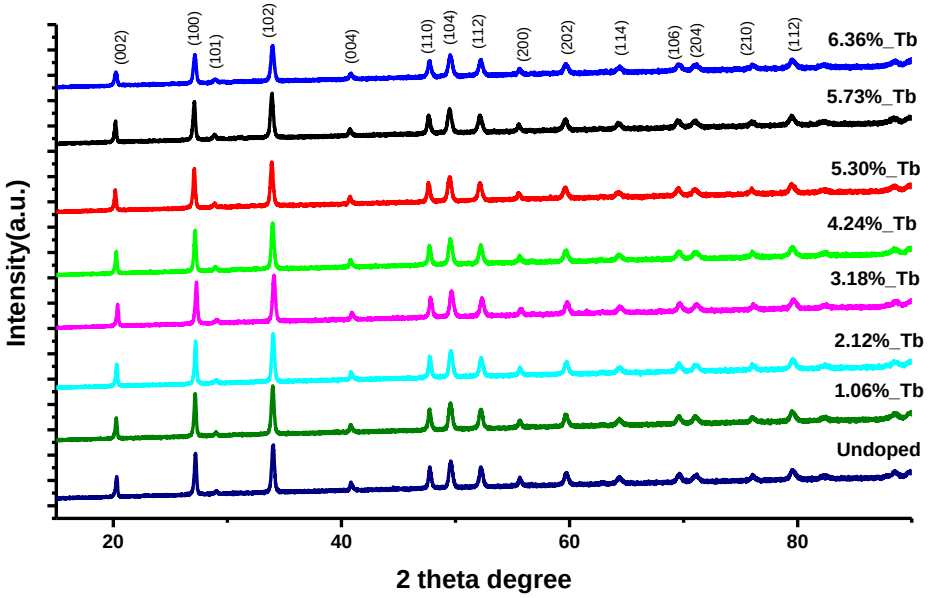


Figure 24. X-Ray patterns of undoped and Tb doped $GdBO_3$ samples.

3.1.3 Undoped and Dy, Sm and Tb doped YBO_3 X-ray Results

Figure 25 shows undoped and Dy doped YBO_3 X-ray pattern. Looking at this pattern, it is concluded that there are no differences in the peaks of Dy doped and undoped samples. This shows that there are no impurities or different phases in samples. The h-k-l values of JCPDS no :88-0356 card and the h-k-l values of samples match.

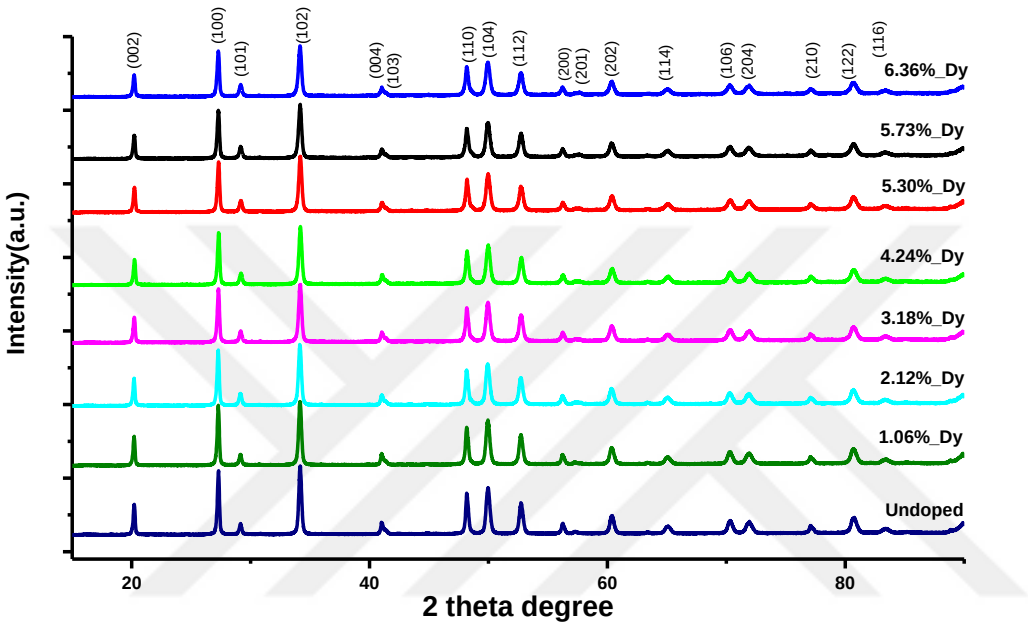


Figure 25. X-Ray patterns of undoped and Dy doped YBO_3 samples.

Figure 26 shows Sm doped and undoped YBO_3 sample patterns. No differences are evident in the patterns. **Figure 27** shows patterns of Tb doped and undoped samples. No differences in the patterns of samples are noticed. Thus, considering the patterns of all samples, only the cubic phase of the yttrium borate was identified by comparing the peak positions and the intensities with those in the Joint Committee on Powder Diffraction Standards (JCPDS) data files. The positions of the peaks correspond accurately to the Standard card with number 88-0356. All samples have a space group of C2/c and a monoclinic crystal structure. The lattice parameters of this structure are: a=11.32 Å, b=6.54 Å, c=9.55 Å, β=112.955°.

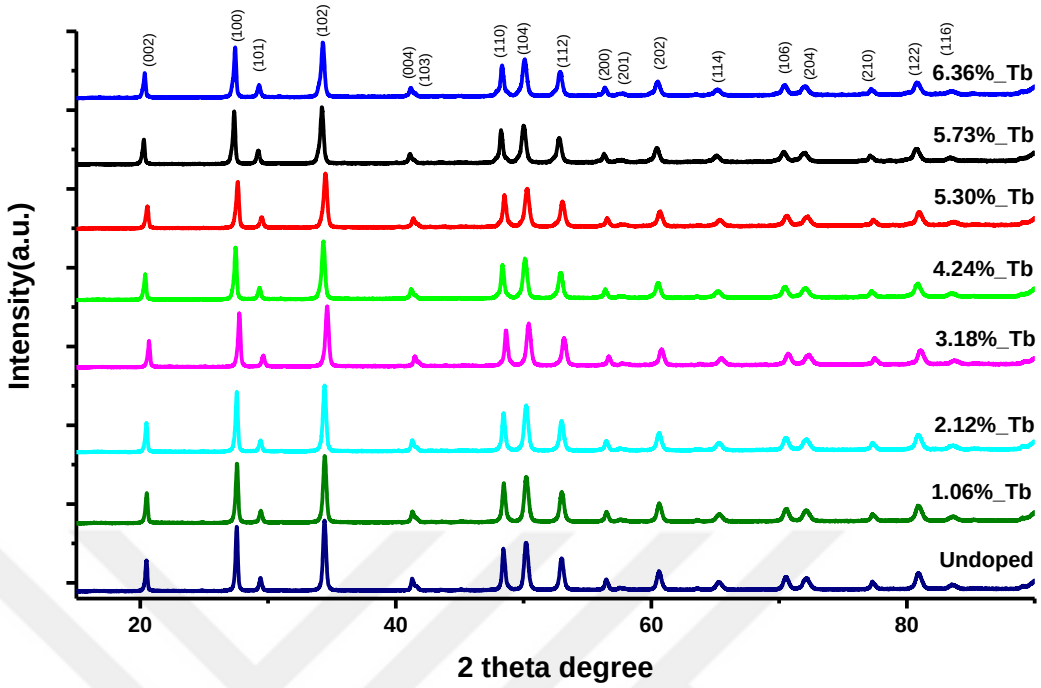


Figure 26. X-Ray patterns of undoped and Sm doped YBO_3 samples.

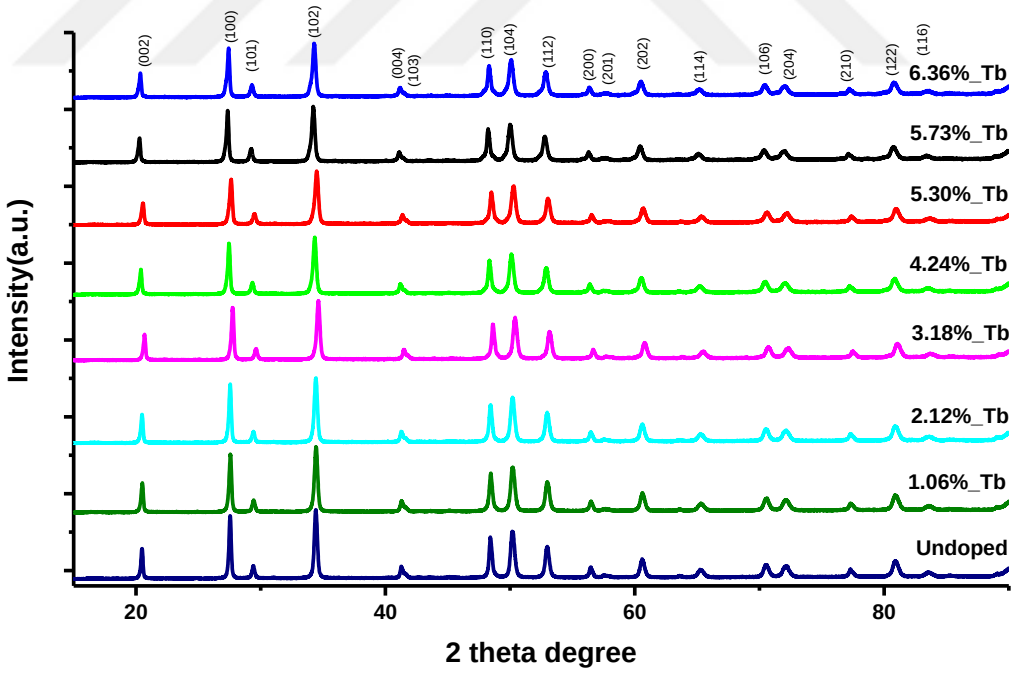


Figure 27. X-Ray patterns of undoped and Tb doped YBO_3 samples.

3.2 SEM & EDX Results

3.2.1 Undoped and Dy, Sm, Tb doped $LaBO_3$ SEM&EDX Results

In **Figure 28** SEM image of undoped $LaBO_3$ and Dy, Sm, Tb doped $LaBO_3$ powders shows a fine size and regular morphology. Also, doping amount of Dy, Sm, Tb does not affect the crystallinity and morphology of $LaBO_3$. In addition, we observed that Dy, Sm and Tb doped $LaBO_3$ sample sizes are roughly same as undoped $LaBO_3$ the samples size.

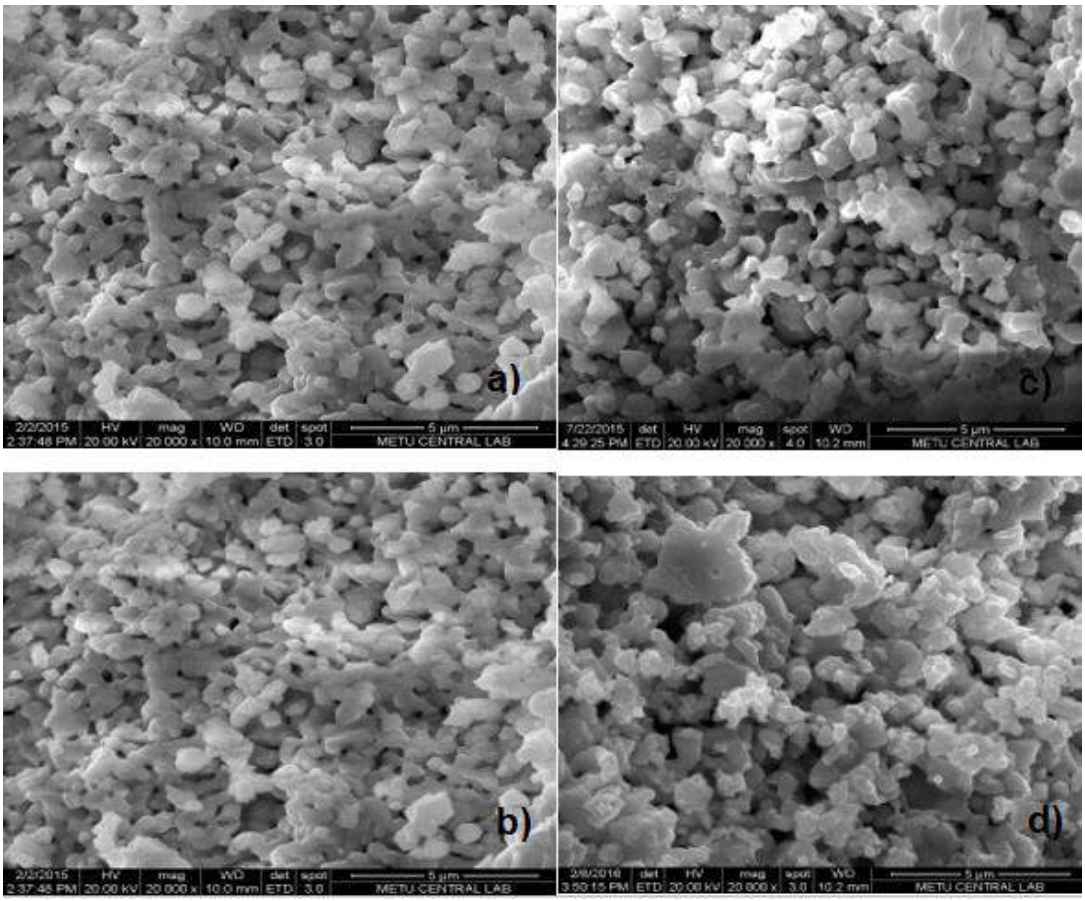


Figure 28. SEM images of a) undoped $LaBO_3$ b) Dy doped $LaBO_3$ c) Sm doped $LaBO_3$ d) Tb doped $LaBO_3$ all scale of 5 μm.

Figure 29 demonstrates the EDX (Energy Dispersive X-ray) results for the Dy, Sm and Tb doped $LaBO_3$ and undoped $LaBO_3$ by urea precursors. Boron has poorer detection limit; hence, boron is not identified precisely. Thus, a clean and truthful ratio of the elements cannot be given. Comparing undoped and REE doped $LaBO_3$ samples,

it is proven that REE is existed in the sample synthesized by all three different doping agents.

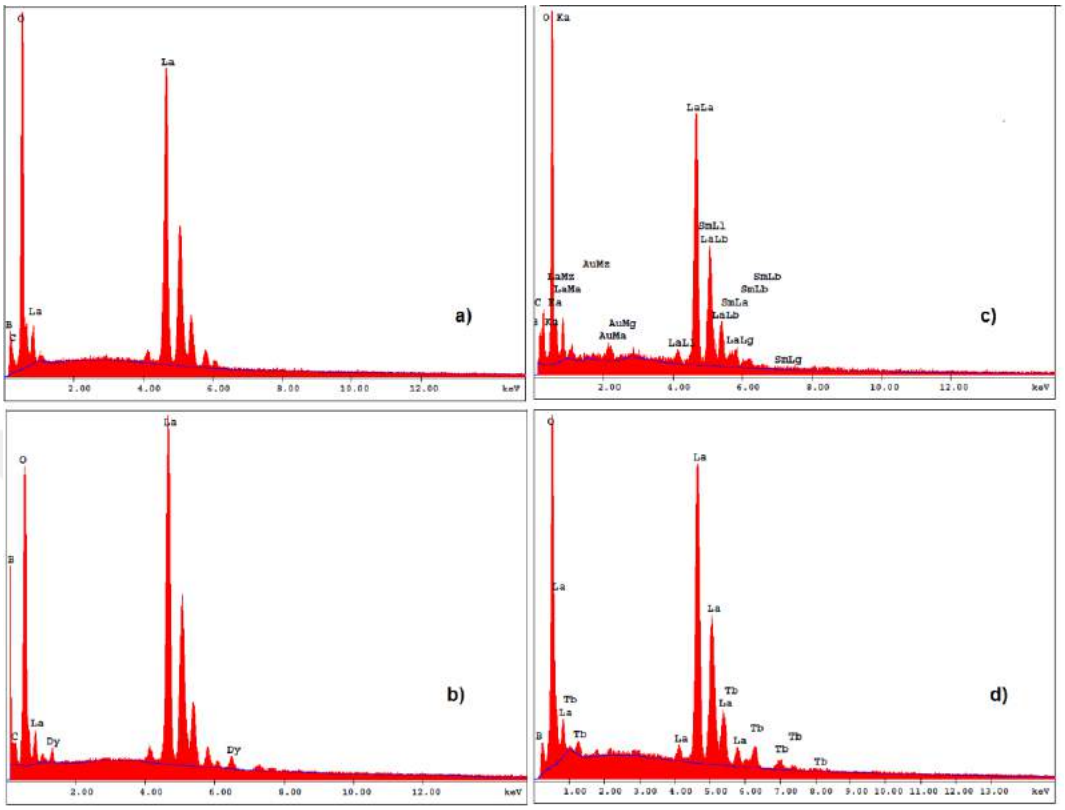


Figure 29. EDX results a) undoped $LaBO_3$b) Dy doped $LaBO_3$ c) Sm doped $LaBO_3$ d) Tb doped $LaBO_3$.

3.2.2 Undoped and Dy, Sm, Tb doped $GdBO_3$ SEM&EDX Results

In **Figure 30** SEM image of Dy, Sm, Tb doped $GdBO_3$ and undoped $GdBO_3$ powders show a fine size and regular morphology. Also, different doping amount of Dy, Sm, Tb does not affect the crystallinity and morphology of $GdBO_3$. Moreover, we detected that Dy, Sm and Tb doped $GdBO_3$ samples sizes are roughly same as undoped $GdBO_3$ samples size.

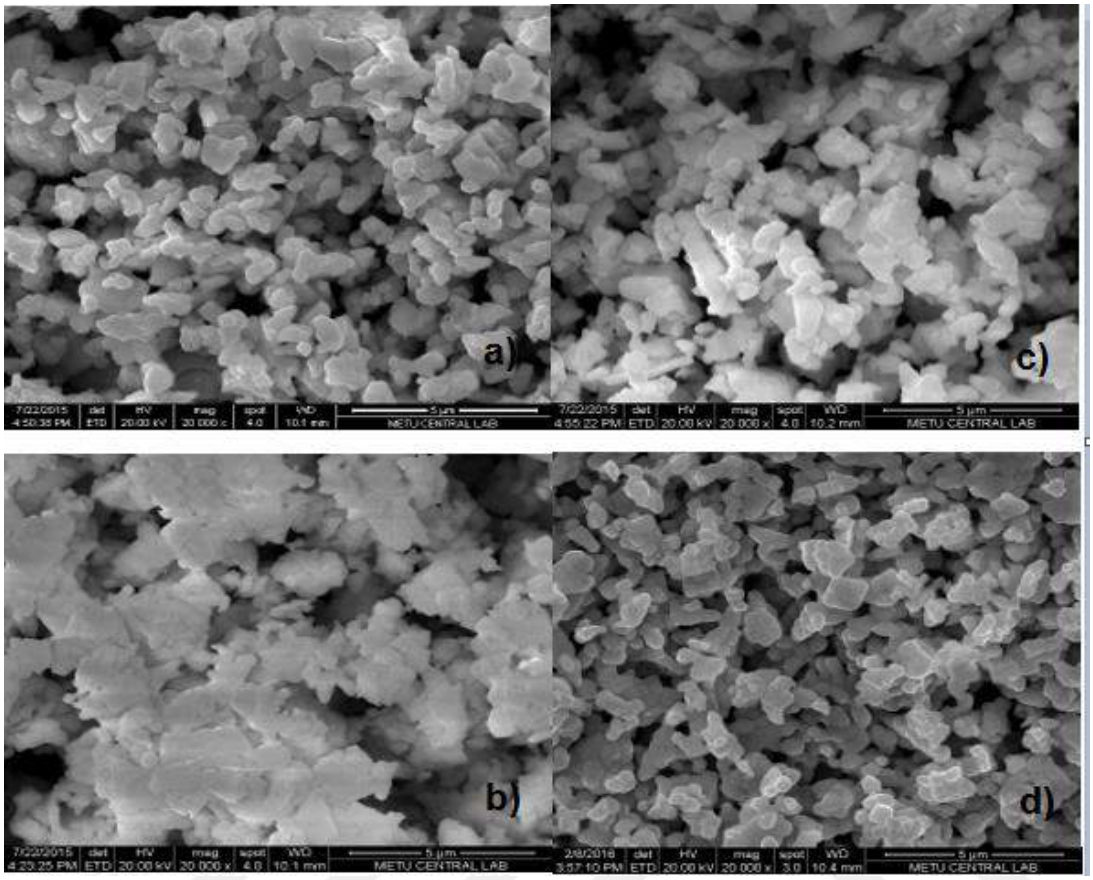


Figure 30. SEM images of a) undoped $GdBO_3$ b) Dy doped $GdBO_3$ c) Sm doped $GdBO_3$ d) Tb doped $GdBO_3$ all scale of 5 μm.

Figure 31 reveals the EDX results for the undoped $GdBO_3$ and Dy, Sm and Tb doped $GdBO_3$. When undoped $GdBO_3$ sample result and REE doped $GdBO_3$ samples results are compared, it is proven that REE is existed in the sample synthesized by all three different doping agents.

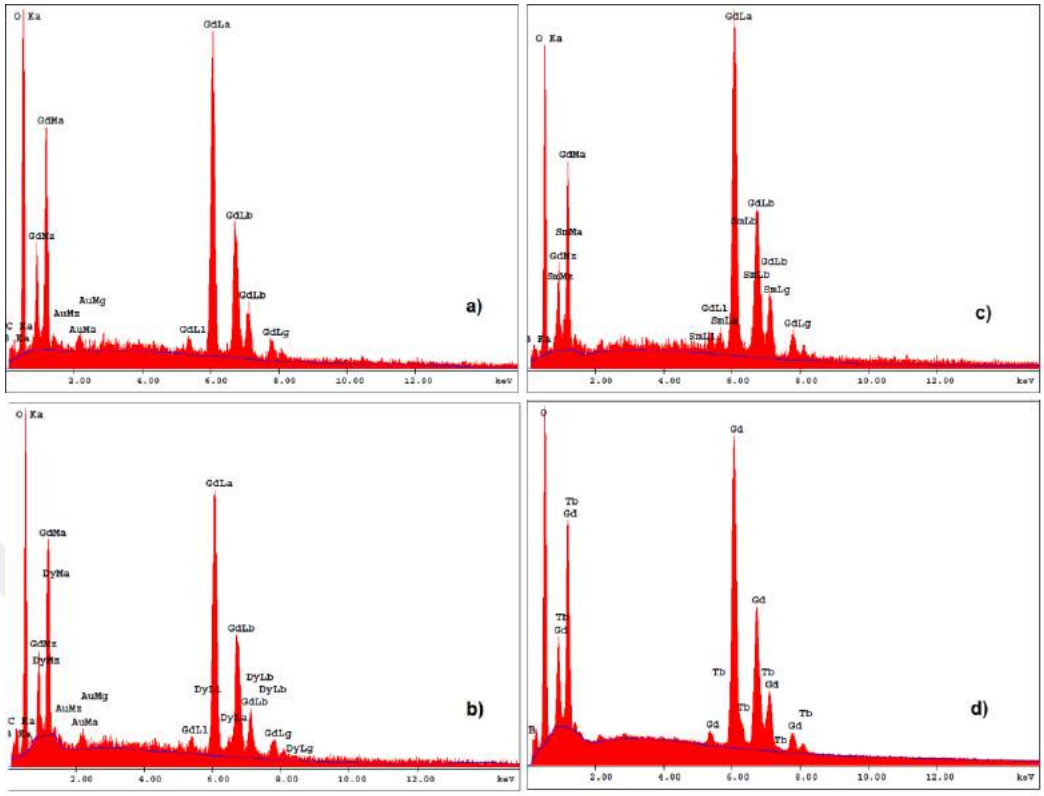


Figure 31. EDX results of a) undoped $GdBO_3$b) Dy doped $GdBO_3$ c) Sm doped $GdBO_3$ d) Tb doped $GdBO_3$.

3.2.3 Undoped and Dy, Sm, Tb doped YBO_3 SEM&EDX Results

Dy, Sm, Tb doped YBO_3 and undoped YBO_3 powders have a fine size and regular morphology, **Figure 32** shows all samples SEM images. Similarly, altered fraction doping amount of Dy, Sm, Tb does not affect the crystallinity and morphology of YBO_3. Additionally, we detected that the sizes of Dy, Sm and Tb doped YBO_3 samples are roughly same as the size of undoped YBO_3 sample.

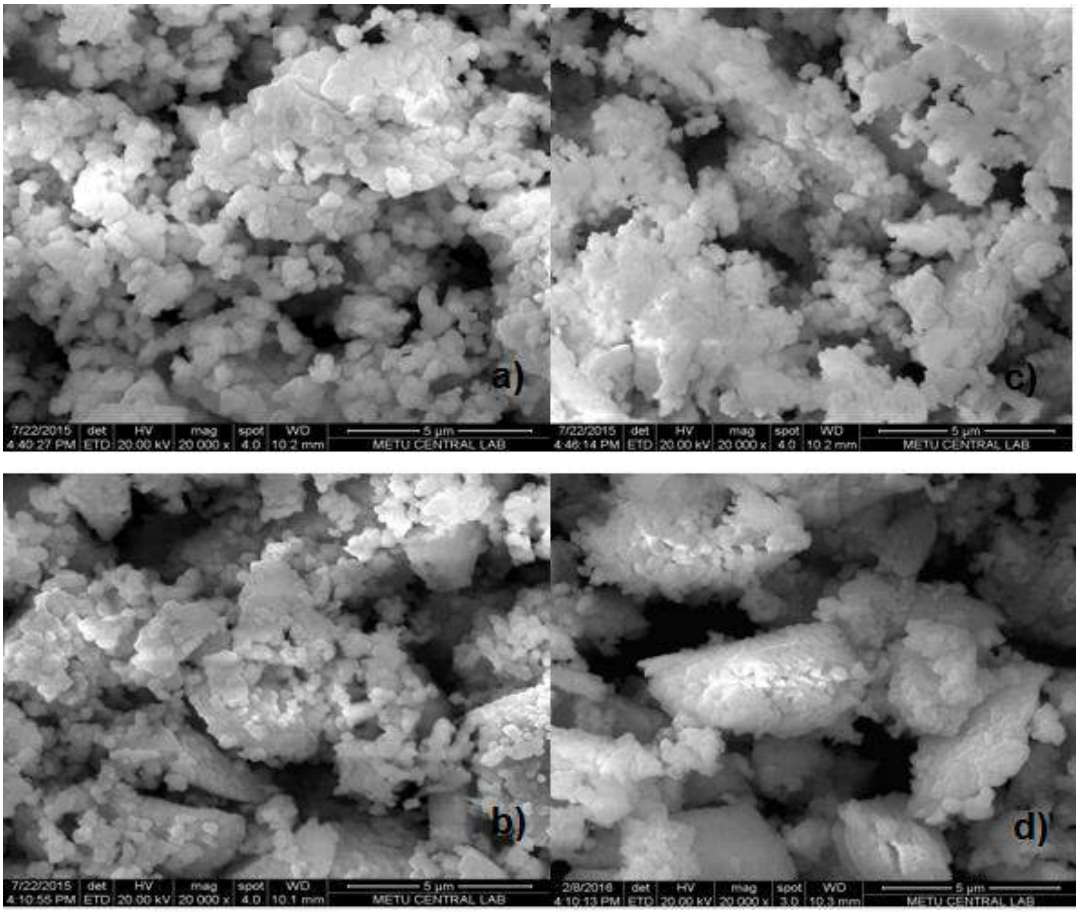


Figure 32. SEM images of a) undoped YBO_3 b) Dy doped YBO_3 c) Sm doped YBO_3 d) Tb doped YBO_3 all scale of 5 µm.

Figure 33 demonstrates that undoped YBO_3 and REE doped YBO_3 samples EDX results. We observed that REE exist in the REE doped YBO_3 samples from these results.

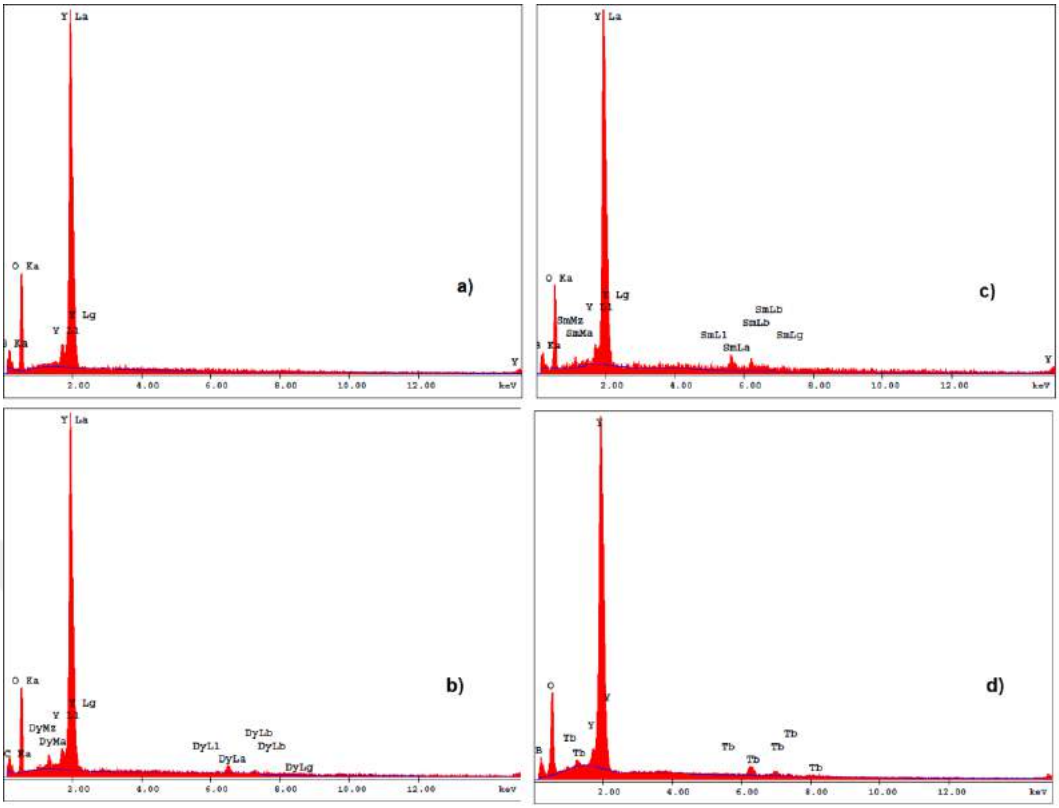


Figure 33. EDX results of a) undoped YBO_3 b) Dy doped YBO_3 c) Sm doped YBO_3 d) Tb doped YBO_3.

3.3 ATR Results and Spectra

3.3.1 Undoped and Dy, Sm and Tb doped $LaBO_3$ ATR Results

Figure 34 Demonstrates the ATR spectra of undoped and Dy doped $LaBO_3$ samples. No significant differences were observed with doping and dopant amount. The ν3 (asymmetric stretching) bands are observed at 1255 cm^{-1} and ν1 (symmetric stretching) bands at 940 cm^{-1}, ν2 (out of plane bending) modes at 790, 708 cm^{-1}, ν4 (in-plane bending) mode at 611, 591 cm^{-1}. All modes belong to planar BO_3^{3-} borate units.

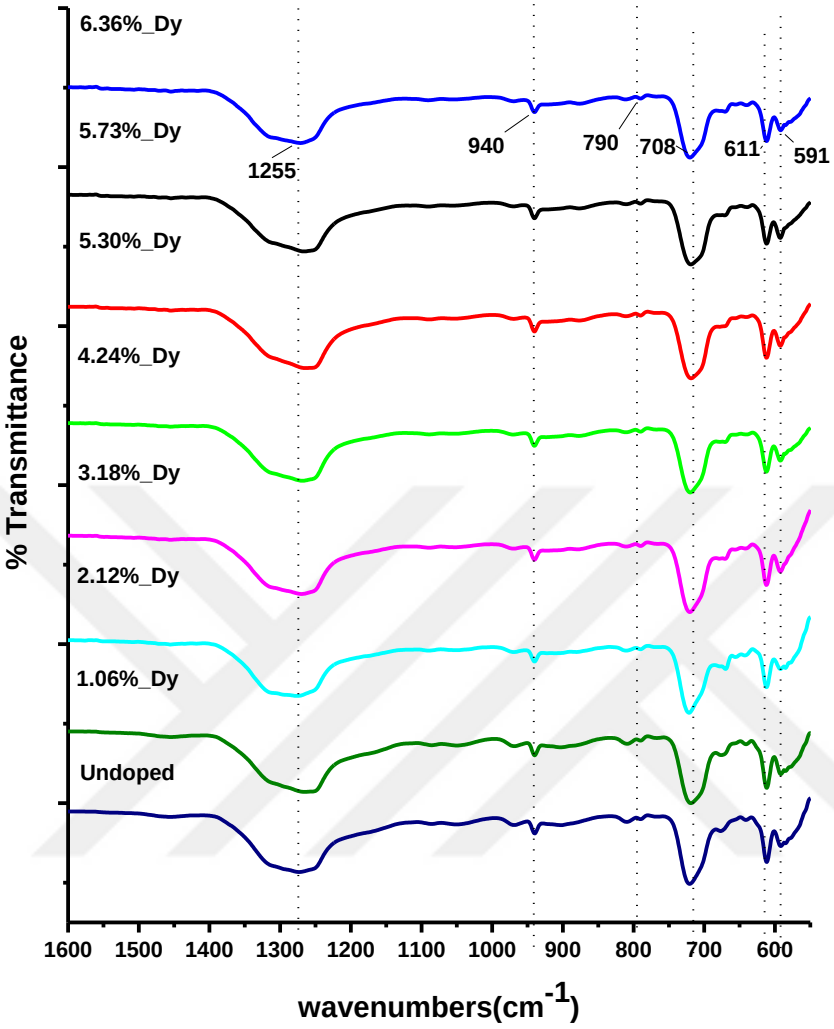


Figure 34. ATR spectra of undoped and Dy doped $LaBO_3$ samples.

Figure 35 showing undoped and Sm doped $LaBO_3$ samples ATR spectra. No significant differences we observed. The ν3 (asymmetric stretching) bands are observed at 1255 cm^{-1} and ν1 (symmetric stretching) bands at 940 cm^{-1}, ν2 (out of plane bending) modes at 790, 708 cm^{-1}, ν4 (in-plane bending) mode at 612 and 591 cm^{-1}. All modes belong to planar BO_3^{3-} borate units.

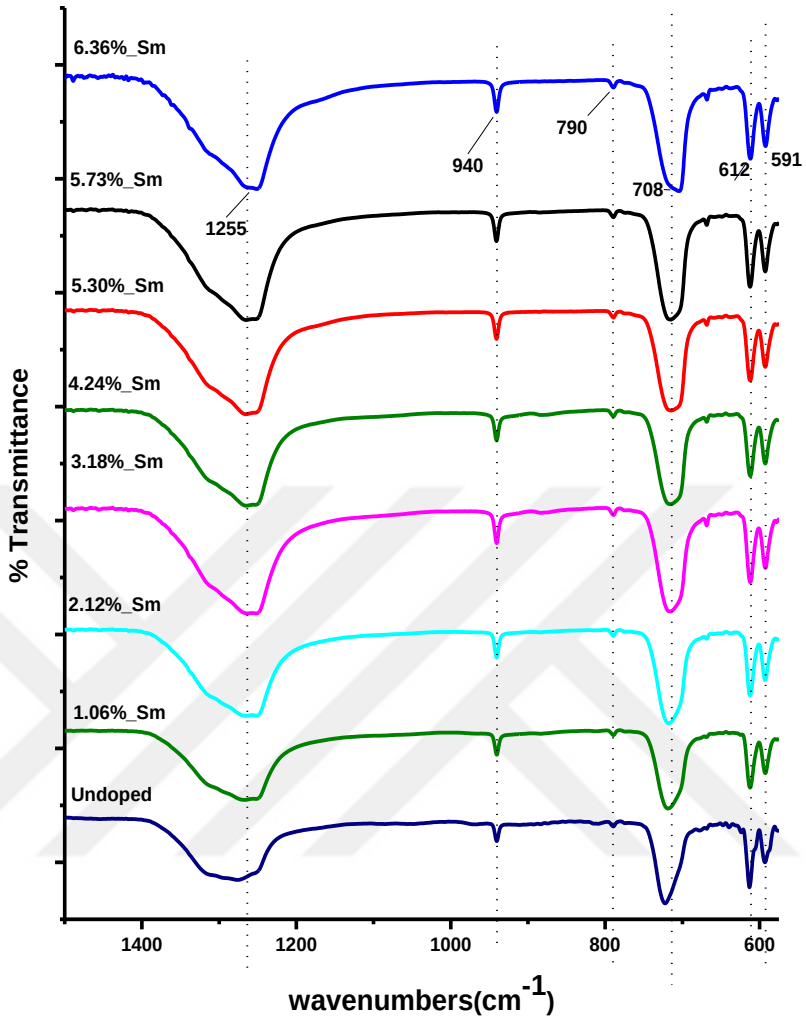


Figure 35. ATR spectra of undoped and Sm doped $LaBO_3$ samples.

When we look at the **Figure 36**, we can see undoped and Tb doped $LaBO_3$ samples have similar spectra. The ν3 (asymmetric stretching) bands are observed at 1255 cm^{-1} and ν1 (symmetric stretching) bands at 940 cm^{-1}, ν2 (out of plane bending) modes at 790, 708 cm^{-1}, ν4 (in-plane bending) mode at 611, 591 cm^{-1}. All modes belong to planar BO_3^{3-} borate units.

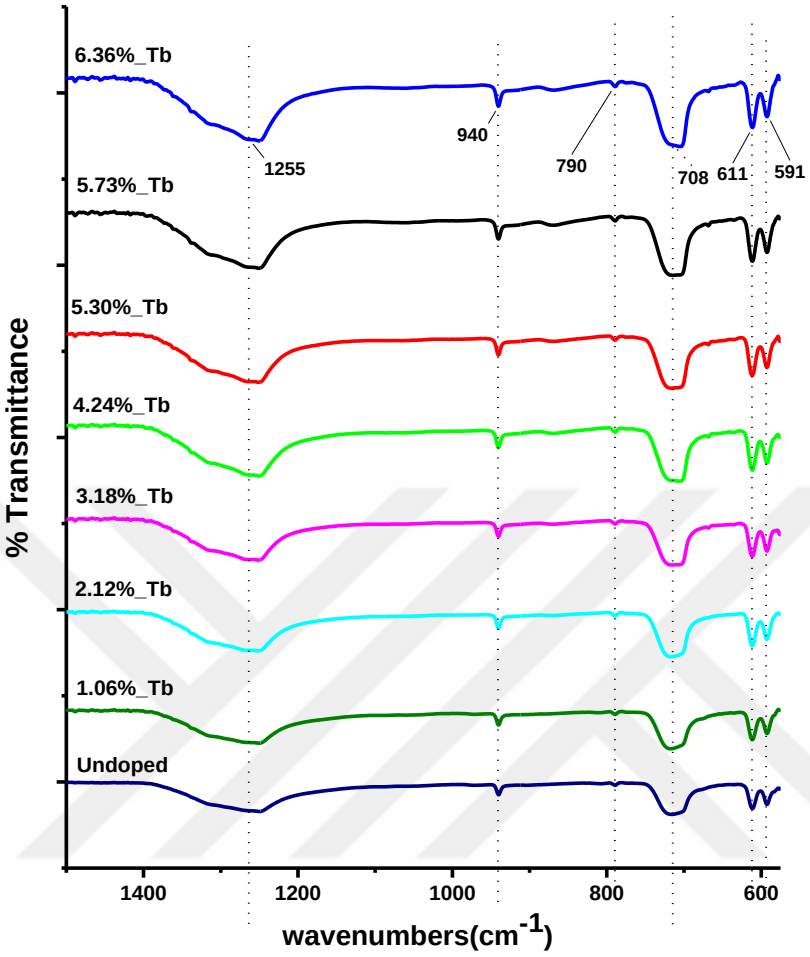


Figure 36. ATR spectra of undoped and Tb doped $LaBO_3$ samples.

Aragonite type of orthoborate $LaBO_3$ has trigonal BO_3^{3-} borate units. Dy, Sm, Tb doped and undoped $LaBO_3$ samples' ATR spectra illustrate that in all samples boron atoms are in three-fold coordination. We can conclude that Dy, Sm, Tb doped samples were synthesized successfully and we did not observe extra bands from the ATR spectra; therefore, we can say that none of the doped samples have create any impurities. Previous study and literature support our results [69].

3.3.2 Undoped and Dy, Sm and Tb doped $GdBO_3$ ATR Results

Undoped and Dy doped $GdBO_3$ samples' spectra demonstrate that different percentage Dy doped samples absorption peaks match with undoped $GdBO_3$ absorption peaks.

Vaterite type of $GdBO_3$ has absorption bands reported as: distortion at frequencies 576 and 698 cm^{-1} and stretching frequencies at 862, 922, 1082 cm^{-1} [70]. The close likenesses in ATR spectra of Dy doped and undoped $GdBO_3$ are marked as in **Figure 37**. The distortion frequencies are 578 and 696 cm^{-1} and stretching frequencies are 821, 904, 980, 1054 cm^{-1}. The slight variation in the peak positions may be due to the broadness of the observed bands.

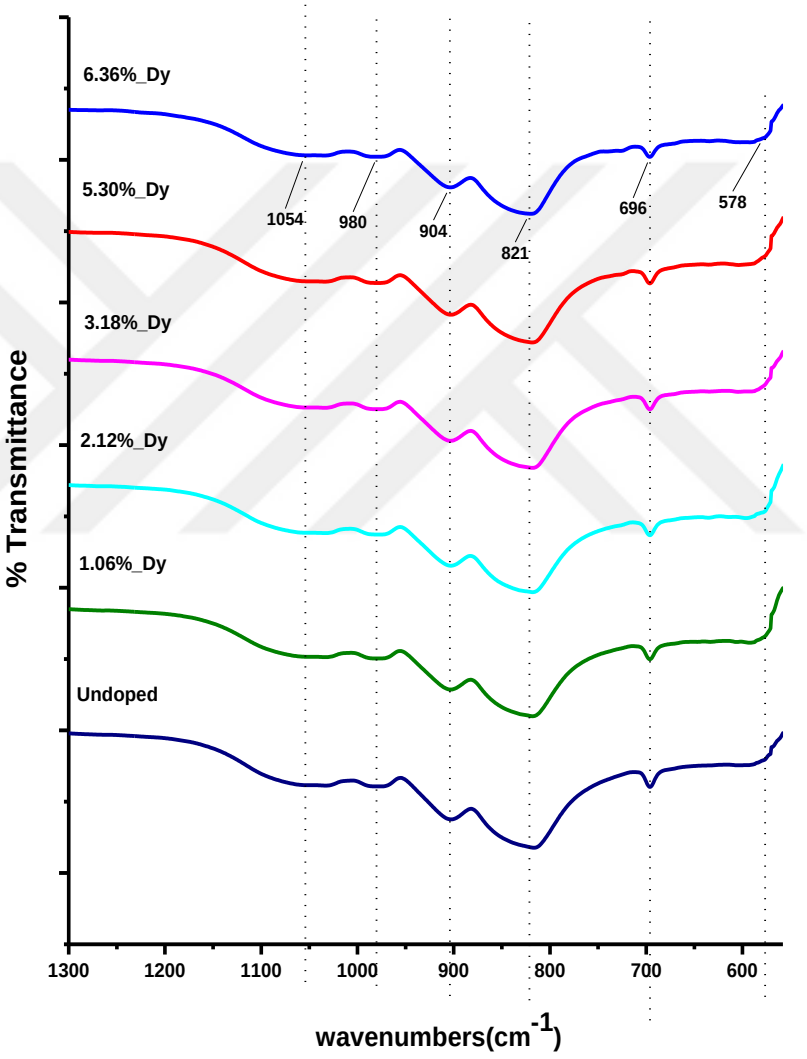


Figure 37. ATR spectra of undoped and Dy doped $GdBO_3$ samples.

Figure 38 shows undoped and Sm doped $GdBO_3$ samples ATR spectra. No significant differences are observed between undoped and doped samples. Distortion frequencies

are observed at 564 and 696 cm^{-1} and stretching frequencies are observed at 827, 908, 976 and 1057 cm^{-1}.

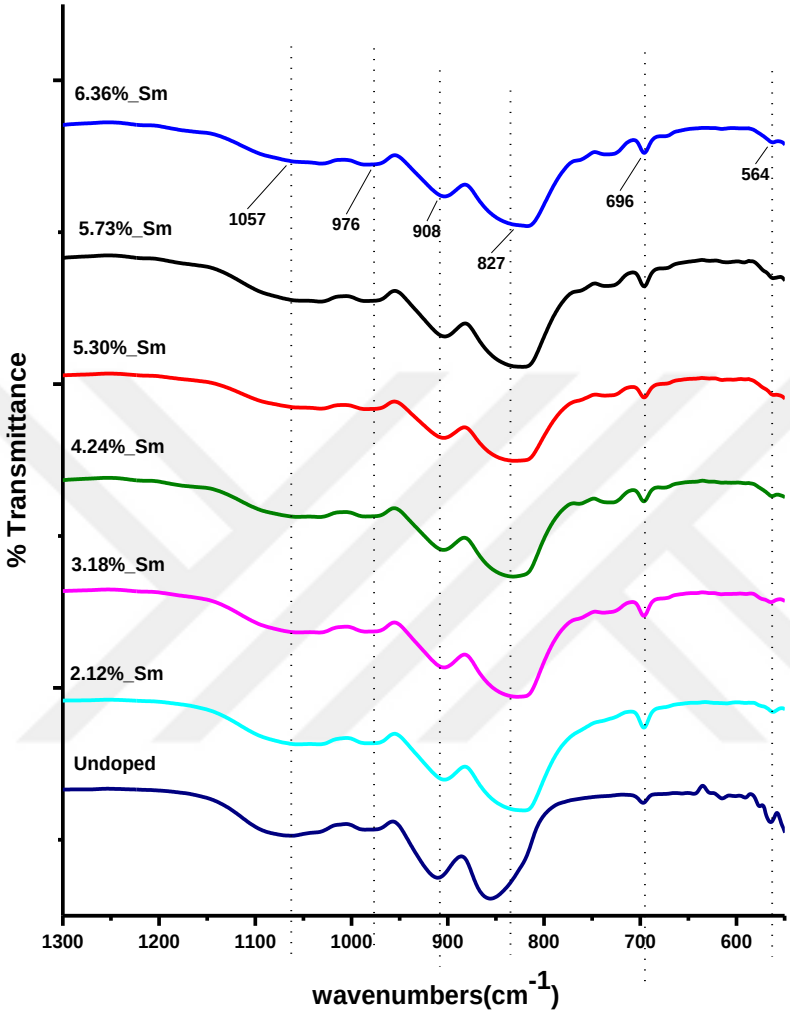


Figure 38. ATR spectra of undoped and Sm doped $GdBO_3$ samples.

Lastly, ATR spectra of undoped and Tb doped $GdBO_3$ samples are present in **Figure 39**. Different amount of Tb doped $GdBO_3$ samples and undoped $GdBO_3$ sample have very similar spectra. No significant differences are obtained with doping Tb ion into the $GdBO_3$. In addition, increase in the dopant amount had no effect. The bending frequencies are observed at 566 and 697 cm^{-1} and stretching frequencies are observed at 824, 908, 979 and 1059 cm^{-1}.

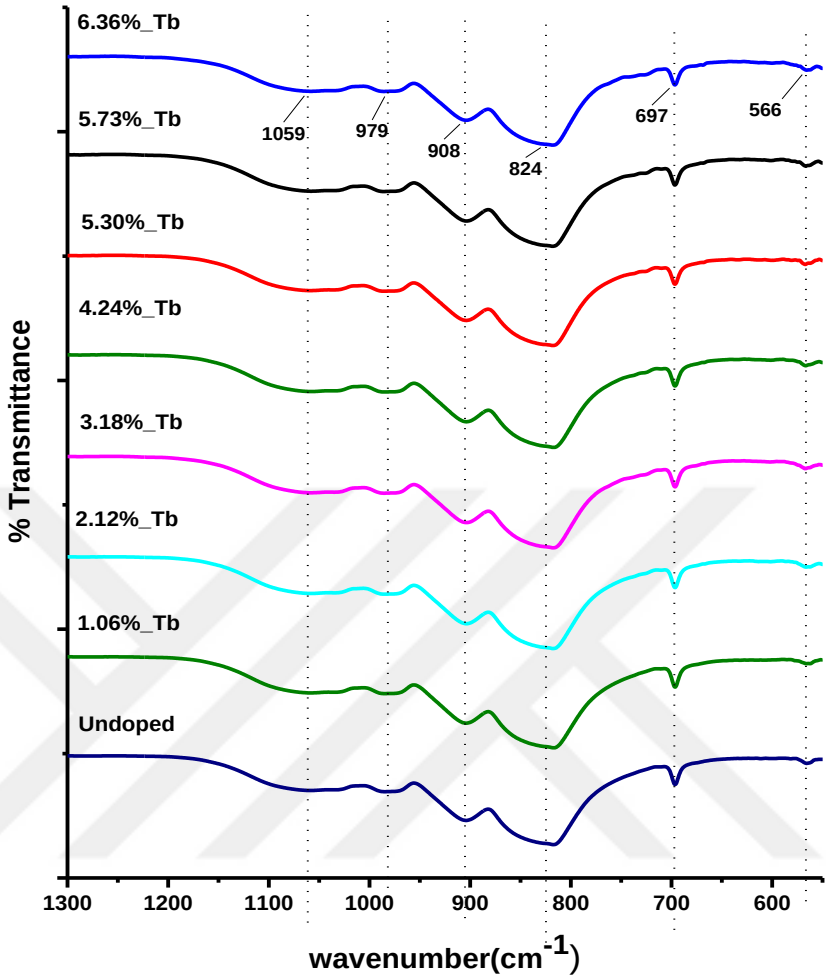


Figure 39. ATR spectra of undoped and Tb doped $GdBO_3$ samples.

The vaterite type of $GdBO_3$ contains only the tetrahedral group of $B_3O_9^{9-}$ borate units. No significant change in the spectra with the dopant type or amount, suggests this tetrahedral structure is not disturbed. We can say that all $GdBO_3$ samples were produced successfully. In addition, we didn't detect any extra peaks in the ATR spectra. Former studies and literature support our observations.

3.3.3 Undoped and Dy, Sm, Tb doped YBO_3 ATR Results

Undoped and Dy dopedYBO_3 samples spectra showed that Dy doped samples with various concentrations and undoped samples have similar structure. The bands of vaterite type of YBO_3 are reported in the literature as follows: distortion frequencies

at 551 and 714 cm^{-1} and stretching frequencies at 874, 935 and 1105 cm^{-1} [70]. In our study, the distortion frequencies are at 576 and 710 cm^{-1} and stretching frequencies are at 829, 906, 1005 and 1077 cm^{-1} in the **Figure 40**.

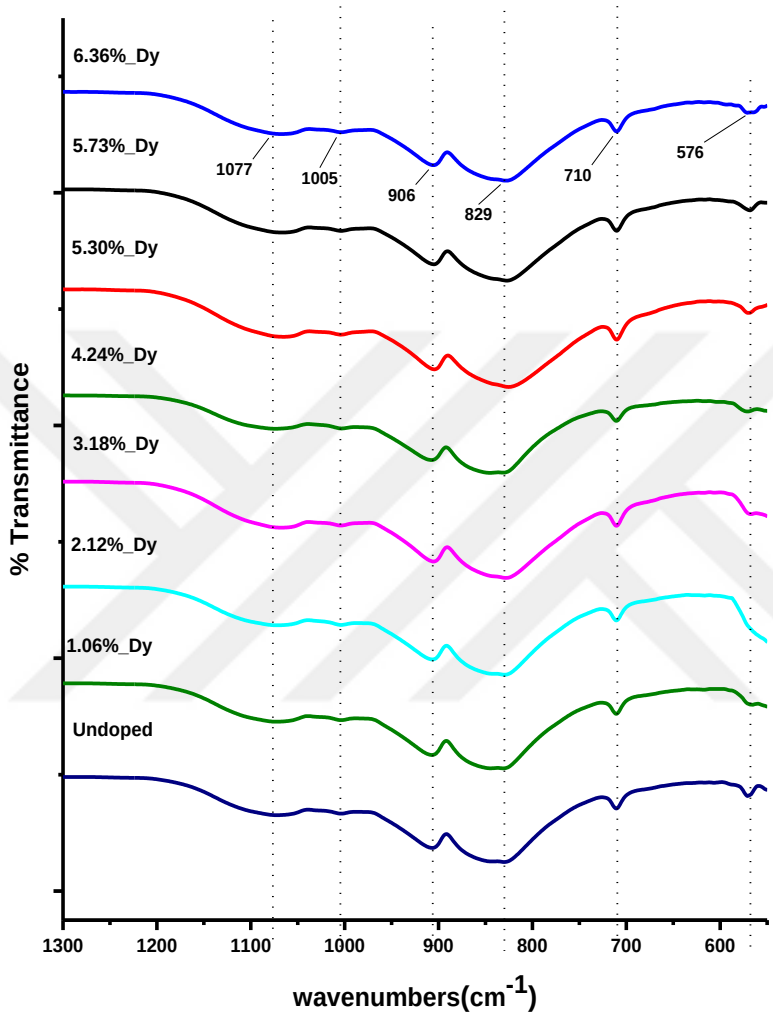


Figure 40. ATR spectra of undoped and Dy doped YBO_3 samples.

Figure 41 presents undoped and Sm doped YBO_3 samples ATR spectra. Likewise, we can detect that altered percentage samples YBO_3 spectra are similar to undoped YBO_3 spectrum. These spectra distortion frequencies are observed at 570 and 710 cm^{-1} and stretching frequencies are observed at 840, 909, 1001 and 1079 cm^{-1}.

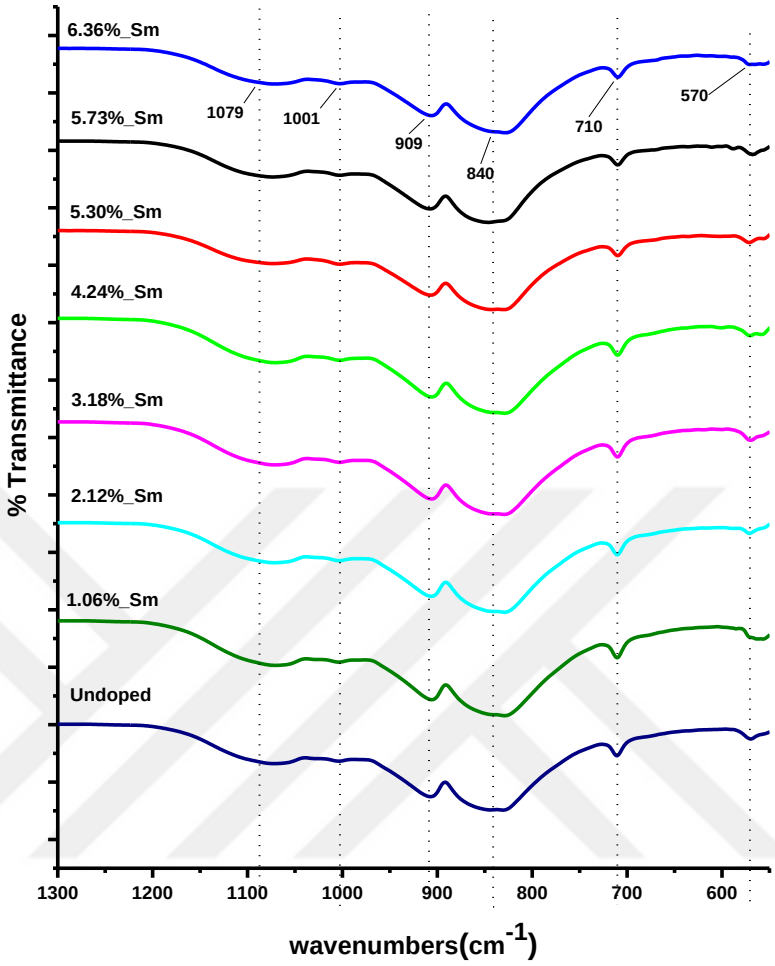


Figure 41. ATR spectra of undoped and Sm doped YBO_3 samples.

We have also not observed any significant alterations as YBO_3 is doped with various amounts of Tb in the **Figure 42**. Altered amount Tb doped YBO_3 samples spectra and undoped YBO_3 sample have similar vibrational modes. In this case, the bending frequencies observed at 568 and 711 cm^{-1} and stretching frequencies observed at 839, 910, 1001 at 1077 cm^{-1}.

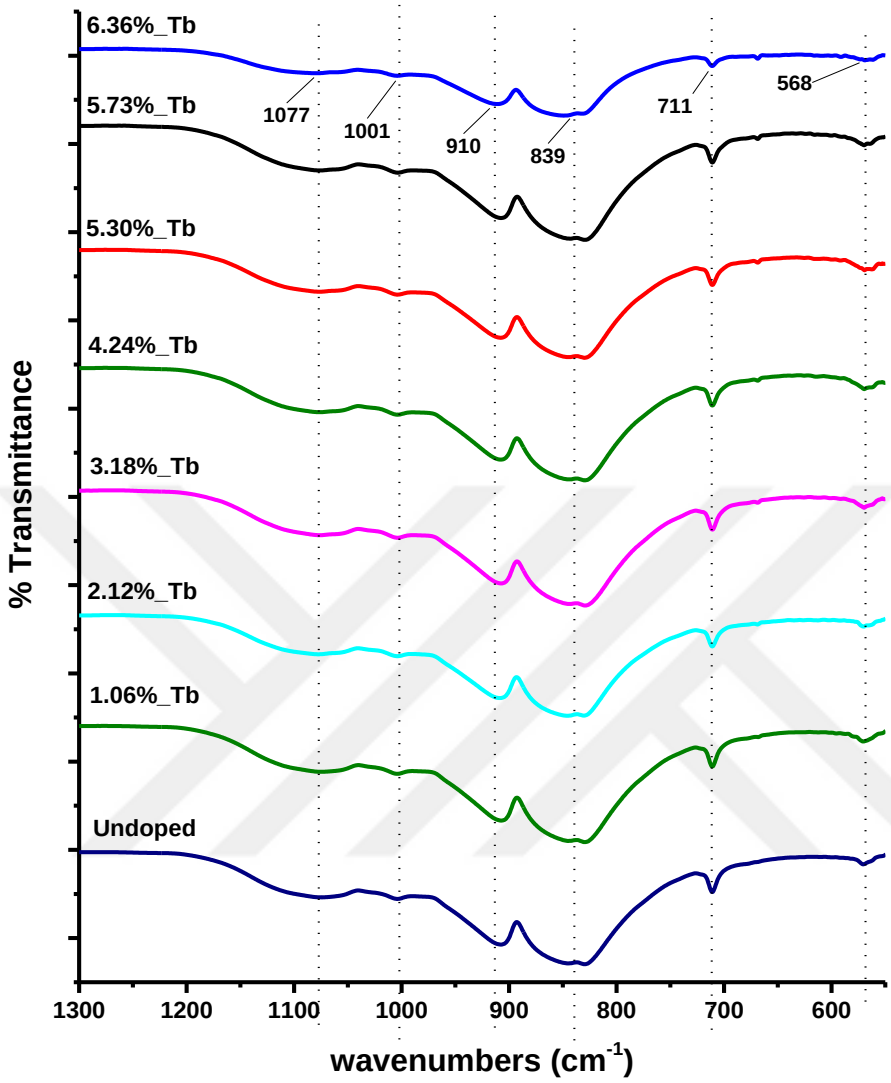


Figure 42. ATR spectra of undoped and Tb doped YBO_3 samples.

The vaterite type of YBO_3 contains only the tetrahedral group of $B_3O_9^{9-}$ borate units. Since no change is observed with doping Dy, Sm, Tb doped YBO_3 have tetrahedral $B_3O_9^{9-}$ anions. We can say that all YBO_3 samples were produced successfully. In addition, we didn't detect any extra peaks from the ATR spectra. Suggesting that there is no impurity in the samples.

3.4 Luminescence Results and Spectra

3.4.1 Dy, Sm, Tb doped $LaBO_3$ Luminescence Results

Figure 43 demonstrates the emission spectra of the $LaBO_3$ samples with different percentage of Dy doping amounts. The $LaBO_3$ is doped with Dy at 1.06, 2.12, 3.18, 4.24, 5.30, 5.73, 6.36 % Dy mole ratio. Emission spectra of Dy^{3+} doped $LaBO_3$ were collected at 351 nm excitation. At this excitation wavelength, we observed three major peaks. The observed three peaks correspond to fluorescence emissions from Dy states where the transitions are marked on the Figure 43. These peaks are at 481, 575 and 665 nm which are identified as to $^4F_{9/2} \rightarrow {}^6H_{15/2}$, $^4F_{9/2} \rightarrow {}^6H_{13/2}$ and $^4F_{9/2} \rightarrow {}^6H_{11/2}$ transitions from the energy levels reported in literature and the strongest transition $^4F_{9/2} \rightarrow {}^6H_{13/2}$ at 575 nm [37]. It is found that the luminescence intensity depends on the doping amount strongly. However, we have not observed any trend with dopant amount. Sample with 5.30 % mole of REE doping has the strongest emission while 6.36 % mole of Dy doping sample intensity is significantly lower than 5.30 % sample because of concentration quenching.

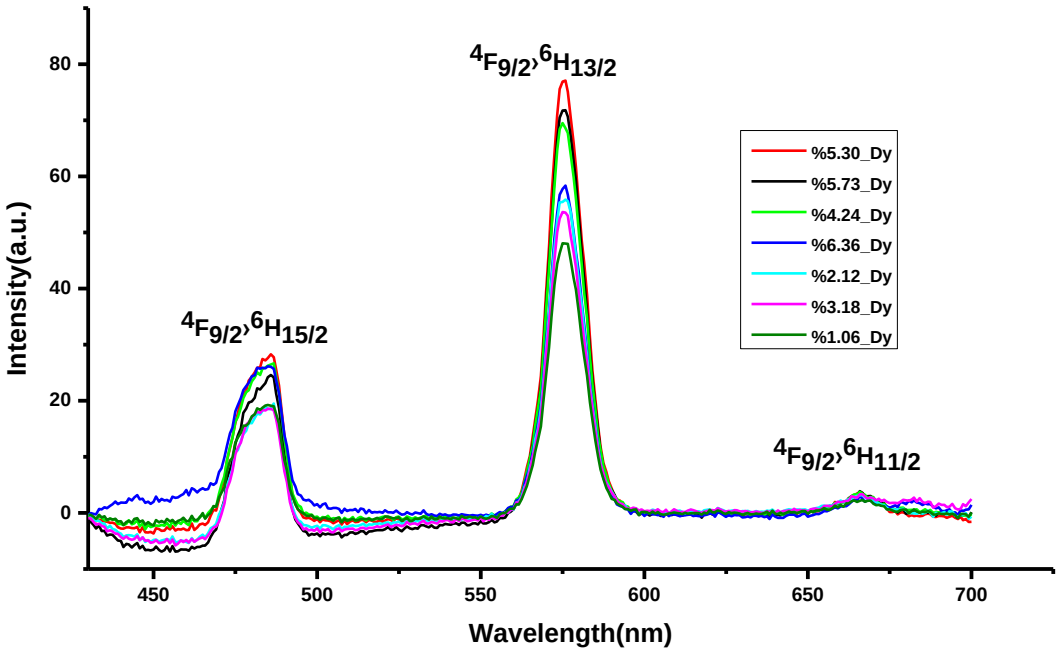


Figure 43. PL spectra of Dy doped $LaBO_3$ samples.

The detected three peaks correspond to luminescence spectra from Sm states where the transitions are marked on the **Figure 44**. These three emission peaks are in between 430-700 nm when excited at 403 nm. These bands at 564, 601, 645 nm which are assigned to $^4G_{5/2} \rightarrow {}^6H_{5/2}$, $^4G_{5/2} \rightarrow {}^6H_{7/2}$ and $^4G_{5/2} \rightarrow {}^6H_{9/2}$ transitions, respectively. The strongest transition is $^4G_{5/2} \rightarrow {}^6H_{7/2}$ at 601 nm. We observed that the highest emission intensity belongs to 2.12 % sample. Therefore, we can say that 2.12 % is critical amount of doping and at other doping amount samples luminescence intensity is less than this sample luminescence intensity. We can explain this situation with concentration quenching phenomena.

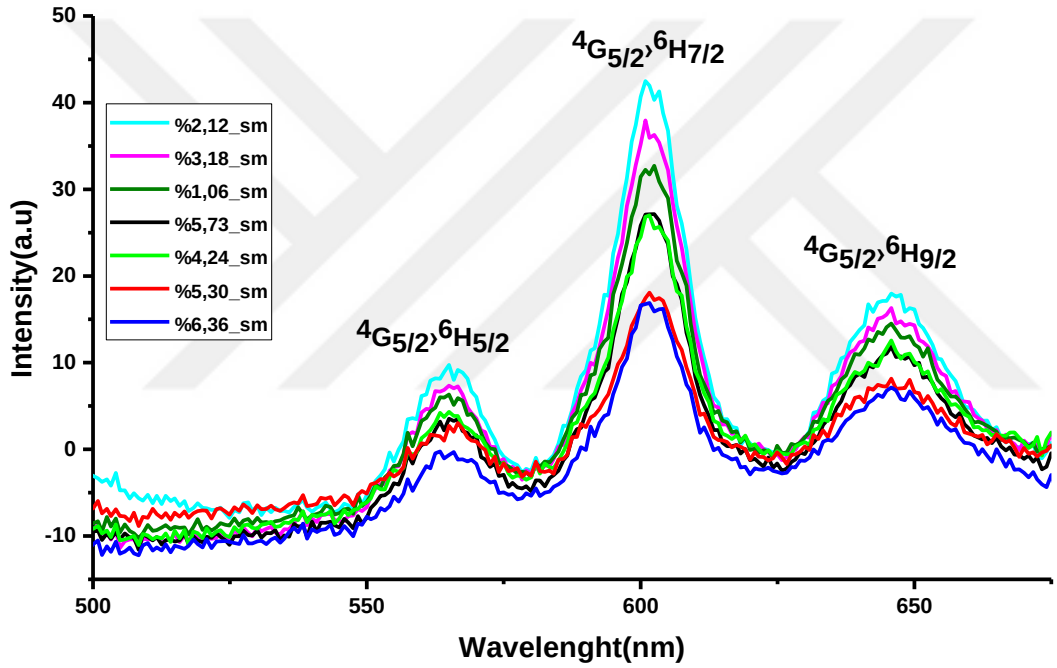


Figure 44. PL spectra of Sm doped $LaBO_3$ samples.

Figure 45 illustrates the luminescence spectra of Tb doped $LaBO_3$ samples at various concentrations. We observed four emission peaks when excited at 378 nm and these four peaks are at 489, 545, 586 and 622 nm. These bonds are $^5D_4 \rightarrow {}^7F_6$, $^5D_4 \rightarrow {}^7F_4$ and $^5D_4 \rightarrow {}^7F_3$, $^5D_4 \rightarrow {}^7F_2$ transitions, respectively. The strongest transition $^5D_4 \rightarrow {}^7F_4$ is at 545 nm. In addition, the critical doping amount of Tb is also 2.12 %. When the doping amount exceeds 2.12 %, we observed that concentration quenching lowers the luminescence intensity significantly.

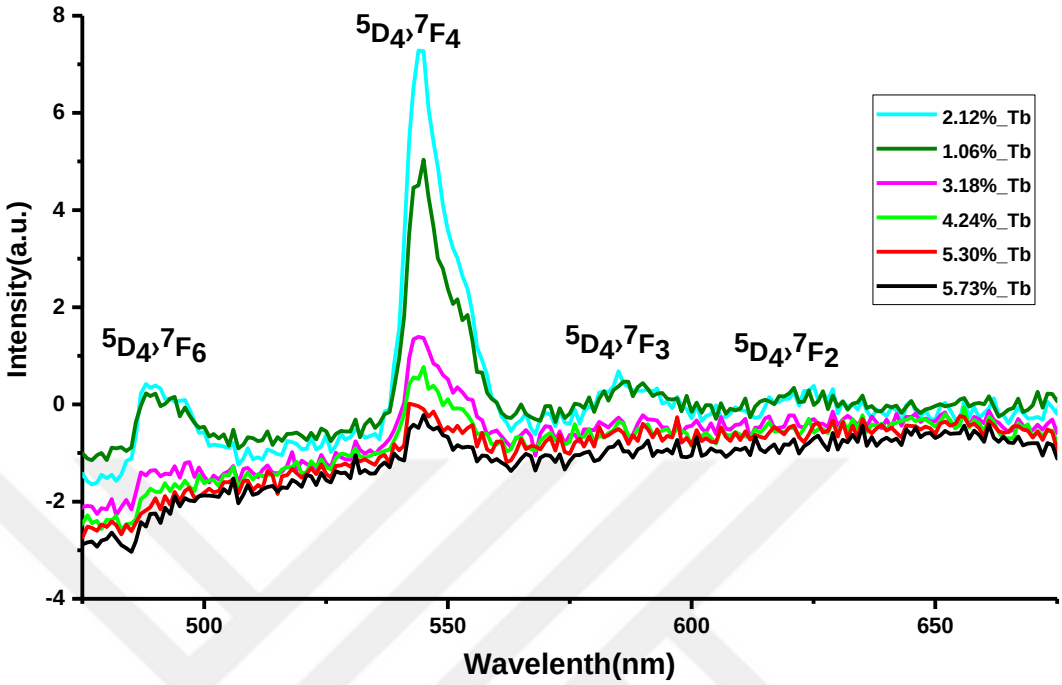


Figure 45. PL spectra of Tb doped $LaBO_3$ samples.

3.4.2 Dy, Sm, Tb doped $GdBO_3$ Luminescence Results

1.06, 2.12, 3.18, 4.24, 5.30, 5.73, 6.36 % doped Dy: $GdBO_3$ samples luminescence characteristics were examined and luminescence intensities were compared. **Figure 46** illustrates luminescence spectra of Dy doped $GdBO_3$ samples. We observed three emissions peaks. When these samples were excited at 312 nm, the observed bands are at 481, 575 and 670 nm. These peaks are $^4F_{9/2} \rightarrow {}^6H_{15/2}$, $^4F_{9/2} \rightarrow {}^6H_{13/2}$ and $^4F_{9/2} \rightarrow {}^6H_{11/2}$. When we look at spectra, we noticed that first peak has a shoulder at 488 nm. This situation might be explained by the relation of crystal structure of host, borate units of host and host-guest interaction. $GdBO_3$ crystal type is vaterite in which borate units are tetrahedral $B_3O_9^{9-}$ so we observed different luminescence spectra from Dy doped $LaBO_3$ samples' luminescence spectra in which borate units are planar BO_3^{3-}. In addition, 5.73 % Dy doped sample has the best luminescence character. Also, 6.36 % Dy doped $GdBO_3$ sample luminescence intensity is lower than 5.73 % Dy doped sample and we can describe this situation with concentration quenching.

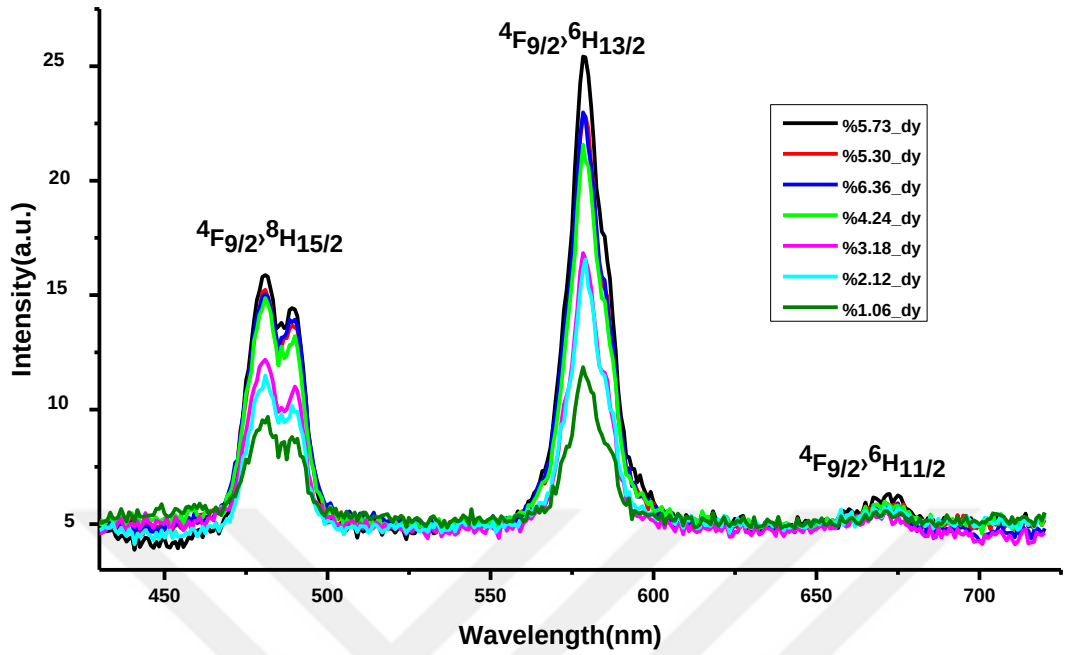


Figure 46. PL spectra of Dy doped $GdBO_3$ samples.

Figure 47 illustrates different amount Sm doped $GdBO_3$ samples' luminescence spectra. Luminescence results demonstrate that we have observed three emission peaks between 430-700 nm when excited at 407 nm. These emission peaks are at 570, 608, 650 nm. We assign these peaks to $^4G_{5/2} \rightarrow {}^6H_{5/2}$, $^4G_{5/2} \rightarrow {}^6H_{7/2}$ and $^4G_{5/2} \rightarrow {}^6H_{9/2}$ transitions, respectively. The most intense peak's transition is $^4G_{5/2} \rightarrow {}^6H_{7/2}$ at 608 nm. We detected that 5.30 % Sm doped sample luminescence intensity is slightly higher than other samples. In addition, all samples' intensities are almost the same except from 1.06 % Sm doped sample. We didn't increase doping amount because 5.73 % and 6.36 % Sm doped samples' emission intensities are slightly less than 5.30 % samples' emission intensity. When we increased doping amount, concentration quenching was occurred.

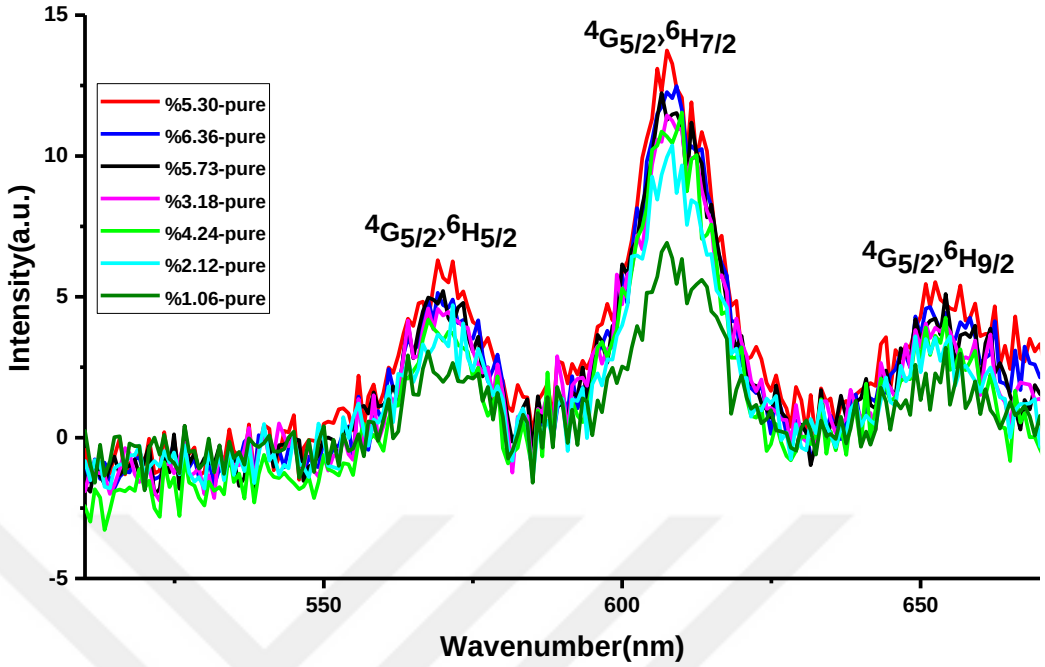


Figure 47. PL spectra of Sm doped $GdBO_3$ samples.

Figure 48 demonstrates 2.12 % Tb doped $GdBO_3$ samples luminescence spectra. Luminescence results demonstrate that we have observed three emission peaks as expected between 430-700 nm when excited at 378 nm. These emission peaks are at 484, 544, 578 and 622 nm, and assigned to $^5D_4 \rightarrow {}^7F_6$, $^5D_4 \rightarrow {}^7F_4$ and $^5D_4 \rightarrow {}^7F_3$, $^5D_4 \rightarrow {}^7F_2$ transitions, respectively. The most intense peak's transition is $^5D_4 \rightarrow {}^7F_4$ at 544 nm. We detected only that 2.12 % Tb doped sample luminescence intensity. We used 25mm sputtered edgepass filter, longpass 450 nm thorlabs filter to clean up the strong light observed at the spectrum. Thus, a longer data collection time with higher voltage setting at the detector can be utilized. The spectrum is collected at ~10 nm resolution then appears as digitized. The main idea was to successfully observe the emission bands of Tb. No further studies were carried out since Tb emission was very weak.

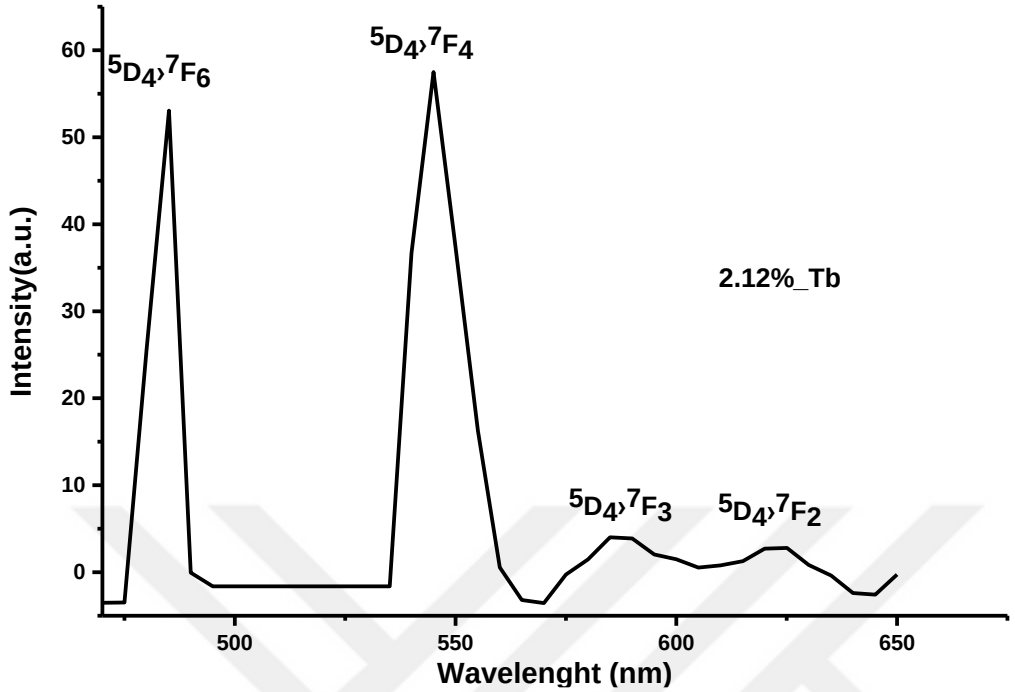


Figure 48. PL spectrum of Tb doped $GdBO_3$.

3.4.2 Dy, Sm, Tb doped YBO_3 Luminescence Results

Figure 49 shows different concentration Dy doped YBO_3 luminescence spectra. Emission spectra of Dy doped YBO_3 samples at various concentration were collected at 351 nm excitation. When samples were excited at 351 nm, we observed two major peaks. These peaks are at 481 nm and 579 nm and are assigned to $^4F_{9/2}\rightarrow{}^6H_{15/2}$, $^4F_{9/2}\rightarrow{}^6H_{13/2}$ transitions, respectively. Dy doped YBO_3, we noticed that $^4F_{9/2}\rightarrow{}^6H_{11/2}$ transition was not observed because YBO_3 host's luminescence intensities are much lower than Dy doped $LaBO_3$ luminescence intensities. Thus, it appears that the low intensity transition is buried under the noise. The relatively lower intensities observed in the YBO_3 host when doped with Dy can be explained with the help of their crystal structure. ATR results show that borate units of $LaBO_3$ are planar BO_3^{3-} however borate units of YBO_3 and $GdBO_3$ are tetrahedral $B_3O_9^{9-}$. It appears that the planar BO_3^{3-} is a preferred structure than the tetrahedral one for the luminescence. In addition, 5.30 % Dy doped sample has best luminescence character. Also, 6.36 % and 5.73 % Dy doped samples luminescence intensities are lower than 5.73 % Dy doped sample and we can describe this situation with concentration quenching.

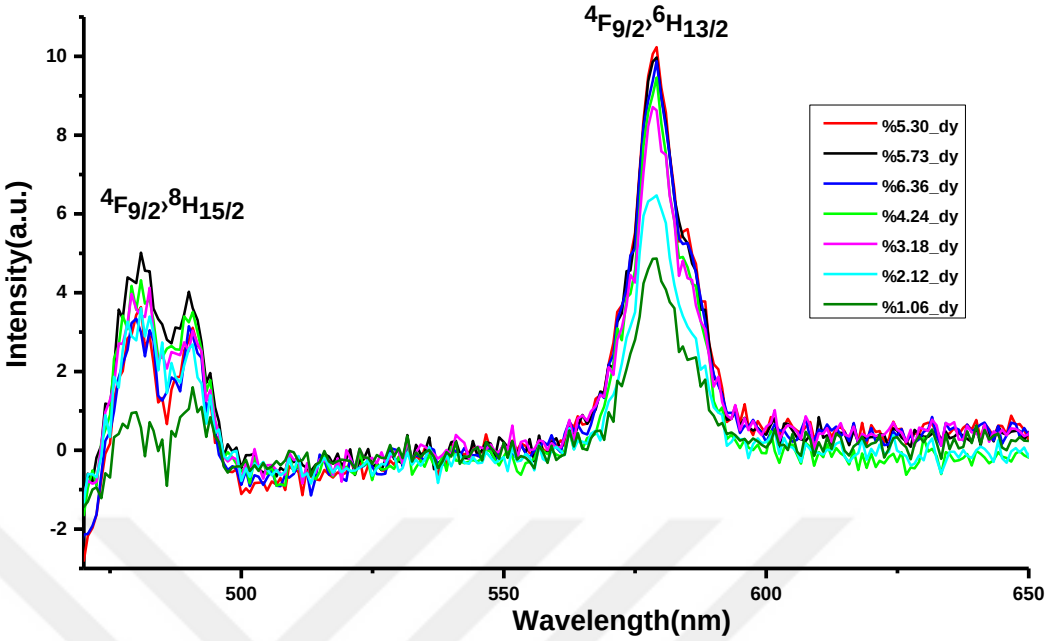


Figure 49. PL spectra of Dy doped YBO_3 samples.

Figure 50 illustrates different amount Sm doped YBO_3 samples luminescence spectra. Luminescence results exhibit that we observed three emission peaks between 430-700 nm when excited at 407 nm. These emission peaks are at 570, 609 and 656 nm and we assigned to $^4G_{5/2}\rightarrow{}^6H_{5/2}$, $^4G_{5/2}\rightarrow{}^6H_{7/2}$ and $^4G_{5/2}\rightarrow{}^6H_{9/2}$ transition, respectively. The most intense transition is $^4G_{5/2}\rightarrow{}^6H_{7/2}$ at 609 nm. We notice that 5.30 % Sm doped sample luminescence is slightly higher than other sample. However, the difference is very low and all samples' intensities are almost same apart from 1.06 % Sm doped sample. We didn't rise doping amount since 5.73 % and 6.36 % Sm doped samples intensities are lower than 5.30 % samples intensity. 5.73 % and 6.36 % samples luminescence intensities are lower than 5.30 % because of concentration quenching.

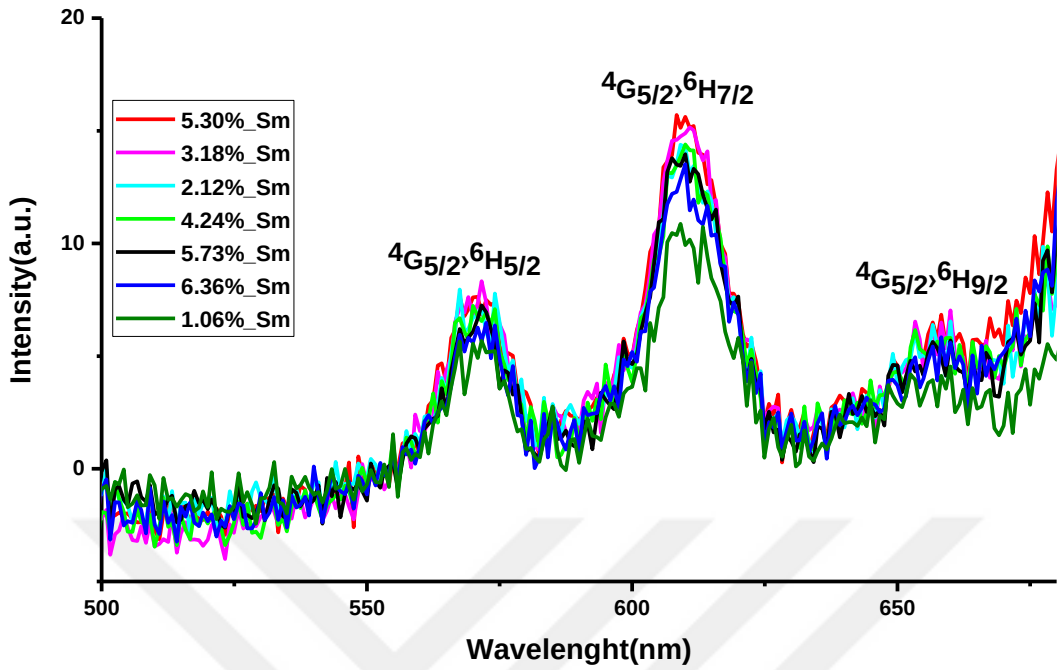


Figure 50. PL spectra of Sm doped YBO_3 samples.

Figure 51 demonstrates the luminescence spectra of Tb doped YBO_3 samples. We observed four emission bands when excited at 378 nm. These four peaks are at 489, 544, 587 and 623 nm corresponding to $^5D_4 \rightarrow {}^7F_6$, $^5D_4 \rightarrow {}^7F_4$ and $^5D_4 \rightarrow {}^7F_3$, $^5D_4 \rightarrow {}^7F_2$ transitions, respectively. The strongest transition is $^5D_4 \rightarrow {}^7F_4$ at 544 nm. In addition, the critical doping amount of Tb is 5.30 %, though the others are also very close. When the doping amount exceeds 5.30 %, we observed that concentration quenching occurs. An important point is that all samples spectra were collected directly from solid powder.

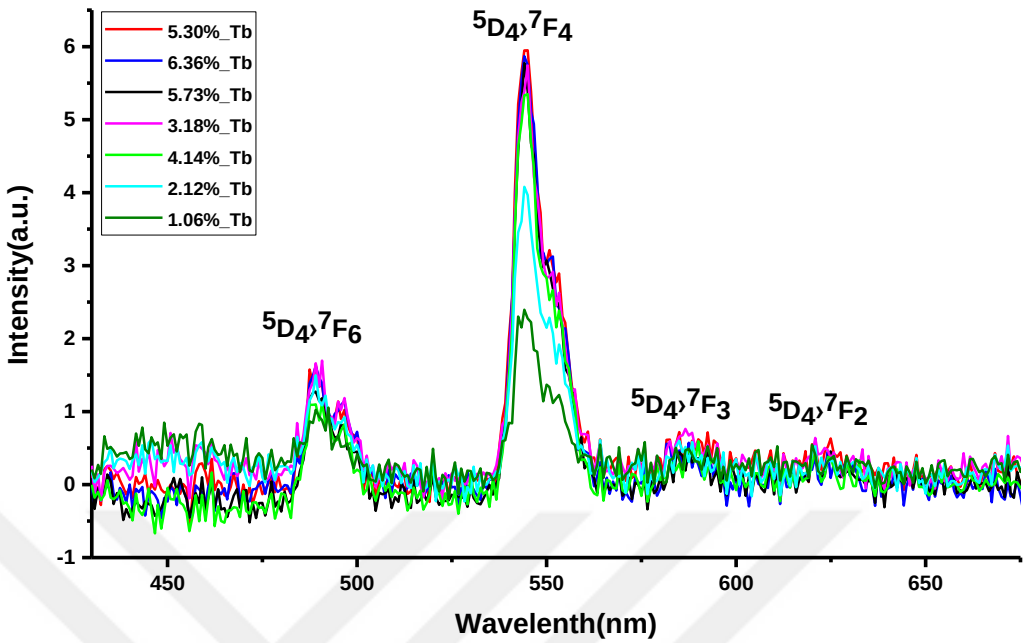


Figure 51. PL spectra of Tb doped YBO_3 samples.

3.5 Far-IR Results and Spectra

Far-IR measurements were made using Nicolet 6700 FTIR device. Prior to the data collection, the samples were placed inside the device for 1 hour as the sample compartment purged by dry. This way, strong water vapor interferences were minimized at low frequencies region. Pellets were prepared with HDPE (high density polyethylene) as matrix materials, use of HDPE made it possible to work between 70-1200 cm^{-1}. This way, low frequency bands especially below 500 cm^{-1} observed. The Far-IR measurement of undoped $LaBO_3$, $GdBO_3$ and YBO_3 were recorded for the first time, to best of our knowledge. In addition, the spectra of REE (Dy, Sm, Tb) doped $LaBO_3$, $GdBO_3$ and YBO_3 were collected to determine the effect of the doping on the host material vibrational signature.

In order to identify the peaks of REE doped three different hosts' samples, the spectra of REE doped samples were divided by the spectra of undoped samples. No quantitative results could be reached due to the fact that the pellets turned out to be non-homogenous. Thus, no connection could be made between luminescence and Far-IR spectra in terms of the amount of doping. The actual aim of this study is then to identify new bands if exist, as well as to identify shifts in existing bands and determine peaks at low and high frequencies.

3.5.1 Dy, Sm, Tb doped $LaBO_3$ Far-IR Results

Both the information from the literature and the Far-IR spectra in our studies show that the peaks at 611cm^{-1} and 592cm^{-1} are related with stretching and bending modes of planar BO_3^{3-} structure in **Figure 52**. Thus, the borate units of $LaBO_3$ structure are planar [59]**.** When the Far-IR spectra of Dy doped and undoped $LaBO_3$ are examined, no significant changes were observed in borate peaks. In addition, low frequency peaks appear on shoulders over a very broad band at 269, 188 and 138 cm^{-1} belong to La-O vibrational modes in La-O-B network. Furthermore, a new peak at 531cm^{-1} was observed, this band is most probably associated with the $LaBO_3$ structure as it appears in all of the spectra and not directly related with the dopant, Dy. Also, we observed that when doping amount increases, the band at 398 cm^{-1} appears the relative intensity of this band increases with the dopant amount and clearly directly related with the Dy. Since the band does not exist in the spectrum of undoped $LaBO_3$, the band might be associated with the interstitial Dy placement affecting the $LaBO_3$ modes or creating a new Dy-BO_3 modes. This may cause expansions in the structure. In addition, when $DyBO_3$ spectrum is analyzed, we observed 398cm^{-1} supporting the assignment of the band to $DyBO_3$ vibrational modes.

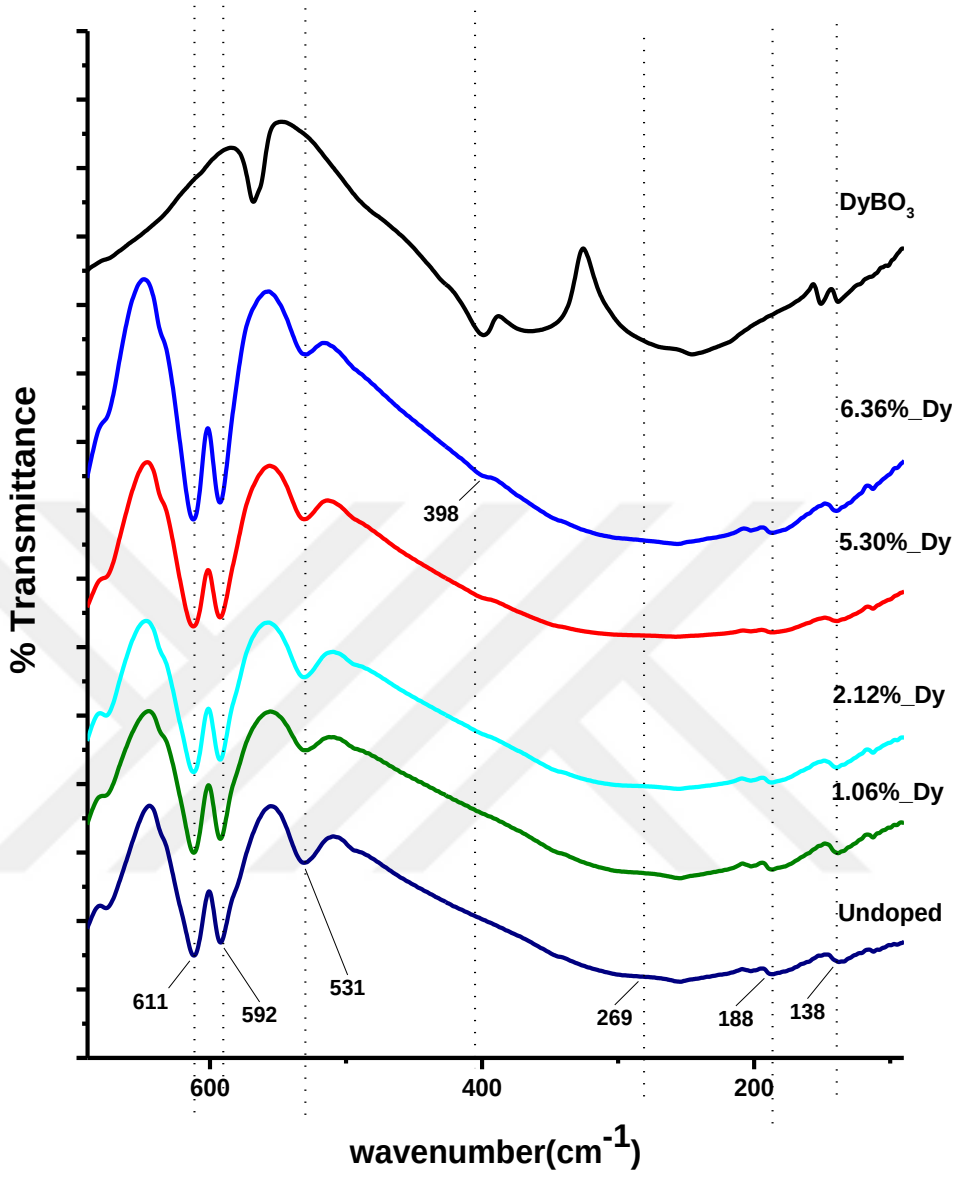


Figure 52. Far-IR spectra of undoped and Dy doped $LaBO_3$ and $DyBO_3$.

Figure 53 shows the Far-IR spectra of undoped and Sm doped $LaBO_3$ samples. La-O stretching modes in La-O-B network are at 296, 188 and 138 cm^{-1}. We didn't observe any other bands than may be associated with $SmBO_3$. So, we might say no newly peaks were formed.

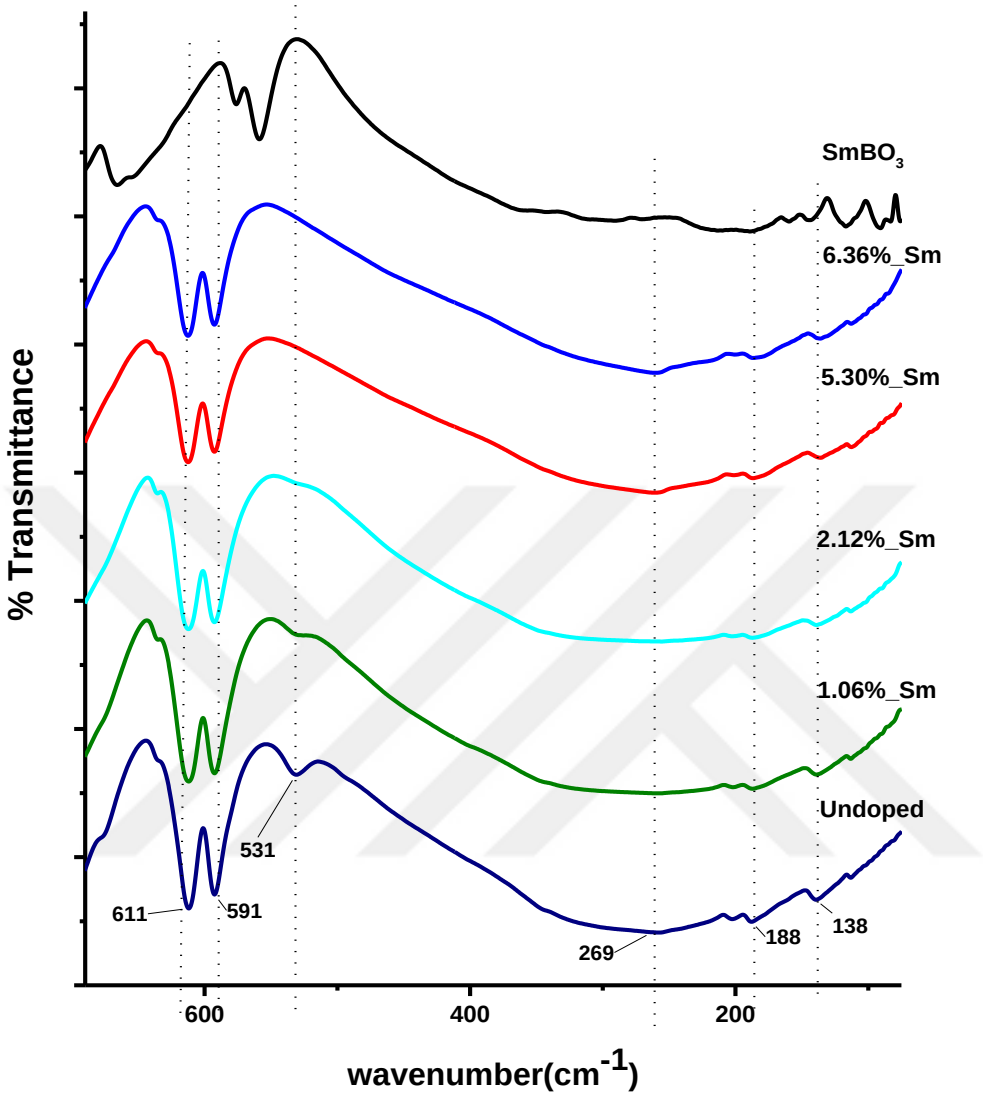


Figure 53. Far-IR spectra of undoped and Sm doped $LaBO_3$ and $SmBO_3$.

Figure 54 demonstrate Far-IR spectra of undoped and Tb doped $LaBO_3$ samples. L-O stretching modes in La-O-B network are at 296, 188 and 138 cm^{-1} appearing as shoulder is a very broad band. Similar to the Dy doping case, we observed some differences between undoped and Tb doped $LaBO_3$ samples. When doping amount rises, a band that is most probably associated with, $TbBO_3$ is observed at 396 cm^{-1}. This suggest that some of the Tb is placed in the interstitial position, same as the Dy case.

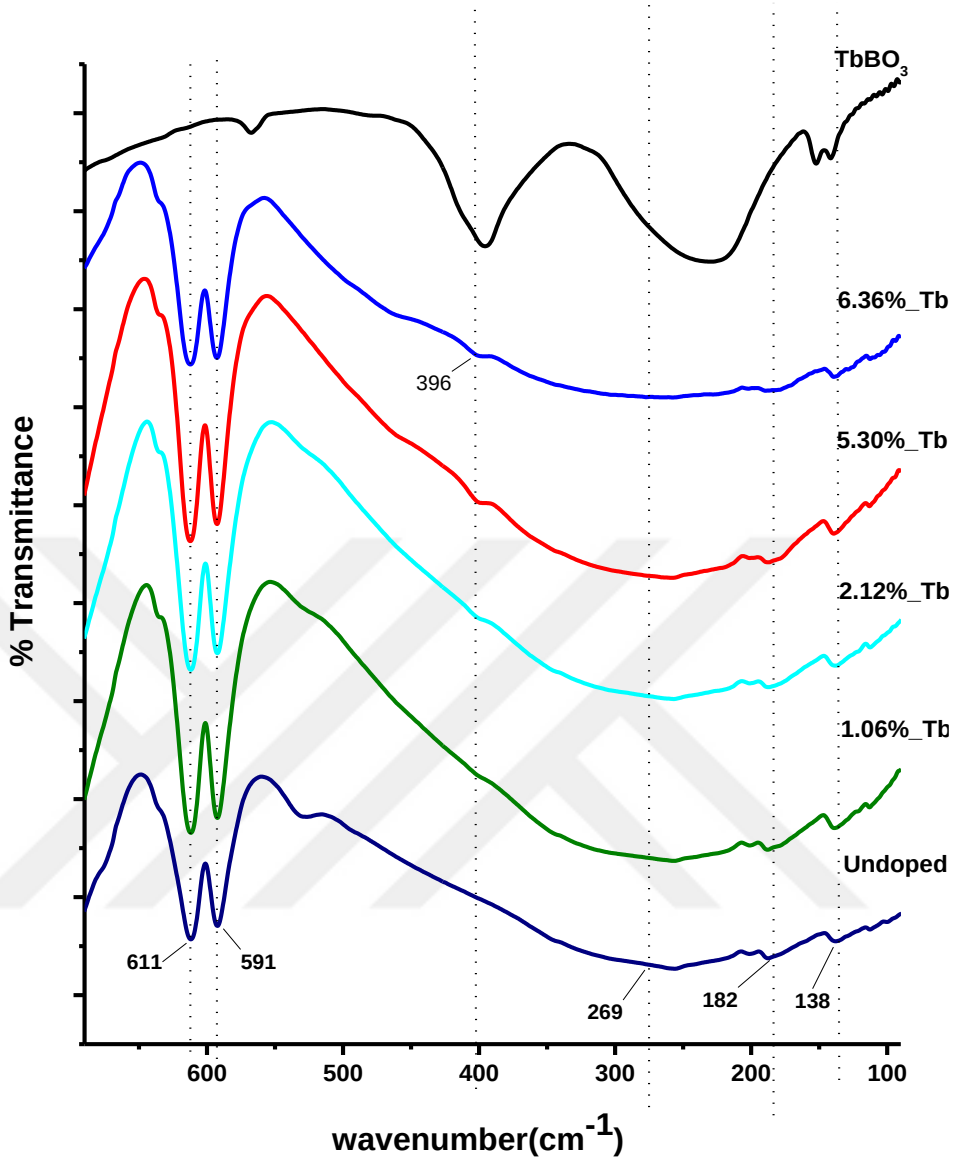


Figure 54. Far-IR spectra of undoped and Tb doped $LaBO_3$ and $TbBO_3$.

3.5.2 Dy, Sm, Tb doped $GdBO_3$ Far-IR Results

Figure 55 illustrate undoped and Dy doped $GdBO_3$ samples Far-IR spectra. We observed that there are no significant alterations when the $GdBO_3$ is doped with Dy. Distinct low frequency peaks are observed at 479, 398, 393, 368, 242, 150 and 141 cm^{-1}. We suggest that these peaks belong to Gd-O stretching modes in the Gd-O-B network. In addition, at 564 cm^{-1} peak might point tetrahedral $B_3O_9^{9-}$ bending mode. There is no significant difference between $DyBO_3$ and $GdBO_3$ Far-IR spectra. This

suggests that Dy doping is mainly substitutional. Considering that any interstitial doping should affect at least some of the bands. However, we should also note that the doping amounts are fairly low.

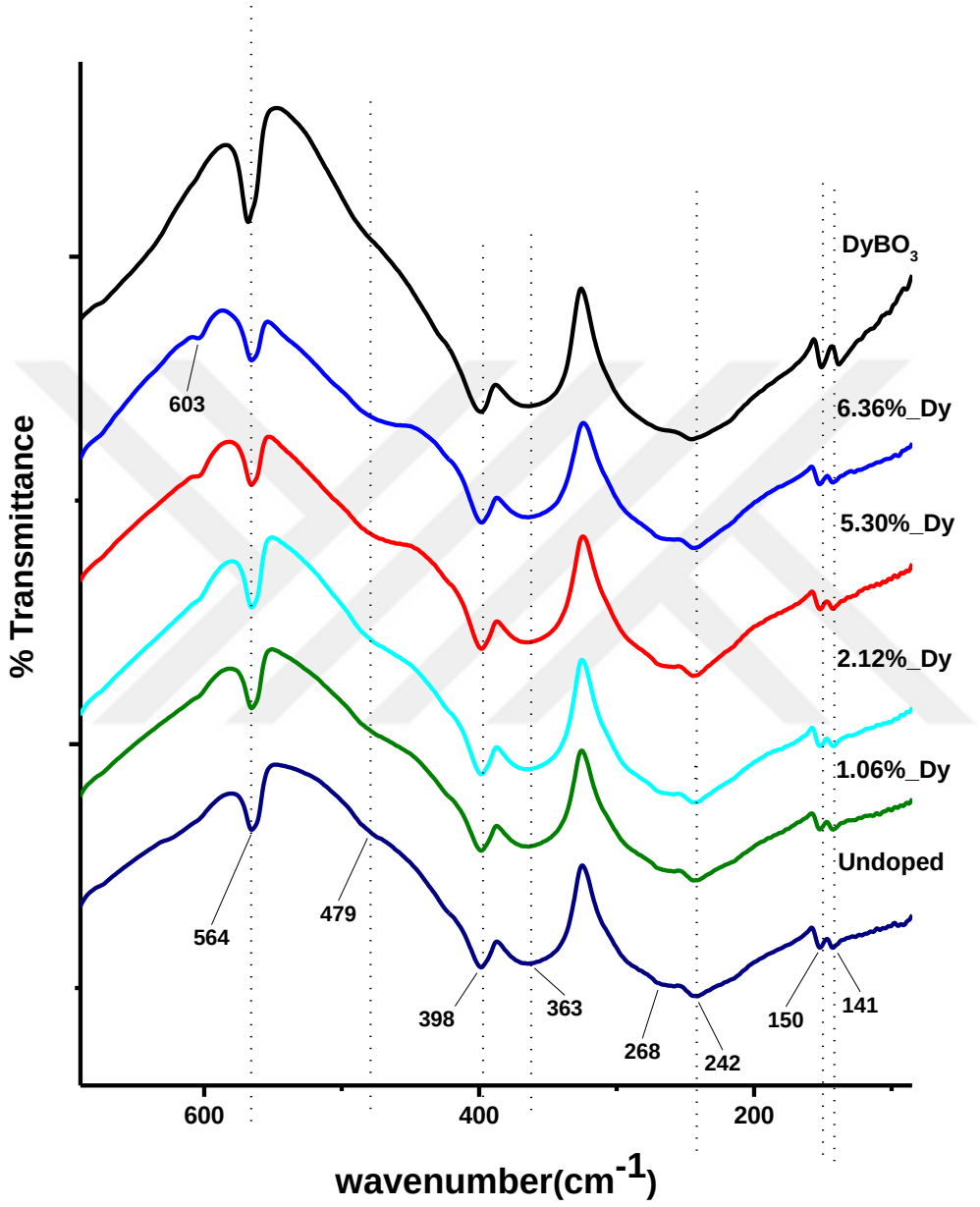


Figure 55. Far-IR spectra of undoped and Dy doped $GdBO_3$ and $DyBO_3$.

Figure 56 shows the spectra of undoped and Sm doped $GdBO_3$ samples. Gd-O vibration frequencies are at 477, 399, 362, 245, 148, 141 cm^{-1}. In addition, $B_3O_9^{9-}$ bending mode is at 566 cm^{-1}. In addition, we didn't observe low frequency $SmBO_3$

peaks. So, we might conclude that Sm does not affect low frequency vibrations modes, when doping amounts are between 1.06 % and 6.36 %.

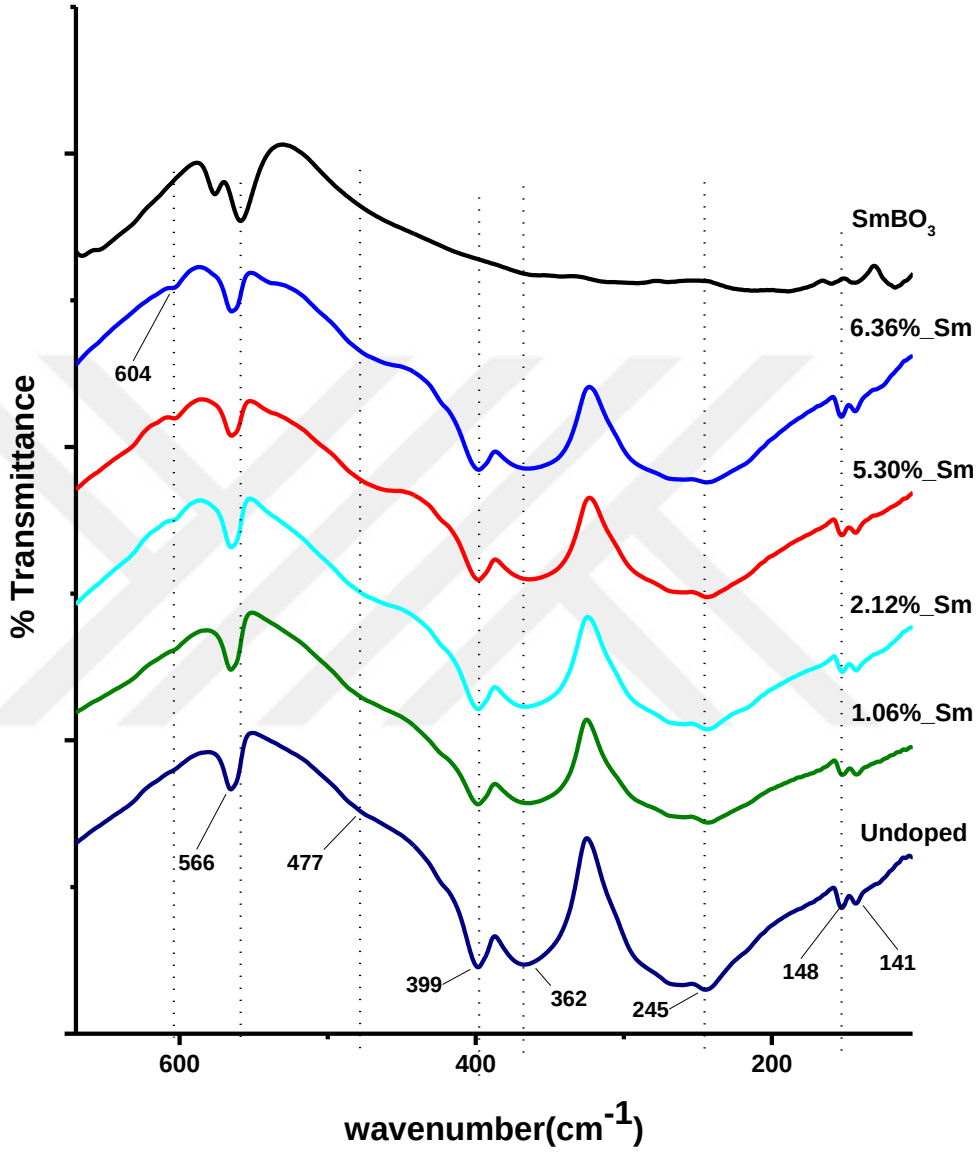


Figure 56. Far-IR spectra of undoped and Sm doped $GdBO_3$ and $SmBO_3$.

Figure 57 demonstrates the spectra of undoped and Tb doped $GdBO_3$ samples. Gd-O vibration frequencies are at 478, 397, 358, 243, 153 and 144 cm^{-1}. In addition, $B_3O_9^{9-}$ bending mode is at 566 cm^{-1}. $TbBO_3$ and $GdBO_3$ Far-IR spectra are same and we didn't note any significant differences so this suggests that Tb doping is mainly

substitutional. Considering that any interstitial doping should affect at least some of the bands. However, we should also note that the doping amounts are fairly low.

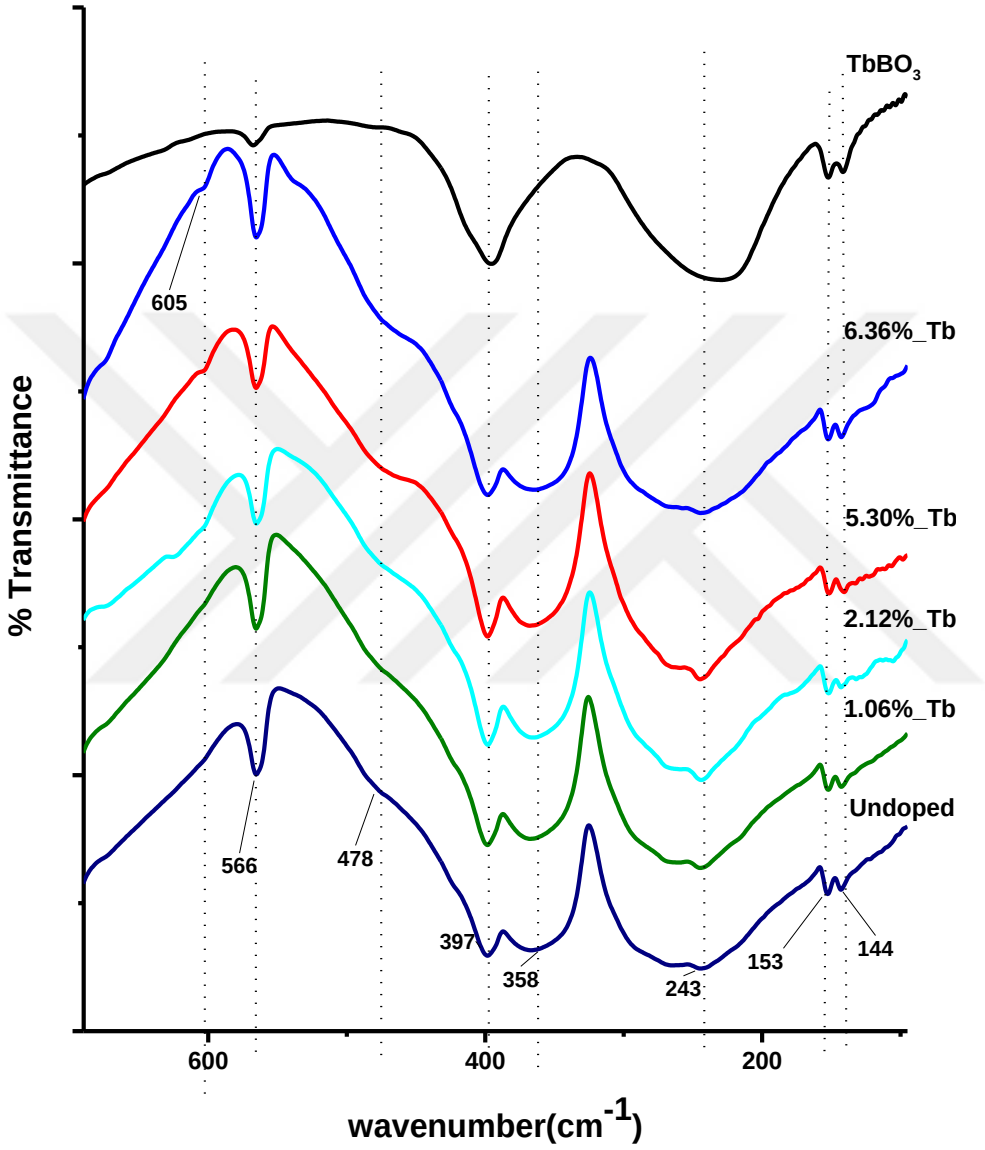


Figure 57. Far-IR spectra of undoped and Tb doped $GdBO_3$ and $TbBO_3$.

3.5.3 Dy, Sm, Tb doped YBO_3 Far-IR Results

Figure 58 demonstrates the spectra of undoped and Dy doped YBO_3 samples. Different doping amounts and spectrum of undoped sample have similar Far-IR

spectra. We didn't observe doping effect because we didn't detect any new peaks or shifting. The peaks at 404, 287, 202, 180 cm^{-1} belong to Y-O stretching modes in the Y-O-B network. In addition, the peak that belongs to tetrahedral $B_3O_9^{9-}$ bending mode appears at 570 cm^{-1}.

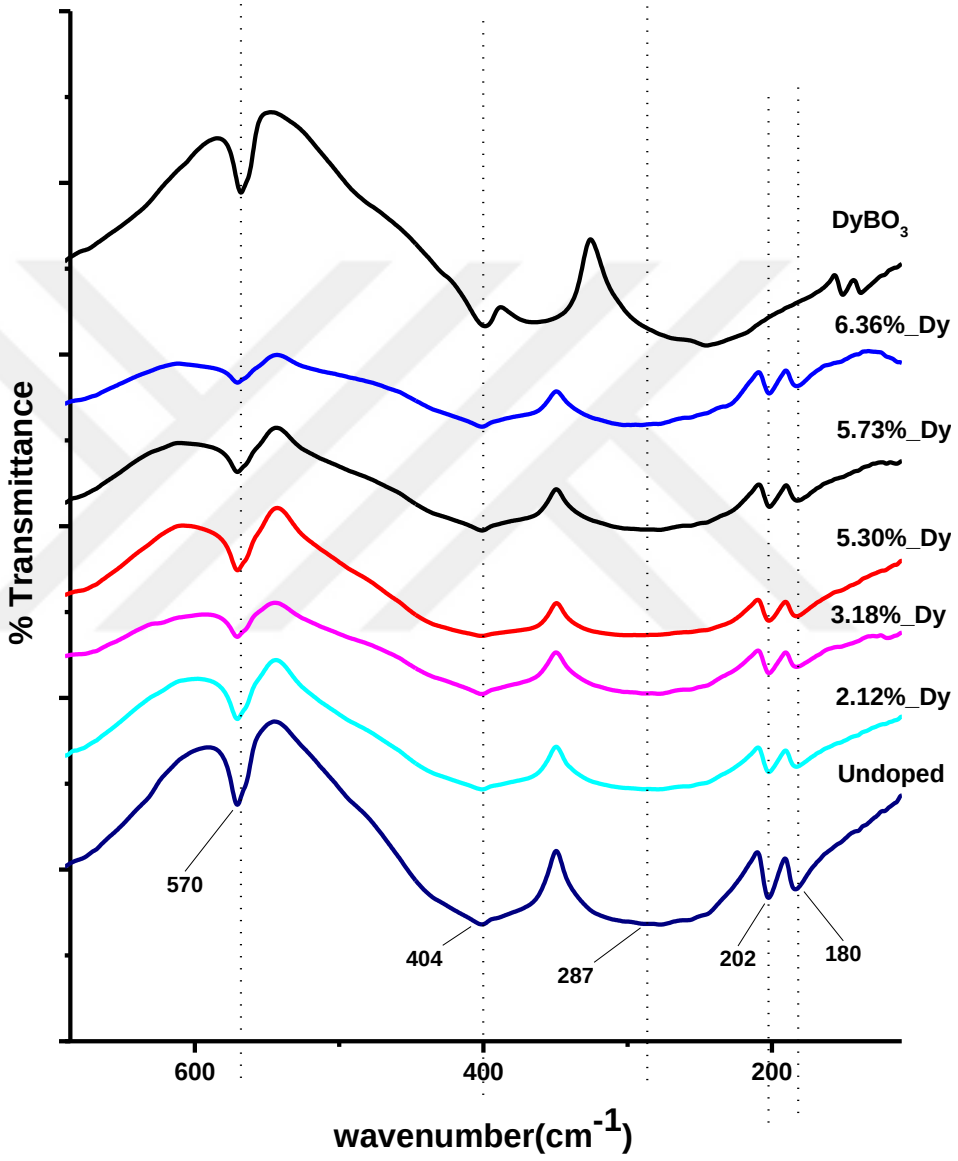


Figure 58. Far-IR spectra of undoped and Dy doped YBO_3 and $DyBO_3$.

Figure 59 shows the Far-IR spectra of undoped and Sm doped YBO_3 samples and **Figure 60** demonstrates the Far-IR spectra of undoped and Tb doped YBO_3 samples.

The Far-IR results of Tb and Sm doped samples are the same with the results of Dy doped samples. All spectra illustrate that undoped YBO_3 low frequency vibration modes and REE doped YBO_3 vibration modes are similar. We might conclude that all peaks related with Y-O vibration modes in the Y-O-B network.

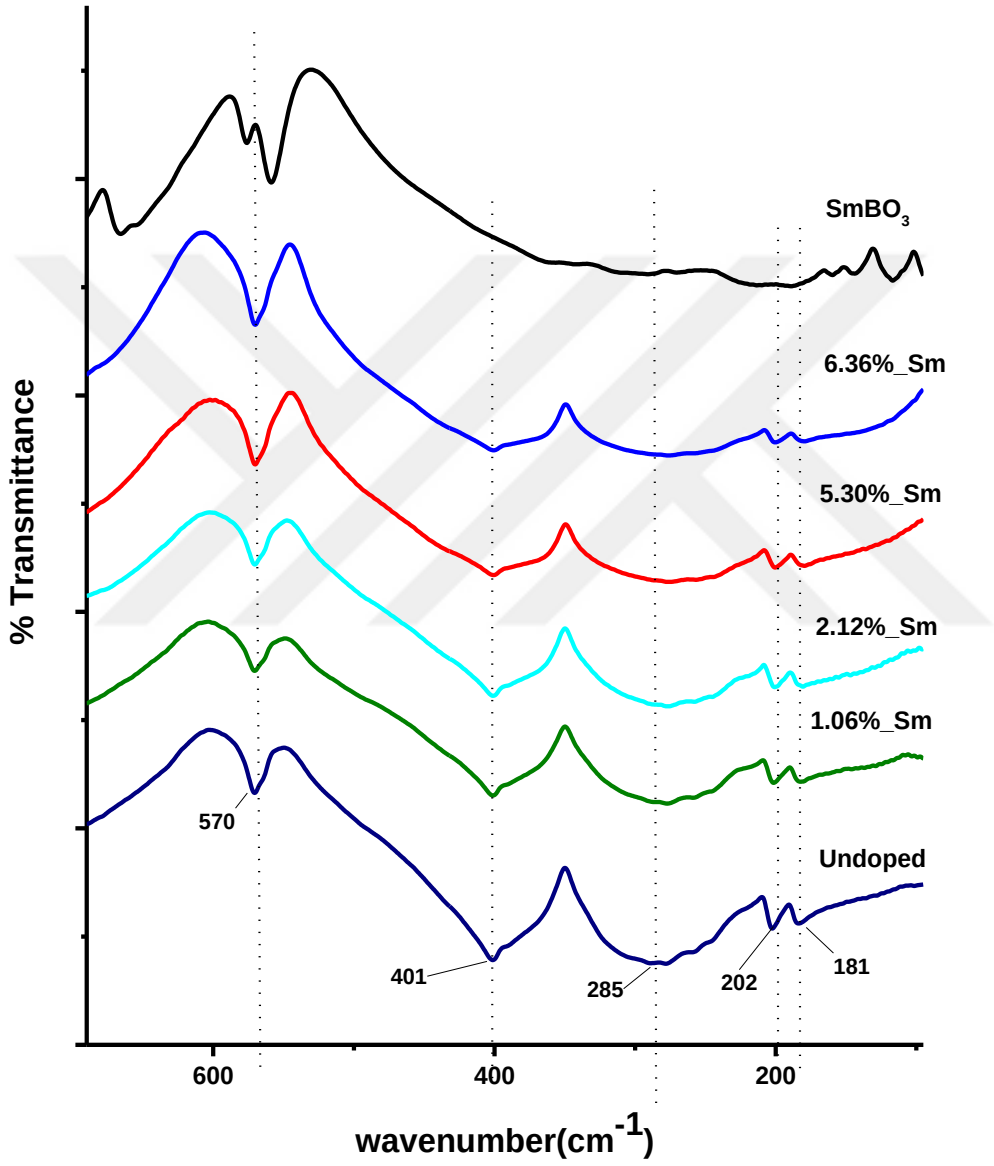


Figure 59. Far-IR spectra of undoped and Sm doped YBO_3 $SmBO_3$.

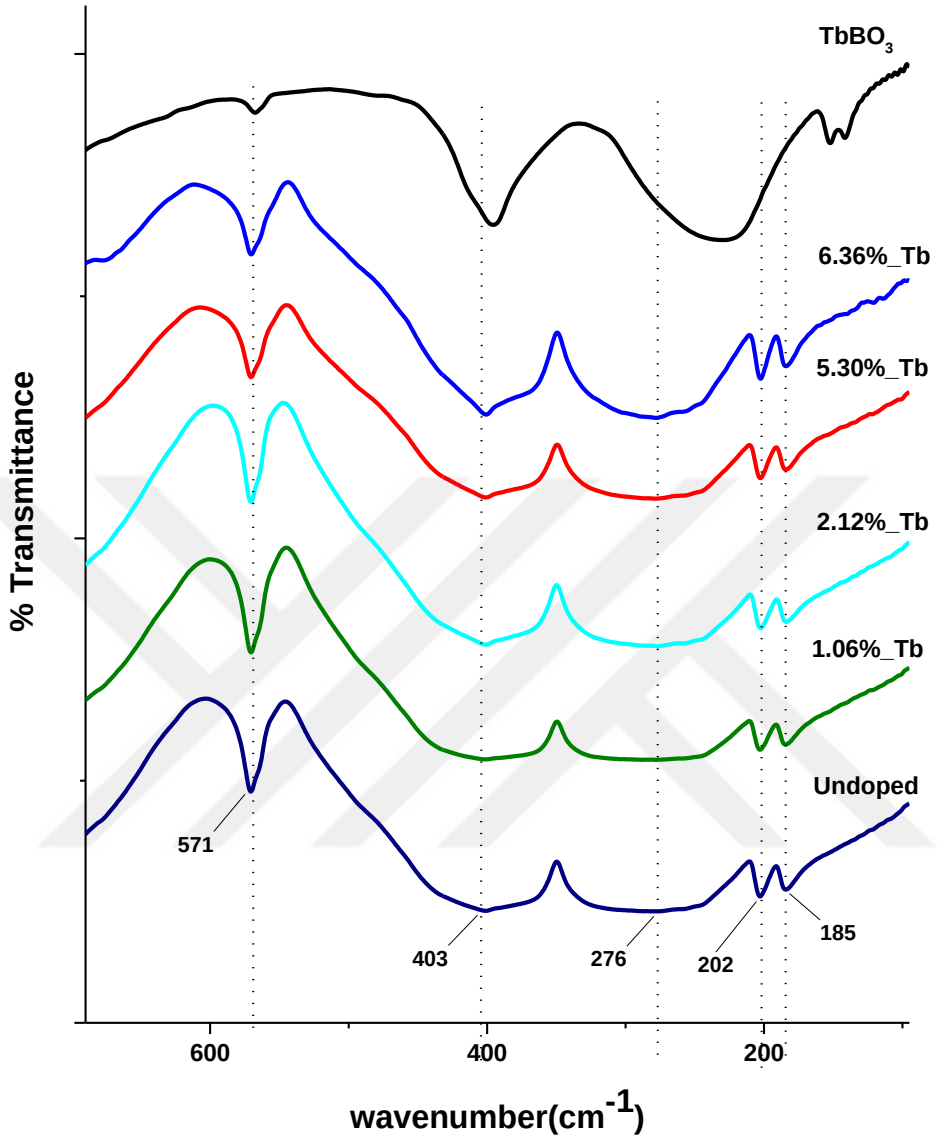


Figure 60. Far-IR spectra of undoped and Tb doped YBO_3 and $TbBO_3$.

Figure 61 shows the Far-IR spectra of rare earth oxide and boric acid. These results suggest the modes at low frequencies may belong to La-O, Gd-O, Y-O stretching modes. We didn't observe any boric acid bands in the spectra of products. As a result, this study shows that heavier atoms and oxygen band modes locate at low frequency.

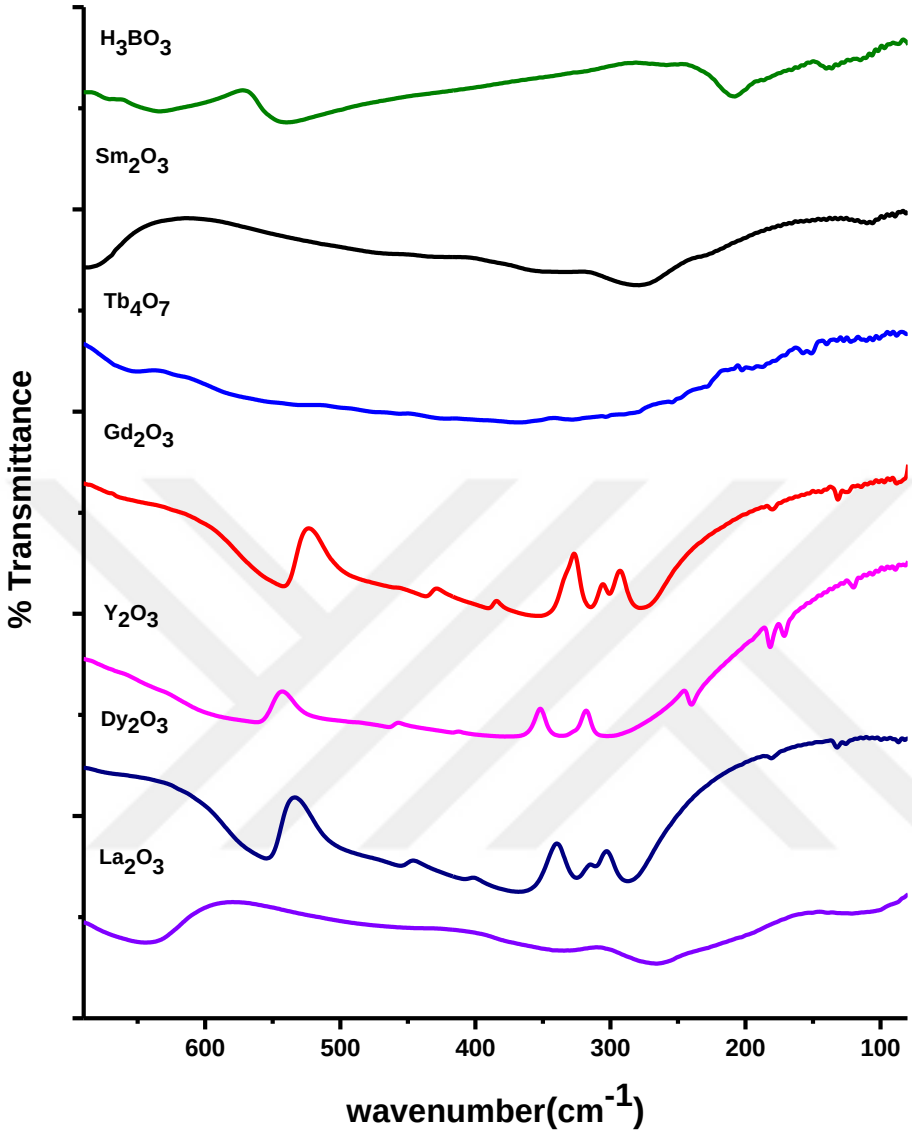


Figure 61. Far-IR spectra of boric acid and RE oxides.

3.6 CIE results

3.6.1 Dy, Sm and Tb doped $LaBO_3$ CIE results

CIE chromaticity coordinates are calculated using Matlab (Matrix Laboratory) the program calculate integrated peaks' area from the PL spectrum and result the X, Y, Z values and x, y values.

In **Figure 62**, the CIE Chromaticity coordinates calculated from the PL spectrum of 5.30 % Dy doped $LaBO_3$ sample. We observed that Dy doped $LaBO_3$ sample color is pale yellow with x =0.42 and y =0.44 coordinates. Different doping concentrations do not change the color observed in all hosts and doping agents. This is due to the fact that when host ion and doping ion radii are very close in dimension to each other, the ratio of Y/B does not change with changing concentrations of doping agent [71]. As a result; no significant differences were observed between Dy doped $LaBO_3$ samples.

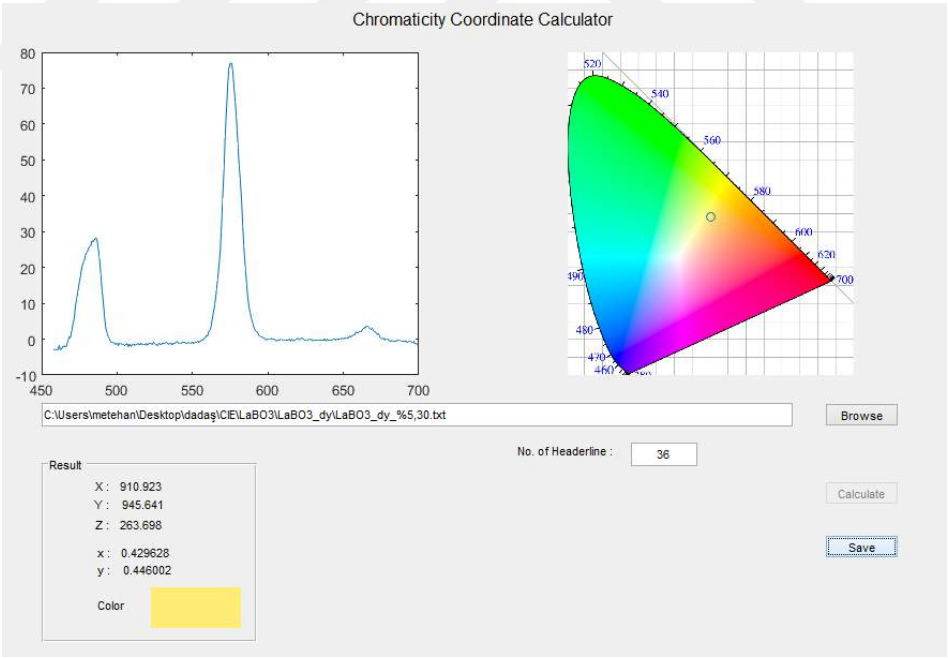


Figure 62. 5.30 %: Dy doped $LaBO_3$ CIE results.

The CIE Chromaticity coordinates of Sm doped $LaBO_3$ sample is given in **Figure 63**. We observed that Sm doped $LaBO_3$ sample color is a darker orange and x =0.58 and y =0.40 coordinates. Also, no significant differences were observed between Sm doped $LaBO_3$ samples in color.

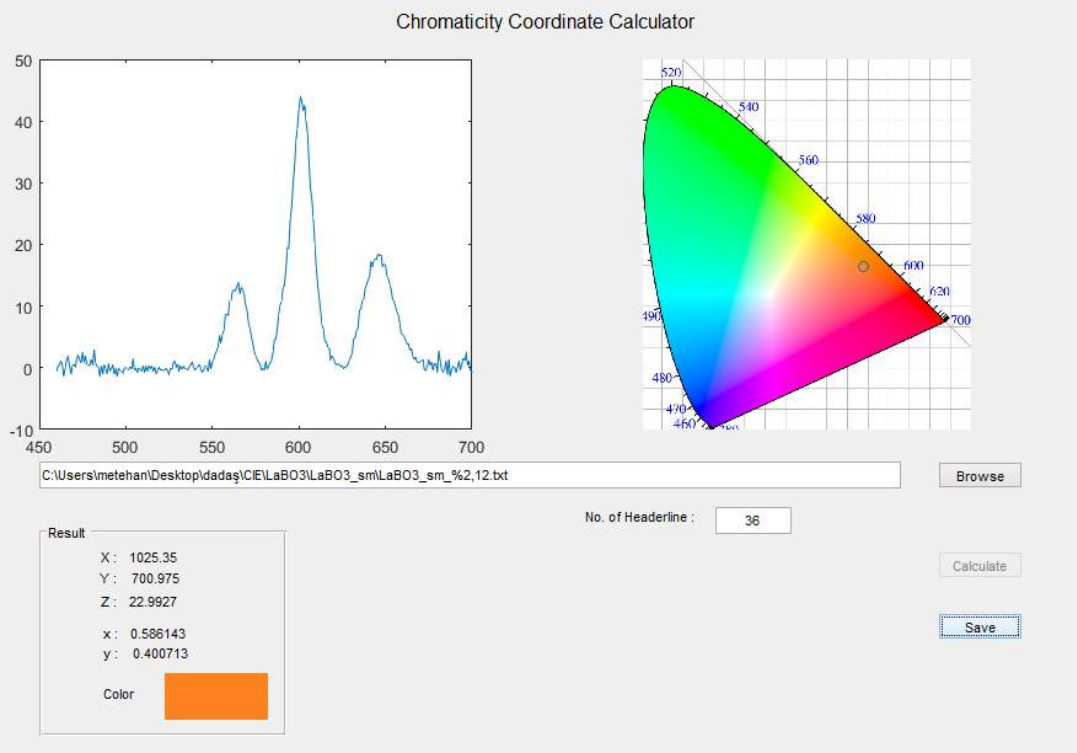


Figure 63. 2.12 %: Sm doped $LaBO_3$ CIE results.

The CIE Chromaticity coordinates of Tb doped $LaBO_3$ sample is presented in **Figure 64**. We observed that Tb doped $LaBO_3$ sample color is green and x =0.29 and y =0.62 coordinates. As a results, we have also not observed any significant alterations in color between Tb different concentrations of doped $LaBO_3$ samples.

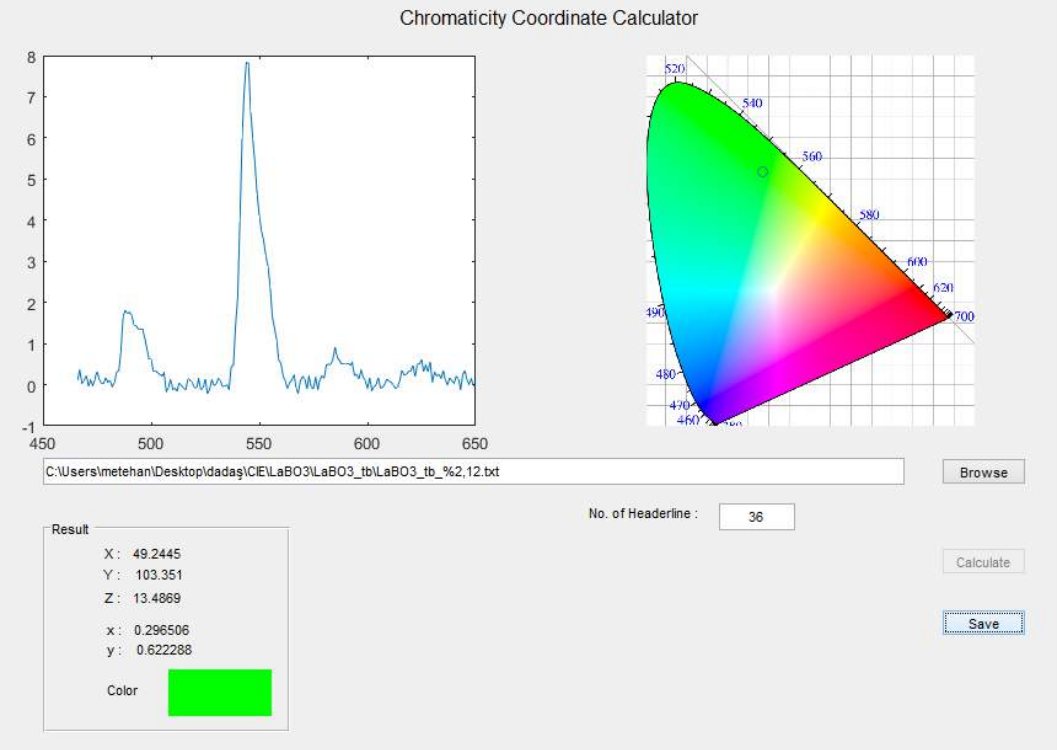


Figure 64. 2.12 %: Tb doped $LaBO_3$ CIE results.

3.6.2 Dy and Sm doped $GdBO_3$ CIE results

In **Figure 65**, the CIE Chromaticity coordinates belong to Dy doped $GdBO_3$ sample. We observed that Dy doped $GdBO_3$ sample color is pale peach and x =0.40 and y =0.40 coordinates. Also, all Dy doped $GdBO_3$ products have almost the same color and no significant differences were observed.

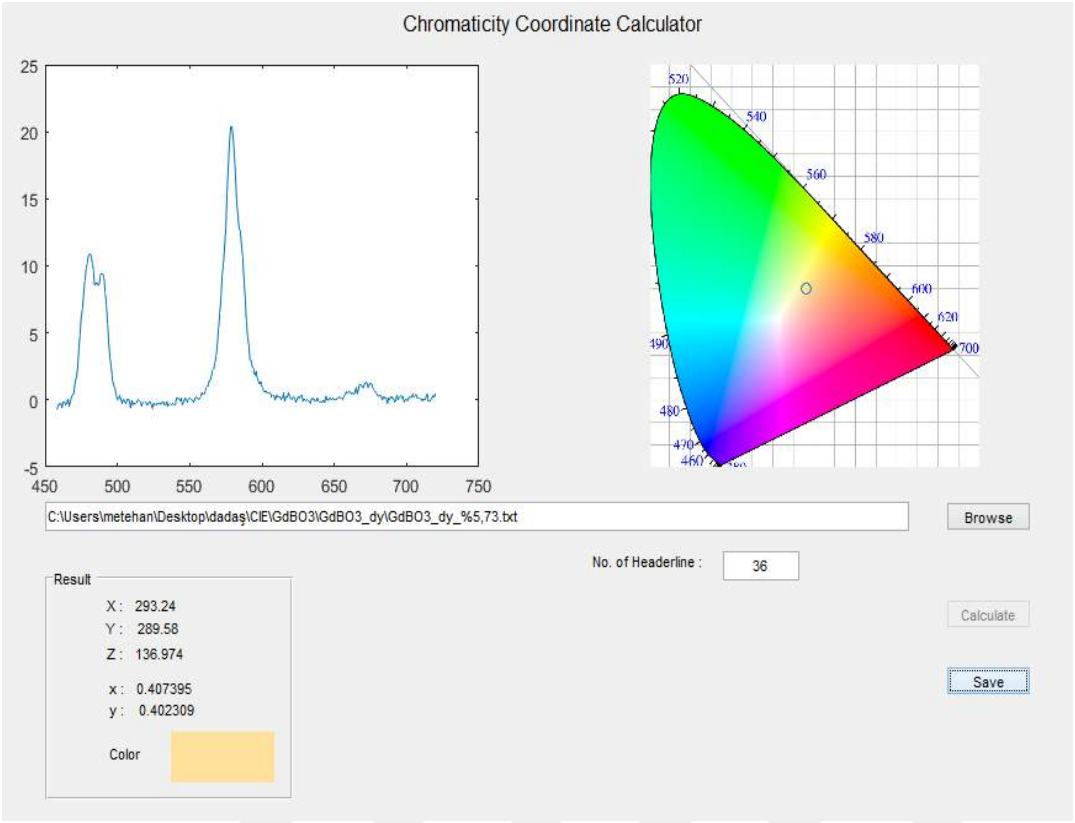


Figure 65. 5.73 %: Dy doped $GdBO_3$ CIE results.

The CIE Chromaticity coordinates of Sm doped $GdBO_3$ sample is given in **Figure 66**. We observed that Sm doped $GdBO_3$ sample color is a slightly lighter orange and x =0.60 and y =0.39 coordinates. Also, the color in all Sm doped $GdBO_3$ the products were similar with negligible difference.

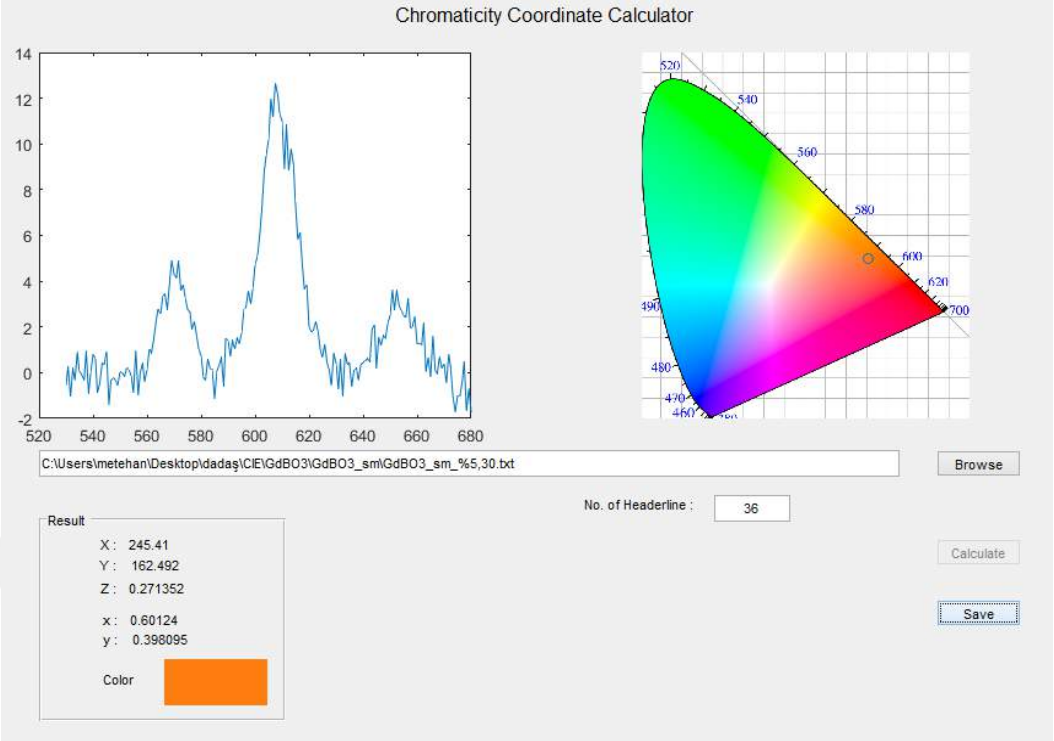


Figure 66. 5.30 %: Sm doped $GdBO_3$ CIE results.

3.6.3 Dy, Sm and Tb doped YBO_3 CIE results

The CIE Chromaticity coordinates of Dy doped YBO_3 sample are presented in **Figure 67**. We observed that Dy doped YBO_3 sample color is whitish yellow and x =0.39 and y =0.41 coordinates. Also, all Dy doped YBO_3 products have almost the same color and no significant differences were observed with changing concentration of doping.

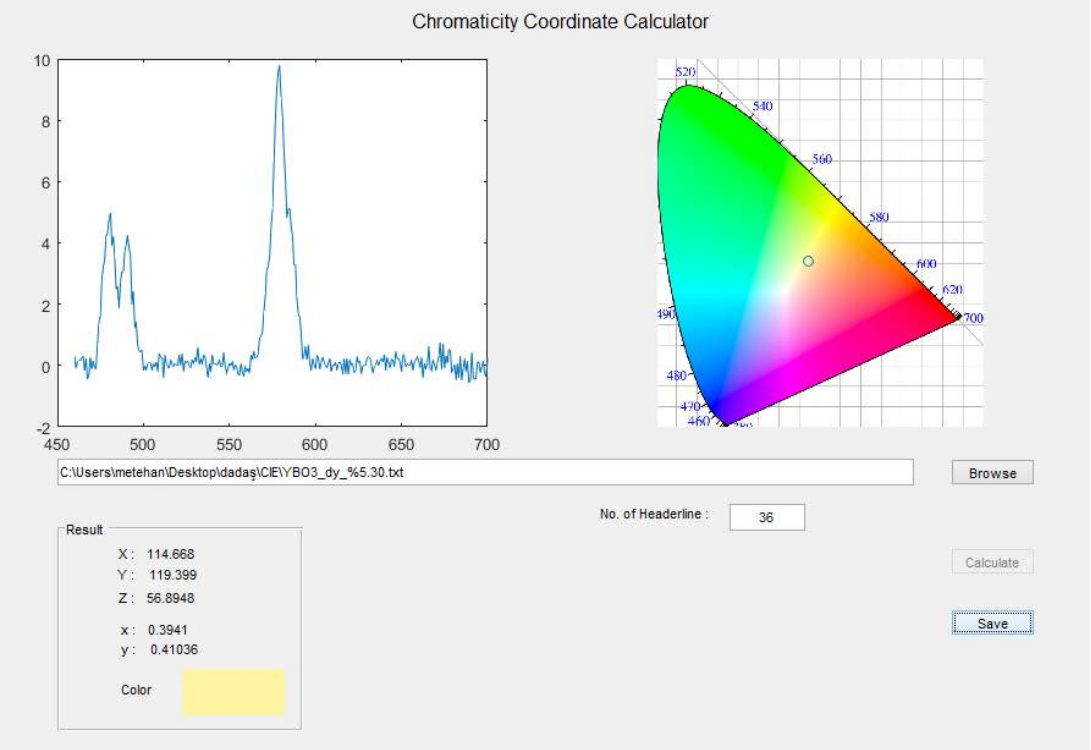


Figure 67. 5.30 %: Dy doped YBO_3 CIE results.

In **Figure 68**, the CIE Chromaticity coordinates belong to Sm doped YBO_3 sample. We observed that Sm doped YBO_3 sample color is a slightly lighter orange and x =0.60 and y =0.39 coordinates. As a results, all Sm doped YBO_3 products have almost the same color and no significant differences were observed.

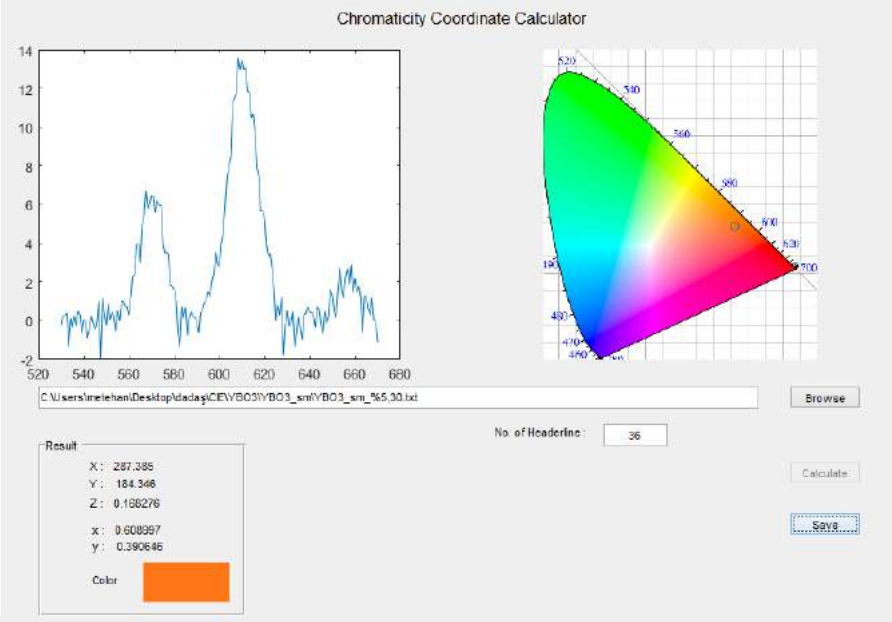


Figure 68. 5.30 %: Sm doped YBO_3 CIE results.

In **Figure 69**, the CIE Chromaticity coordinates belong to Tb doped YBO_3 sample. We observed that Tb doped YBO_3 sample color is a green and x =0.30 and y =0.63 coordinates. As a results, all Tb doped YBO_3 products have almost the same color and no significant differences were observed.

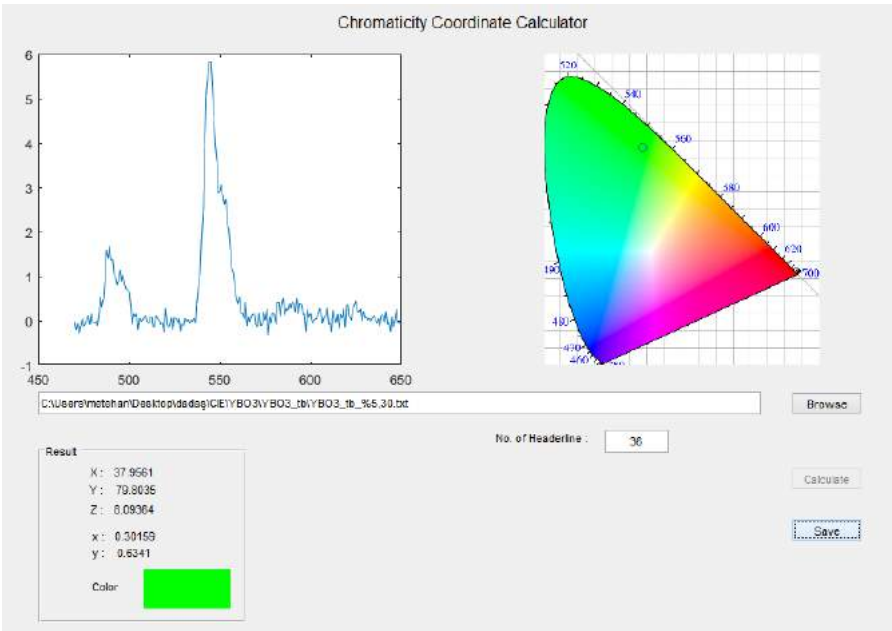


Figure 69. 5.30 %: Tb doped YBO_3 CIE results.

4. CONCLUSION AND RECOMMENDATIONS

X-Ray patterns of the compounds demonstrate that all the $LnBO_3$ (Ln: La, Gd, Y) samples were synthesized successfully by microwave-assisted solid state synthesis method. All the observed patterns of doped with Dy, Sm, Tb $LnBO_3$ and undoped $LnBO_3$ samples at various amount of doping levels are practically same so we suggest that all products synthesized with microwave assisted solid state method successfully. The space group of Dysprosium, Samarium and Terbium doped and undoped $LaBO_3$ samples is Pnma and crystal system is orthorhombic with unit cell diameters a=5.84 Å, b=8.18 Å and c=5.07 Å with card number JCPDS no: 12-0762. Similarly, undoped and Dy, Sm and Tb doped $GdBO_3$ samples have same structure space group $R3_2$ and crystal system is rhombohedral. The lattice parameters are a=6.63 Å and c=26.72 Å and card number JCPDS no: 13-0483. Undoped and Dy, Sm and Tb doped YBO_3 samples also have same powder diffraction patterns that result a space group C2/c and crystal structure monoclinic. In addition, the lattice parameters of this structure are: a=11.32 Å, b=6.54 Å and c=9.55 Å, β=112.955° and card number is JCPDS no :88-0356.

Undoped and REE doped $LaBO_3$ structure is confirmed with the observed give four vibration modes; ν1 symmetric stretching, ν2 out of plane bending, ν3 asymmetric stretching ν4 in-plane bending. We observed that type or amount of doping had no significant effect on these bands. The ν3 (asymmetric stretching) bands observed at 1255 cm^{-1} and ν1 (symmetric stretching) bands at 940 cm^{-1}, ν2 (out of plane bending) modes at 790, 708 cm^{-1}, ν4 (in-plane bending) mode at 611, 591 cm^{-1}. These vibrational modes show that the borate units of our doped and undoped $LaBO_3$ samples are planar BO_3^{3-}. REE and undoped $GdBO_3$ powders give six absorption bands, bending modes and stretching modes. The distortion frequencies are 578, 696 cm^{-1} and stretching frequencies are 821, 904, 980, 1054 cm^{-1}. These vibration modes indicate that the borate units of doped and undoped $GdBO_3$ samples are tetrahedral $B_3O_9^{9-}$. In this case too, no significant shift or change on the bands is observed with the type of amount of doping. Also, the distortion frequencies of doped and undoped YBO_3

products are 576 and 710 cm^{-1} and stretching frequencies are 829, 906, 1005 and 1077 cm^{-1} belong to tetrahedral $B_3O_9^{9-}$ borate units.

SEM images of all types and different percentage doping amount $LnBO_3$ powders show a fine particle size and regular morphology. In addition, we observed that REE doped $LnBO_3$ samples sizes are roughly the same as undoped $LnBO_3$ samples size. EDX results of REE doped $LnBO_3$ powders prove that doping has been done successfully.

Far-IR studies provide the low frequency vibration modes of REE doped and undoped $LnBO_3$ samples. RE oxides La_2O_3, Gd_2O_3, Y_2O_3, Sm_2O_3, Dy_2O_3, Tb_4O_7 and boric acid Far-IR spectra were collected since there is no data available for this region of the spectrum. In the light of these results, we can suggest that the vibration modes of low frequencies belong to various type of RE-O modes. We can suggest that La-O vibrational modes in the La-O-B network are at 290, 188 and 138 cm^{-1} and Gd-O vibrational modes the G-O-B network are at 478, 398, 390-360, 242, 150 and 141 cm^{-1} and Y-O vibrational modes in the Y-O-B network at 404, 287, 202 and 180 cm^{-1}.

Some peaks were observed when doping amounts increased, so we may suggest that when doping agent might have interstitial in $LnBO_3$ structure. Thus, interstitial doping ions cause expansion in structure and we observed these newly formed peaks. Finally, we may conclude that doping materials might prefer to have substitution instead of interstitial in $LnBO_3$ structure. This result proves that substitution doping ions enhancing luminescence intensity.

Variants in $LnBO_3$: REE emissions have been observed for the samples synthesized. When the best emissions are taken into consideration, Dy gives $^4F_{9/2}\rightarrow{}^6H_{15/2}$, $^4F_{9/2}\rightarrow{}^6H_{13/2}$ and $^4F_{9/2}\rightarrow{}^6H_{11/2}$, Sm gives $^4G_{5/2}\rightarrow{}^6H_{5/2}$, $^4G_{5/2}\rightarrow{}^6H_{7/2}$ and $^4G_{5/2}\rightarrow{}^6H_{9/2}$, Tb gives $^5D_4\rightarrow{}^7F_6$, $^5D_4\rightarrow{}^7F_4$, $^5D_4\rightarrow{}^7F_3$, $^5D_4\rightarrow{}^7F_2$ transitions. When luminescence intensities of the three hosts are compared, we observed that RE doped $LaBO_3$ samples give the best luminescence intensities. In addition, we concluded that $LaBO_3$ borate units are planar BO_3^{3-} but YBO_3, $GdBO_3$ samples borate units are tetrahedral $B_3O_9^{9-}$. So, we may suggest that hosts that possess planar BO_3^{3-} structure give higher intensity than hosts that possess tetrahedral $B_3O_9^{9-}$. In addition, we compared emissions intensity among the three different doping agent (Dy, Sm, Tb) in $LaBO_3$ structure, we

notice that Dy doped $LaBO_3$ product emission intensity higher than Sm and Tb doped $LaBO_3$ samples. Finally, emission intensities of different amounts of doping are compared, we observed that 5.30 % mole of Dy doping sample's luminescence intensity is higher than other samples' luminescence intensity. Therefore, critical doping amount is 5.30 % mole of Dy. So, when doping amount exceeds 5.30 %, concentration quenching occurs.

The CIE results show that Dy doped samples give yellow-pale yellow-whitish yellow color, Sm doped samples give darker orange-lighter orange color and Tb doped samples give green color. Different doping concentrations do not change the color observed in all hosts and doping agents because doping ions' radii and host ions' radii are very close. Therefore, different doping concentration samples give almost the same color. This is due to the fact that when host ion and doping ion radii are very close in dimension to each other, the ratio of Yellow/Blue does not change with changing concentrations of doping agent.

REFERENCES

[1] Eti Maden, "Bor sektör raporu," 2013.

[2] B. P. a Lyday, "By Phyllis A. Lyday," no. 37, pp. 1–10, 2008.

[3] D. Trimnell, B. S. Shasha, R. E. Wing, and F. H. Otey, "Pesticide encapsulation using a starch–borate complex as wall material," *J. Appl. Polym. Sci.*, vol. 27, no. 10, pp. 3919–3928, 1982.

[4] C. Helvaci and R. B. Kistler, *Industrial Minerals and Rocks*, 6th ed. Littleton, Colarado: Society for Mining and Metallurgy and Exploration Inc., 1994.

[5] I. Ore, P. Rock, Q. Crystal, R. Earths, S. Ash, and S. Sulfate, "Zirconium Mineral Commodity Summaries 2009," 2009.

[6] U. S. G. Survey, "Mineral commodity summaries 2013," *U.S. Geol. Surv.*, p. 198p, 2013.

[7] Asian Glass, "Marching Ahead Borates Look to High Priced Future." pp. 56–57, 2012.

[8] A. Kitai, "Phosphor Quantum Dots," in *Luminescent Materials and Applications*, Canada: John Wiley&Sons, 2008, p. 19.

[9] B. Valeur and M. N. Berberan-Santos, *Molecular Fluorescence: Principles and Applications*, 2nd ed. Wiley-VCH Verlag GmbH & Co. KGaA, 2013.

[10] H. Morkoç, S. Strite, G. B. Gao, M. E. Lin, B. Sverdlov, and M. Burns, "Large-band-gap SiC, III-V nitride, and II-VI ZnSe-based semiconductor device technologies," *J. Appl. Phys.*, vol. 76, no. 3, pp. 1363–1398, 1994.

[11] J. Faist, F. Capasso, D. L. Sivco, C. Sirtori, A. L. Hutchinson, and A. Y. Cho, "Quantum Cascade Laser," *Science (80-.).*, vol. 264, no. 5158, pp. 553–556, Apr. 1994.

[12] J. W. Stouwdam and F. C. J. M. Van Veggel, "Near-infrared Emission of Redispersible Er^{3+}, Nd^{3+}, and Ho^{3+} Doped LaF_3 Nanoparticles," *Nano Lett.*, vol. 2, no. 7, pp. 733–737, 2002.

[13] R. E. Bailey and S. Nie, "Alloyed semiconductor quantum dots: Tuning the optical properties without changing the particle size," *J. Am. Chem. Soc.*, vol. 125, no. 23, pp. 7100–7106, 2003.

[14] M. A. Hines and G. D. Scholes, "Colloidal PbS Nanocrystals with Size-Tunable

Near-Infrared Emission: Observation of Post-Synthesis Self-Narrowing of the Particle Size Distribution," *Adv. Mater.*, vol. 15, no. 21, pp. 1844–1849, Nov. 2003.

[15] P. W. Barone, S. Baik, D. a Heller, and M. S. Strano, "Near-infrared optical sensors based on single-walled carbon nanotubes," *Nat. Mater.*, vol. 4, no. 1, pp. 86–92, 2004.

[16] J. L. Sommerdijk, A. Bril, and A. W. de Jager, "Luminescence of Pr^{3+}-Activated fluorides," *J. Lumin.*, vol. 9, no. 4, pp. 288–296, 1974.

[17] G. Blasse and N. L. Materials, "New Luminescent Materials," *Chem. Mater.*, vol. 1, no. 10, p. 294, 1989.

[18] X. He, J. Zhou, N. Lian, J. Sun, and M. Guan, "Sm^{3+}-activated gadolinium molybdate: an intense red-emitting phosphor for solid-state lighting based on InGaN LEDs," *J. Lumin.*, vol. 130, no. 5, pp. 743–747, 2010.

[19] B. Valeur and N. Berberan-Santos, "A Brief History of Fuorescence and Phosphorescence before the Emergence of Quantum Theory," *J. Chem. Educ.*, vol. 88, pp. 731–738, 2011.

[20] A. Jabłoński, "Efficiency of Anti-Stokes Fluorescence in Dyes," *Nature*, vol. 131, no. 3319, pp. 839–840, 1933.

[21] M. Sauer, J. Hofkens, and J. Enderlein, *Handbook of Fluorescence Spectroscopy and Imaging*. Weinheim, Germany: Wiley-VCH Verlag GmbH & Co. KGaA, 2011.

[22] K. N. Shinde, S. J. Dhoble, H. C. Swart, and K. Park, *Phosphate Phosphors for Solid-State Lighting*, vol. 174. 2012.

[23] D. R. Vij, "Luminescence of Solids," *Nature*, vol. 170, no. 4320, pp. 259–259, 1952.

[24] A. S. Coolidge, H. M. James, and R. D. Present, "A Study of the Franck-Condon Principle," *J. Chem. Phys.*, vol. 4, no. 3, p. 193, 1936.

[25] G. H. Dieke, H. M. Crosswhite, and B. Dunn, "Emission Spectra of the Doubly and Triply Ionized Rare Earths," *J. Opt. Soc. Am.*, vol. 51, no. 8, p. 820, 1961.

[26] W. T. Carnall, G. L. Goodman, K. Rajnak, and R. S. Rana, "A systematic analysis of the spectra of the lanthanides doped into single crystal LaF_3," *J.*

Chem. Phys., vol. 90, no. 7, pp. 3443–3457, 1989.

[27] S. Özkar and N. K. Tunalı, *Anorganik Kimya*, 7th ed. Ankara: ÖzBaran Ofset, 2009.

[28] Y. Tian, W. H. Cao, X. X. Luo, and Y. Fu, "Preparation and luminescence property of Gd_2O_2S:Tb X-ray nano-phosphors using the complex precipitation method," *J. Alloys Compd.*, vol. 433, no. 1–2, pp. 313–317, 2007.

[29] P. A. M. Berdowski, M. J. J. Lammers, and G. Blasse, "$^5D_3$ – $^5D_4$ cross relaxation in Tb^{3+} pairs in CsCdBr3 crystals," *J. Chem. Phys.*, vol. 83, no. 1985, pp. 476–479, 1985.

[30] A. A. da Silva, M. A. Cebim, and M. R. Davolos, "Excitation mechanisms and effects of dopant concentration in $Gd_2O_2S:Tb^{3+}$ phosphor," *J. Lumin.*, vol. 128, no. 7, pp. 1165–1168, 2008.

[31] R. Velchuri, B. V. Kumar, V. R. Devi, G. Prasad, D. J. Prakash, and M. Vithal, "Preparation and characterization of rare earth orthoborates, $LnBO_3$ (Ln = Tb, La, Pr, Nd, Sm, Eu, Gd, Dy, Y) and $LaBO_3$:Gd, Tb, Eu by metathesis reaction: ESR of $LaBO_3$:Gd and luminescence of $LaBO_3$:Tb, Eu," *Mater. Res. Bull.*, vol. 46, no. 8, pp. 1219–1226, 2011.

[32] H. Zhang, "Luminescence characteristics of europium and terbium complexes with 1,10-phenanthroline in-situ synthesized in a silica matrix by a two-step sol–gel process," *Mater. Lett.*, vol. 38, no. 4, pp. 260–264, 1999.

[33] I. Arul Rayappan, K. Marimuthu, S. Surendra Babu, and M. Sivaraman, "Concentration dependent structural, optical and thermal investigations of Dy^{3+} doped sodium fluoroborate glasses," *J. Lumin.*, vol. 130, no. 12, pp. 2407–2412, 2010.

[34] R. Praveena, R. Vijaya, and C. K. Jayasankar, "Photoluminescence and energy transfer studies of Dy^{3+}-doped fluorophosphate glasses," *Spectrochim. Acta - Part A Mol. Biomol. Spectrosc.*, vol. 70, no. 3, pp. 577–586, 2008.

[35] S. Zulfiqar Ali Ahamed, C. Madhukar Reddy, and B. Deva Prasad Raju, "Structural, thermal and optical investigations of Dy^{3+} ions doped lead containing lithium fluoroborate glasses for simulation of white light," *Opt. Mater. (Amst).*, vol. 35, no. 7, pp. 1385–1394, 2013.

[36] C. R. Kesavulu and C. K. Jayasankar, “White light emission in Dy^{3+}-doped lead fluorophosphate glasses,” *Mater. Chem. Phys.*, vol. 130, no. 3, pp. 1078–1085, 2011.

[37] J. Pisarska, “Luminescence behavior of Dy^{3+} ions in lead borate glasses,” *Opt. Mater. (Amst).*, vol. 31, no. 12, pp. 1784–1786, Oct. 2009.

[38] Y. C. Li, Y. H. Chang, Y. F. Lin, Y. S. Chang, and Y. J. Lin, “Synthesis and luminescent properties of Ln^{3+} (Eu^{3+}, Sm^{3+}, Dy^{3+})-doped lanthanum aluminum germanate $LaAlGe_2O_7$ phosphors,” *J. Alloys Compd.*, vol. 439, no. 1–2, pp. 367–375, 2007.

[39] Y. S. Tang, S. F. Hu, C. C. Lin, N. C. Bagkar, and R. S. Liu, “Thermally stable luminescence of KSrPO4:Eu^{2+} phosphor for white light UV light-emitting diodes,” *Appl. Phys. Lett.*, vol. 90, no. 15, pp. 4–6, 2007.

[40] Y. Xu, W. Peng, S. Wang, X. Xiang, and P. Lu, “Synthesis of $SrAl_2O_4$ and $SrAl_{12}O_{19}$ via ethylenediaminetetraacetic acid precursor,” *Mater. Chem. Phys.*, vol. 98, no. 1, pp. 51–54, 2006.

[41] X. Qin, Y. Li, Y. Li, Y. Wu, R. Chen, K. Sharafudeen, Z. Ma, S. Liu, D. Wu, and J. Qiu, “Inducing NIR long persistent phosphorescence in Cr-doped perovskite titanate via redox,” *J. Alloys Compd.*, 2016.

[42] E. Wilhelm, *Silicate Science*, 7th ed. London: Academic press, 1976.

[43] R. S. R. and J. B. M. Ernest M. Levin, “Polymorphism of ABO_3 type rare earth borates,” *Am. Mineral.*, vol. 46, no. 1954, pp. 1030–1055, 1961.

[44] G. Chadeyron, R. Mahiou, M. El-Ghozzi, A. Arbus, D. Zambon, and J. C. Cousseins, “Luminescence of the orthoborate YBO_3: Eu^{3+}. Relationship with crystal structure,” *J. Lumin.*, vol. 72, pp. 564–566, 1997.

[45] G. Chadeyron, M. El-Ghozzi, R. Mahiou, a Arbus, and J. C. Cousseins, “Revised Structure of the Orthoborate YBO_3,” *J. Solid State Chem.*, vol. 128, no. 128, pp. 261–266, 1997.

[46] H. G. Giesber, J. Ballato, W. T. Pennington, and J. W. Kolis, “Synthesis and characterization of optically nonlinear and light emitting lanthanide borates,” in *Information Sciences*, 2003, vol. 149, no. 1–3, pp. 61–68.

[47] M. Ren, J. H. Lin, Y. Dong, L. Q. Yang, M. Z. Su, and L. P. You, “Structure

and Phase Transition of $GdBO_3$," *Chem. Mater.*, vol. 11, no. 6, pp. 1576–1580, 1999.

[48] J. Hölsä, "Luminescence of Eu^{3+} ion as a structural probe in high temperature phase transformations in lutetium orthoborates," *Inorganica Chim. Acta*, vol. 13, no. 1–2, pp. 257–259, 1987.

[49] J. H. Lin, D. Sheptyakov, Y. X. Wang, and P. Allenspach, "Structures and phase transition of vaterite-type rare earth orthoborates: A neutron diffraction study," *Chem. Mater.*, vol. 16, no. 22, pp. 2418–2424, 2004.

[50] A. Pitscheider, R. Kaindl, O. Oeckler, and H. Huppertz, "The crystal structure of ??-$ErBO_3$: New single-crystal data for an old problem," *J. Solid State Chem.*, vol. 184, no. 1, pp. 149–153, 2011.

[51] S. Seyyidoğlu, "Synthesis And Characterization Of Novel Rare Earth Phosphates And Rietveld Structural Analysis Of Rare Earth Orthoborates," METU, 2009.

[52] M. Helge, T. Nikelski, M. B. O. M. Bo, M. B. O. Der Lanthanide, W. Ca, and O. Si, "Einkristalle des Neodym (III) -meta-Borats $Nd(BO_2)_3$ und -ortho-Borats Nd [BO 3]," no. Iii, pp. 375–380, 2003.

[53] Dr. H. Putz & Dr. K. Brandenburg, "Diamond - Crystal and Molecular Structure Visualization Crystal Impact." Bonn, Germany.

[54] S. Lemanceau, R. Mahiou, J. C. Cousseins, P. Con, and R. N. Vannier, "Synthesis and Characterization of H-$LnBO_3$ Orthoborates (Ln ، La , Nd , Sm , and Eu)," *J. Solid State Chem.*, vol. 148, pp. 229–235, 1999.

[55] E. F. Schubert, "CIE 1931 x, y Chromaticity Diagram," *Rensselaer Polytechnic Institute*. [Online]. Available: https://www.ecse.rpi.edu/~schubert/Light-Emitting-Diodes-dot-org/chap17/F17-04 Chromaticity diagram.jpg. [Accessed: 15-Apr-2016].

[56] N. Kohei and K. Sueko, "Color Vision," in *Phosphor Handbook*, 2nd ed., M. William, S. Shionoya, and H. Yamamoto, Eds. 2006, p. 967.

[57] J. Wiwattanapongpan, O. Mekasuwandumrong, C. Chaisuk, and P. Praserthdam, "Effect of dopants on the properties of metal-doped zirconia prepared by the glycothermal method," *Ceram. Int.*, vol. 33, no. 8, pp. 1469–

1473, 2007.

[58] S. T. Aruna and A. S. Mukasyan, “Combustion synthesis and nanomaterials,” *Curr. Opin. Solid State Mater. Sci.*, vol. 12, no. 3–4, pp. 44–50, 2008.

[59] C. Badan, “Microwave Assisted Synthesis of Rare Earth Ions Doped Lanthanum Orthoborate, Their Characterizations and Investigations of Luminescence Properties,” METU, 2012.

[60] M. Gaft, G. Panczer, R. Reisfeld, and I. Shinno, “Laser-induced luminescence of rare-earth elements in natural zircon,” *J. Alloys Compd.*, vol. 300, pp. 267–274, 2000.

[61] F. Liu, S. Zuo, W. Kong, and C. Qi, “High-temperature synthesis of strong acidic ionic liquids functionalized, ordered and stable mesoporous polymers with excellent catalytic activities,” *Green Chem.*, vol. 14, no. 5, p. 1342, 2012.

[62] J. B. Holt, “Simultaneous synthesis and densification of TiC / Ni-AI composites,” vol. 26, pp. 2410–2416, 1991.

[63] A. C. Pierre, *Introduction to Sol-Gel Processing*, 1st ed., vol. 1. Boston, MA: Springer US, 1998.

[64] H. Bin, W. Yi-Fei, L. Qian, and H. Qing, “Microwave Assisted Sintering and Photoluminescence Properties of $Ba_3Si_6O_{12}N_2$:Eu^{2+} Green Phosphors,” *J. Inorg. Mater.*, vol. 30, no. 3, p. 330, 2015.

[65] R. Mahiou, C. Caperaa, D. Boyer, and J. Cousseins, “Synthesis dependent luminescence efficiency in Eu^{3+} doped polycrystalline YBO_3 `,” pp. 211–214, 1999.

[66] E. Lesley and E. Moore, *Solid State Chemistry*, 4th ed. CRC Press, 2012.

[67] K. Y. Jung, H. W. Lee, Y. C. Kang, S. B. Park, and Y. S. Yang, “Luminescent properties of (Ba, Sr) $MgAl_{10}O_{17}$: Mn, Eu green phosphor prepared by spray pyrolysis under VUV excitation,” *Chem. Mater.*, vol. 17, no. 10, pp. 2729–2734, 2005.

[68] Encyclopædia Britannica, “rare-earth element,” 2016. [Online]. Available: http://global.britannica.com/science/rare-earth-element. [Accessed: 11-May-2016].

[69] C. Badan, O. Esenturk, and A. Yilmaz, “Microwave-assisted synthesis of Eu^{3+}

doped lanthanum orthoborates, their characterizations and luminescent properties," *Solid State Sci.*, vol. 14, no. 11–12, pp. 1710–1716, 2012.

[70] C. E. Weir and E. R. Lippincott, "Infrared studies of aragonite, calcite, and vaterite type structures in the borates, carbonates, and nitrates," *J. Res. Natl. Bur. Stand. Sect. A Phys. Chem.*, vol. 65A, no. 3, p. 173, 1961.

[71] M. Shang, C. Li, and J. Lin, "How to produce white light in a single-phase host?," *Chem. Soc. Rev.*, vol. 43, no. 5, pp. 1372–86, 2014.